DESIGN OPTIMISATION OF THE FAST SWITCHED CHOPPER DIPOLE MAGNET FOR THE MEDAUSTRON PROJECT

by

Miroslav Atanasov

A thesis submitted in partial fulfilment of the requirements
for the degree of
MSc
Technical University of Sofia, Plovdiv Branch

2014

Declaration

I hereby declare that this text is the result of my own original work. Where external sources have been used they have been properly cited and acknowledged.

Geneva, 29 August 2014

Miroslav Atanasov

Table of contents

Abstract

The MedAustron hadron therapy centre currently under construction in Wiener Neustadt, Austria, is a synchrotron based accelerator facility for cancer treatment with protons and carbon ions. The concept for such a machine first originated at the European Organization for Nuclear Research (CERN) in 1999 as the Proton-Ion Medical Machine Study (PIMMS). The first centre based on this concept was the National Centre for Oncological Treatment (CNAO) built in Italy, which treated its first patient in November 2012. The MedAustron accelerator complex consists of three particle sources, a linear accelerator, a synchrotron, an extraction line, and four irradiation rooms (1 experimental area with horizontal fixed beam, 2 fixed beam line rooms (one horizontal, and one horizontal and vertical) and a rotating gantry treatment room). It will be capable of accelerating $^1H^+$ protons to energies of 60-250 MeV for clinical purposes, and up to 800 MeV for research purposes. It will also accelerate $^{12}C^{6+}$ carbon ions to energies of 120-400 MeV/u. An energy of 400 MeV/u for the carbon ions corresponds to a beam rigidity $B\rho$ of 6.35 Tm, which determines the maximum strength of the required magnetic elements.

The treatment rooms will be able to switch the beam on and off rapidly ($< 240\,\mu s$) during routine operation, or during emergencies. For the purpose, a beam chopper system will be installed in the extraction line, comprising four identical fast switched dipole magnets electrically connected in series. In the "ON" state, the magnets will deviate the beam around a dump block mounted inside the beam vacuum chamber. When the magnets are switched off the beam will be absorbed by the dump, thus making the chopper system a device in the safety chain to prevent a mismatched beam from being sent to a treatment room inadvertently.
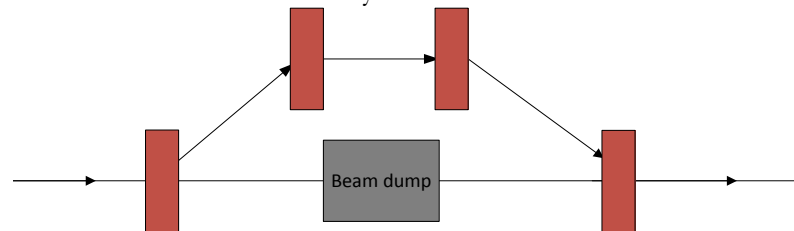
Figure 1. Schematic representation of the chopper operation

The initial design of the magnets has been based on experience from CNAO, and realised at CERN by the MedAustron Special Magnets work package. The production of the magnets has been subcontracted to the company Danfysik, based in Taastrup, Denmark.

The author was involved in the 3D Finite Element electromagnetic design optimisation and was responsible for the validation of the mechanical models and drawings, and the contract follow-up, ensuring that the specified magnet parameters were respected in the final design. Being the link between the FEM models and the mechanical design, the author optimized the magnet coil heads, and ferrite pole shape in the end-regions, validating their impact on the desired $\pm\,0.2\,\%$ field homogeneity in the magnet gap. He examined different insulation schemes and their impact on the field quality, as well as the impact of any possible manufacture and assembly defects and misalignments. The author also studied the influence on the effective magnetic length of the device of the brazing collars for the flanges on the ceramic vacuum chambers. The author was involved in the final magnetic measurements and factory acceptance tests, thus assuring that the magnets delivered to the project would perform according to the technical specification.

Резюме

Центърът за адронна терапия МедАустрон, който в настоящия етап е в процес на изграждане във Винер Нойщат, Австрия е реализиран на базата на синхротрон за ускоряване на протонни и йонни лъчи за концентрирано облъчване на ракови клетки. Идеята за създаването на такава машина се ражда в Европейската организация за ядрени изследвания (ЦЕРН) през 1999 под името Проект за протонно-йонно медицинско съоръжение (PIMMS). Първият терапевтичен център, базиран на тази концепция е Националният център за онкологична адронна терапия (CNAO), построен в Италия, с първо облъчване на пациент – Ноември 2012. Комплексът МедАустрон се състои от три йонни източника, линеен ускорител, синхротрон, линия за екстракция на ускорения лъч частици и четири зали за облъчване: една експериментална с фиксирано хоризонтално подаване на лъча, две терапевтични, съответно с хоризонтално и хоризонтално-вертикално подаване, и зала с въртящ портал (gantry). Машината ще бъде способна да ускорява ^{1}H$^+$ протони до енергийни нива между 60-250 MeV за клинични и до 800 MeV за изследователски цели. Съоръжението също така ще може да ускорява ^{12}C^{6+} въглеродни йони до енергийни нива между 120-400 MeV/u. Енергийното ниво 400 $MeV/$u за лъч от въглеродни йони отговаря на магнитна твърдост на лъча $B\rho$, равна на 6.35 Tm, която предопределя и максималната сила и мощност на магнитните елементи на машината.

По време на рутинна работа, а също така и в случаи на авария, терапевтичните зали ще имат възможност за бързо включване или изключване на лъча частици (< 240 μs). За целта в линията за екстракция е инсталиран т.нар. превключвател на лъча (beam chopper). Системата на превключвателя се състои от четири идентични бързопулсиращи електромагнита, включени последователно към общо захранващо устройство. Във включено състояние магнитите ще отклоняват лъча в хоризонталната равнина, направлявайки го по траектория, заобикаляща блок от абсорбиращ материал (beam dump), монтиран във вакуумната камера. При изключване лъчът ще попадне в абсорбера, където енергията му ще бъде погълната и разсеяна във вид на топлина. Функционално, превключвателят на лъча е защитно устройство, което е последна преграда между пациента и протонен/йонен лъч с погрешни и/или потенциално опасни параметри.
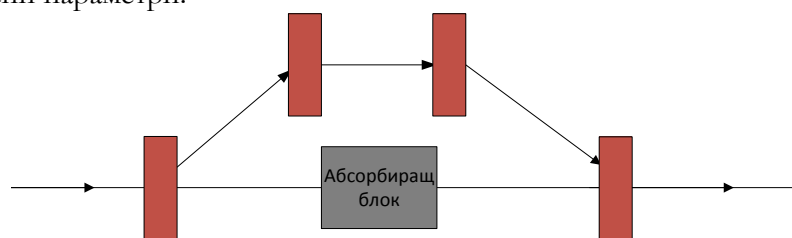
Фиг. 1. Принципна схема

Проектирането на магнитите е осъществено на базата на предишен опит от CNAO и е реализирано в ЦЕРН от работната група „Специални магнити" на МедАустрон. Производството е възложено на подизпълнител – компанията Danfysik, базирана в Тааструп, Дания.

Като част от работната група „Специални магнити", авторът участва в електромагнитното моделиране на устройствата с тримерния метод на крайните елементи, в утвърждаването на механичните модели и производствените чертежи и в контрола на изпълнението на договора от страна на подизпълнителя, гарантирайки запазването във финалния дизайн на зададените по спецификация електромагнитни параметри. В осъществяването на връзката между електромагнитните и механичните модели авторът оптимизира формата на челата на намотката и на крайните участъци на феритния

магнитопровод, установявайки тяхното влияние върху зададената по спецификация $\pm\,0.2\,\%$ хомогенност на полето във въздушната междина. Авторът изследва няколко възможни конфигурации на изолацията на намотката, както и въздействието на възможни производствени и конструкционни дефекти върху желаната хомогенност. В хода на симулациите авторът квантифицира влиянието върху ефективната магнитна дължина на твърдия припой, свързващ керамичната вакуумна камера и стоманените фланци. Авторът участва във финалните магнитни измервания и приемателни изпитвания, обезпечавайки доставката за проекта на устройства с параметри съответстващи на предварително зададените.

Acknowledgements

Preface

Traditional radiation therapy utilises high-energy photons produced by 6-20 MeV electron linacs. When these short-wavelength photons (X, or gamma rays) strike condensed matter they release electrons from the atoms they interact with. During these interactions, the photons are strongly scattered, with statistical laws governing the energy absorption processes. Therefore, a photon beam entering condensed matter spreads rapidly and has no defined range. Furthermore, the beam has a maximum within the first 2.5 cm of tissue before attenuating exponentially as it traverses deeper into the body. For these reasons, when treating a deep-seated tumour an unacceptably large dose is being delivered to the healthy tissue surrounding it [1] [2] [3].

Hadron Beams for Cancer Therapy

Hadron therapy is the collective term describing the techniques of treating tumours by means of irradiating them with a beam of non-elementary particles made of quarks. The main advantage can be seen on their particular depth-dose distribution curves (Figure 1). They are characterised by a slow initial increase with penetration depth, and a steep rise up to a maximum, known as the Bragg peak, followed by a sharp fall towards the end of their range. Protons and heavy ions are characterised by much higher masses as compared to electrons (the proton to electron mass ratio is 1836:1), therefore they experience significantly less lateral scattering. This property allows a proton or ion beam to penetrate the body with minimum diffusion. Carbon ions are particularly suited for the task, as they possess a much larger biological effectiveness than X-rays and even protons against deep-seated radio-resistant tumours. This can partly be explained by the fact that carbon ions resemble strongly the way the human body is built. The linear energy transfer, being the measure for the energy deposited by an ionizing particle travelling through matter is much higher for carbon ions, especially in the Bragg peak region, and it can produce multiple, hence irreparable distortions in the DNA structure of the traversed cells.

To reach depths of about 27 cm in order to irradiate deep-seated tumours the particle energy must be in the range of 200 MeV for protons, and 400 MeV/u (4800 MeV total energy) for $^{12}C^{6+}$ carbon ions. To achieve such energies the synchrotron is an appropriate choice, as it also allows for easy variation of the particle energy and thus the depth of penetration, while remaining sufficiently compact to be installed in a hospital environment.
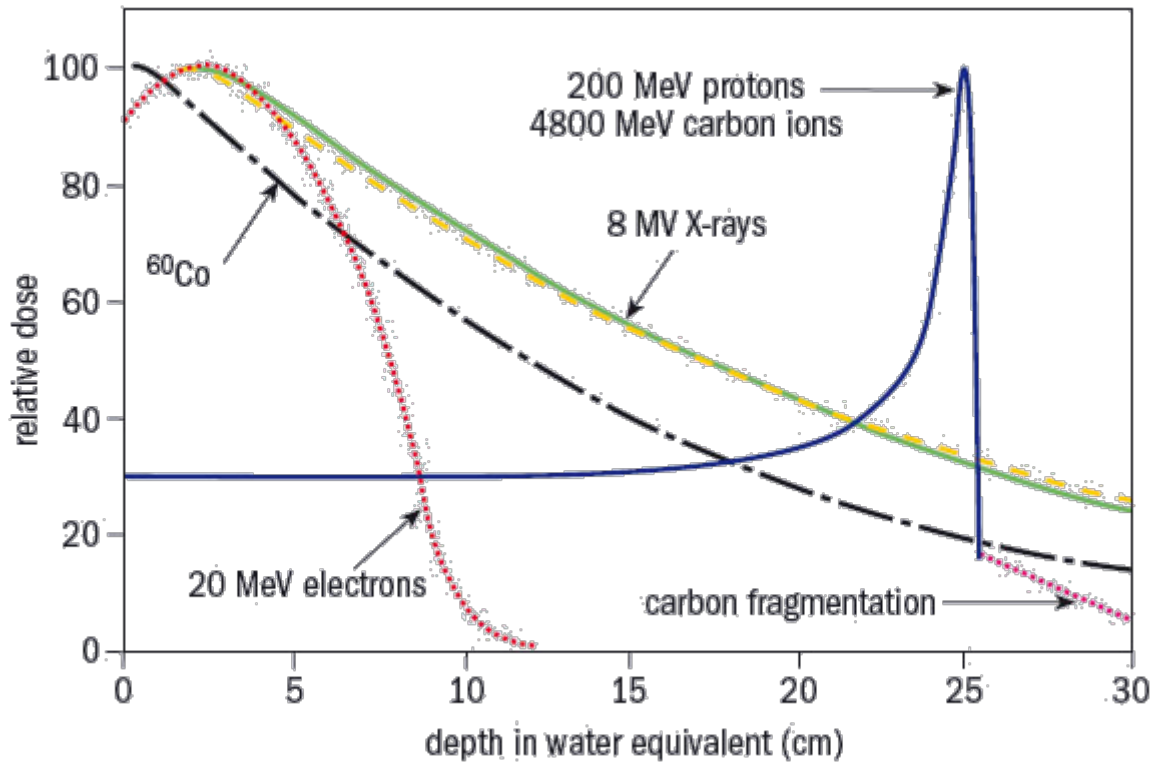
Figure 1. Depth-dose rate for different particle species

Another advantage of ion beams in comparison to photons is the possibility to spread out the Bragg peak to match the dimensions of the targeted structure. The dimensions and the depth of the spread out can be adjusted for a given particle type by varying the beam energy.
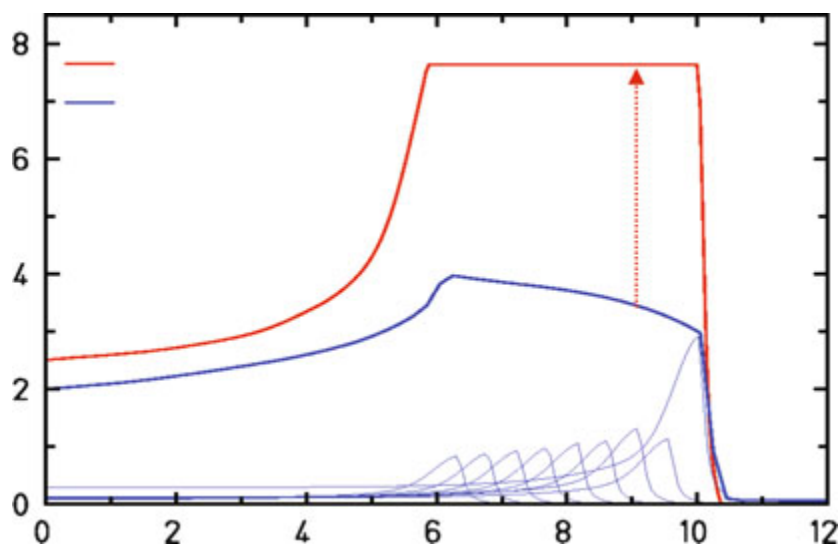
Figure 2. Spread-out Bragg peak. Courtesy of GSI, Darmstadt

The spread out Bragg peak (Figure 2) is composed of several overlaid pristine Bragg peaks, which together cover a larger volume with the maximum dose, a technique called high-precision

active scanning. To achieve this, a fast variation of the beam energy must be available from the accelerator.

The MedAustron project

Feasibility studies for the design and development of a cancer therapy synchrotron have begun in the late 90's as collaboration between MedAustron (Austria) and the TERA Foundation (Italy) and hosted by CERN's PS division. The resulting PIMMS (Proton-Ion Medical Machine Study) [4] was the base on which the National Hadron Therapy Centre for Cancer Treatment (CNAO) in Pavia, Italy was built and had its first patient treated with carbon ions in November 2012 [5]. The company EBG MedAustron GmBH was founded in 2007 with financial contributions by the Republic of Austria, the province of Lower Austria and the City of Wiener Neustadt. The main objective was to build and operate a proton and ion beam cancer treatment and research facility based on the PIMMS conceptual design study using the experience from the construction and commissioning of the CNAO centre.

The MedAustron centre which is currently being built in the city of Wiener Neustadt will be one of the most advanced centres for cancer therapy in Europe, and one of only four facilities worldwide that will be capable of both proton and ion beam tumour treatment. Upon its completion expected in late 2015, the centre will be capable of treating up to 1400 patients per annum.

The design and development of the synchrotron is based on the CNAO machine. It is being done in close collaboration with the European Organisation for Nuclear Research – CERN – the world's leading particle physics laboratory, with its first Proton Synchrotron (CPS, commissioned in 1959), and currently home to the biggest and most powerful particle accelerator ever constructed, the Large Hadron Collider (LHC). The engineering of the accelerator components takes place at CERN allowing the MedAustron project to benefit from CERN's expertise and know-how in building and operating particle accelerators.

Chapter 1

Introduction

Given the current state of technology and the engineering materials and techniques available, the particle beam energies required for both therapeutical and research purposes for the MedAustron centre can only be achieved using a traditional synchrotron. This chapter will briefly present the main operational principles of a synchrotron with the basic laws governing its work, followed by an overview of the MedAustron machine and the chopper dipole system.

1.1 Particle beam dynamics

The essence of particle accelerator physics is the interaction of charged particles with electromagnetic fields. Beam dynamics uses the theories of electromagnetism, classical and relativistic mechanics in order to provide the tools for describing these interactions in a predictable and repeatable manner [6] [7].

1.1.1 Basic units and constants in special relativity

The basic unit of energy used in particle accelerator physics is the electron volt (eV). 1 eV is the energy acquired by an electron traversing an accelerating potential of 1 V:

$$E = eU \tag{1.1}$$

Here e is the unit charge of the electron $e=1.602 \times 10^{-19}$ C, and U is the applied voltage. It then follows that $1eV = 1.602 \times 10^{-19}$ J.

As particles are accelerated from rest, at first an increase of speed is observed, but as the energy becomes higher the rate of increase of speed decreases as speed approaches the speed of light. Therefore, in accordance with Einstein's principle, the increase of energy corresponds to an increase of mass with velocity asymptotically approaching that of light.

In special relativity, the rest energy of a particle is defined as:

$$E_0 = m_0 c^2 \tag{1.2}$$

Here c is the speed of light in vacuum, equal to $3 \times 10^8 m/s$, and m_0 is the rest mass.

The mass of a proton is a fundamental constant equal to $1.67 \times 10^{-27} kg$. To find the energy equivalent of mass we must substitute in the general form of (1.2). It then follows that $E = 1.505 \times 10^{-10} J$, which expressed in units of eV/c^2 gives $938 \, MeV/c^2$ for the proton rest energy.

The ratio between the total energy and the rest energy of a particle, also known as the relativistic gamma factor is:

$$\gamma = \frac{E}{E_0} \tag{1.3}$$

The ratio between the particle velocity and the speed of light is:

$$\beta = \frac{v}{c} \tag{1.4}$$

The total energy is the sum of the kinetic energy T, and the particle rest energy E_0:

$$E = T + E_0 \tag{1.5}$$

Therefore:

$$\gamma = \frac{1}{\sqrt{1-\beta^2}} \tag{1.6}$$

$$\beta = \frac{\mathbf{p}c}{E} \tag{1.7}$$

Here the particle momentum is $\mathbf{p} = m\mathbf{v}$.

The momentum can now be expressed in terms of the energy. Using equations (1.5) and (1.7) we can rewrite:

$$E^2 = (pc)^2 + E_0^2$$
$$pc = \sqrt{(E_0+T)^2 - E_0^2} \tag{1.8}$$
$$pc = \sqrt{2E_0 T + T^2}$$

It can be seen that for highly relativistic particles the total energy is much higher than the rest energy, therefore γ is large and β is close to unity, which means that for relativistic particles the total energy and the momentum are practically equal.

Table 1.1 gives the charge, mass and rest energy of the proton and the electron.

Table 1.1. Charge and mass of the proton and the electron

	Electron	Proton
Charge e	$-1.602 \times 10^{-19} C$	$1.602 \times 10^{-19} C$
Mass m	$9.110 \times 10^{-31} kg$	$1.673 \times 10^{-27} kg$
Rest energy E_0	$0.511 \ MeV$	$938 \ MeV$

Knowing these values, the rest energy of light ions[1] can be approximated according to the following expression:

$$E_0 = AE_a - ZE_e \qquad (1.9)$$

In this formula, A is the atomic mass of the element, and Z is the ionization state (the number of electrons that have been removed from the shell). The atomic mass unit, which is equal to 1 gram, divided by the Avogadro constant yields $E_a = 931.494 \ MeV/c^2$. The electron rest energy is given in Table 1.1 [8].

1.1.2   The Lorentz force

Beam dynamics or beam optics explains the behaviour of charged particles under the influence of electric and magnetic fields. The force that is employed in guiding the particles along the predefined path, and in accelerating and focusing them is known as the Lorentz force:

$$\mathbf{F} = e\mathbf{E} + e[\mathbf{v} \times \mathbf{B}] \qquad (1.10)$$

Here $\mathbf{E}$ and $\mathbf{B}$ are the electric and magnetic field vectors, $\mathbf{v}$ is the particle velocity vector, and e – the elementary charge. In the case of ions we need to include the net charge eZ.

The Lorentz force is invariant under coordinate transformations, and is the sole instrument for particle guidance and acceleration.

An electric field component in the direction of particle motion increases the particle energy, whereas due to the vector cross product the magnetic field does not contribute to the acceleration. The magnetic field changes the direction of the particle momentum vector, resulting in a deflection of the particle trajectory. The force resulting from the magnetic component is normal to the direction of propagation of the particle and normal to the direction of the magnetic field.

It can be seen that if $\mathbf{E} = v\mathbf{B}$, the same force can be obtained from either electric or magnetic field if the magnetic field is orthogonal to the particle velocity. For relativistic particles to produce the same force as from a magnetic field of 1 T, an electric field of around $3 \times 10^8 \ V/m$ needs to be applied, and whereas such magnetic fields are easily achieved, it is rather difficult to establish and maintain electric fields of this magnitude.

For these reasons, electric fields are mostly used for changing the particle energy (acceleration) and are directed longitudinally with respect to the particle trajectory, whereas magnetic fields are mostly used for particle guidance and focusing along the desired beam paths.

---

[1] This refers to ions with a low charge state where the binding energy of the electrons that have been removed can be neglected.

Thus the synchrotron relies on confining the particles in a circular trajectory of a constant radius by using a dipole magnetic field which is synchronised with the accelerating electric field in such a way that for every increase in energy, there is a corresponding increase of magnetic flux density so that the circular trajectory remains unchanged.

1.1.3   Guidance of charged particle beams

A charged particle traversing a magnetic field directed perpendicular to the page as shown on Figure 1.1, will maintain the circular trajectory with radius ϱ due to the equilibrium between the centrifugal force and the Lorentz force.
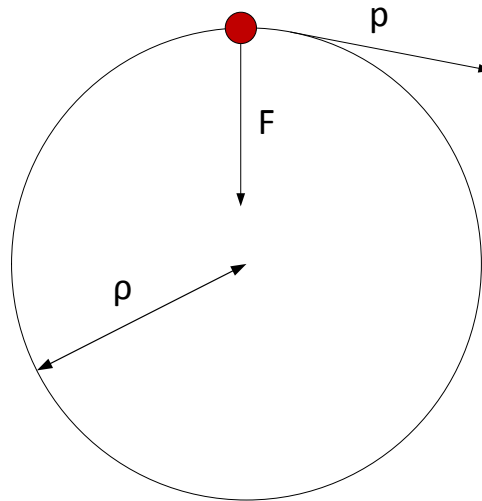

Figure 1.1. Charged particle on a circular trajectory

The balance of forces will give:

$$\mathbf{F}=e\mathbf{v}\mathbf{B}=\frac{m\mathbf{v}^2}{\varrho}$$
$$B\varrho=\frac{mv}{e}=\frac{p}{e}$$

(1.11)

The left hand of this equation has dimensions of [Tm], and is known as the magnetic rigidity of the particle beam. Using equation (1.7) we can express in more practical units:

$$B\varrho[Tm]=3.3356p[GeV/c]$$

(1.12)

The magnetic rigidity is a measure of the reluctance of a particle beam to deflections by a transverse magnetic field. Its highest value is derived from the maximum design energy of the synchrotron and will determine the maximum strength of the required magnetic elements.

1.1.4   Particle in a dipole field

The charged particles are guided along the circular beam path by a series of dipole magnets placed symmetrically along the orbit. A particle entering a dipole field will be deflected at a certain angle from its straight path due to the Lorentz force. The angle will depend on the particle energy,

the magnetic field strength, and the length of the magnet. Figure 1.2 shows a particle entering a magnetic field with magnitude B, and length l. Here for a positively charged particle, following the right hand rule, the field lines are coming out of the page.
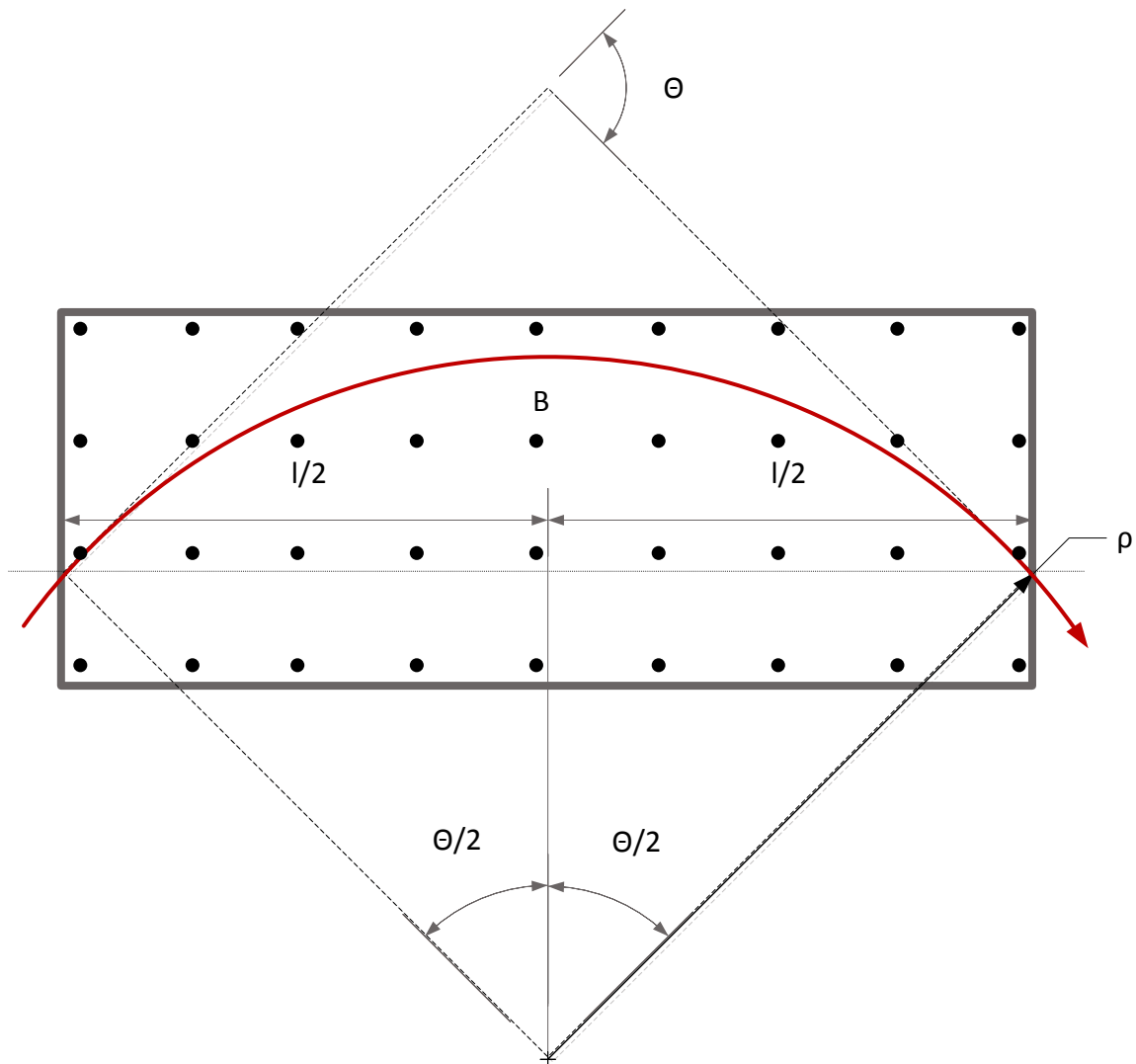

Figure 1.2. Particle trajectory in a bending magnet of length l

From the geometry it can be seen that the bending angle Θ can be expressed in terms of the magnet length and the radius of curvature:

$$\sin\frac{\theta}{2} = \frac{l}{2\varrho} = \frac{1}{2}\frac{lB}{B\varrho} \tag{1.13}$$

For a small deflection angle $\theta \ll \frac{\pi}{2}$, it follows that $\sin\frac{\theta}{2} \approx \theta$. Thus:

$$\theta = \frac{lB}{B\varrho} \tag{1.14}$$

The value of Θ is normally expressed in units of [*mrad*], where for small angles *1mrad≈1mm/1m*. *Bl* [*Tm*] is the integrated field in the centre of the magnet gap. It is a sum integral of the values of *B* over a straight line from $\pm\infty$ to the magnet centre. It is also referred to as *Bdl*, or *Bdz* (denoting the axis of integration), and its value divided by the magnetic induction B_0 in the magnet centre yields the so-called effective magnetic length.

1.1.5   Basic design characteristics of a dipole magnet

Low and medium energy synchrotrons generally use normal conducting iron-dominated electromagnets for particle guidance and focusing. These rely on soft ferromagnetic cores for amplification and channelling of the magnetic flux created by the copper or aluminium coil. The shape and quality of the fields in these magnets are predominantly determined by the geometry of the poles. The coil design is however equally important, especially with respect to the end fields and as the operating point reaches the iron saturation level.

For preliminary calculations it can be assumed that the iron yoke is non-saturated, and has a very large or infinite permeability. A schematic cross section of a dipole magnet is shown on Figure 1.3.
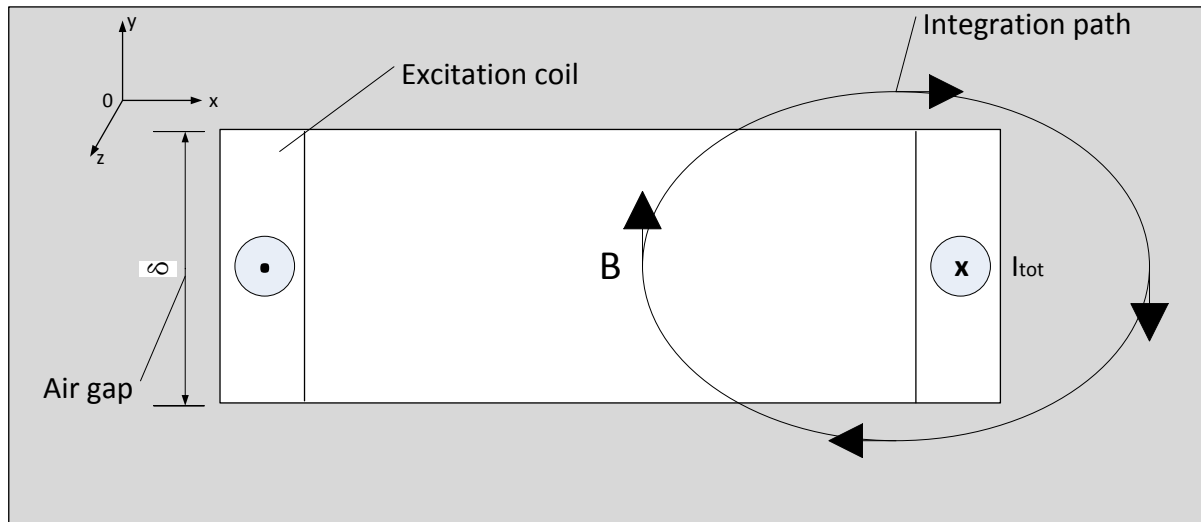

Figure 1.3. Cross section of a dipole magnet

The magnetic field is generated by the electrical current in the coils and the ferromagnetic yoke provides the return path for the flux. The relation between magnetic field and excitation current for static and quasi static problems can be expressed using Ampère's law:

$$\nabla\times\mathbf{H}=\mathbf{J} \tag{1.15}$$

The constitutive equation linking the magnetic field intensity to the flux density is:

$$\mathbf{B}=\mu\mathbf{H} \tag{1.16}$$

The magnetic permeability can be expressed as a function of the permeability of free space:

$$\mu=\mu_0\mu_r \tag{1.17}$$

Using Stoke's theorem, (1.15) can be integrated over the closed path shown in Figure 1.3:

$$\delta B + \int \frac{B}{\mu_r} dl = \mu_0 I_{tot} \tag{1.18}$$

Assuming very large permeability for the ferromagnetic yoke the integral term in the above equation becomes negligibly small. Thus the excitation current required to drive a magnetic flux with density B over an air gap of length δ can be expressed as:

$$I_{tot} = \frac{1}{\mu_0} B\delta \tag{1.19}$$

The total excitation current is given in Ampere-turns.

1.2   The MedAustron synchrotron

The MedAustron accelerator complex consists of three sources – two for ions and one for protons, a common linear accelerator, a synchrotron, an extraction line, and four irradiation rooms. It will be capable of accelerating $^1H^+$ protons to energies of 60-250 MeV for clinical purposes, and up to 800 MeV for research purposes. It will also accelerate $^{12}C^{6+}$ carbon ions to energies of 120-400 MeV/u. The lowest extraction energies are adjusted for tissue penetration of approximately 3.5 cm, whereas the maximum energy corresponds to a penetration depth of about 27 cm, which is considered sufficient for radiation therapy [4] [9] [10].

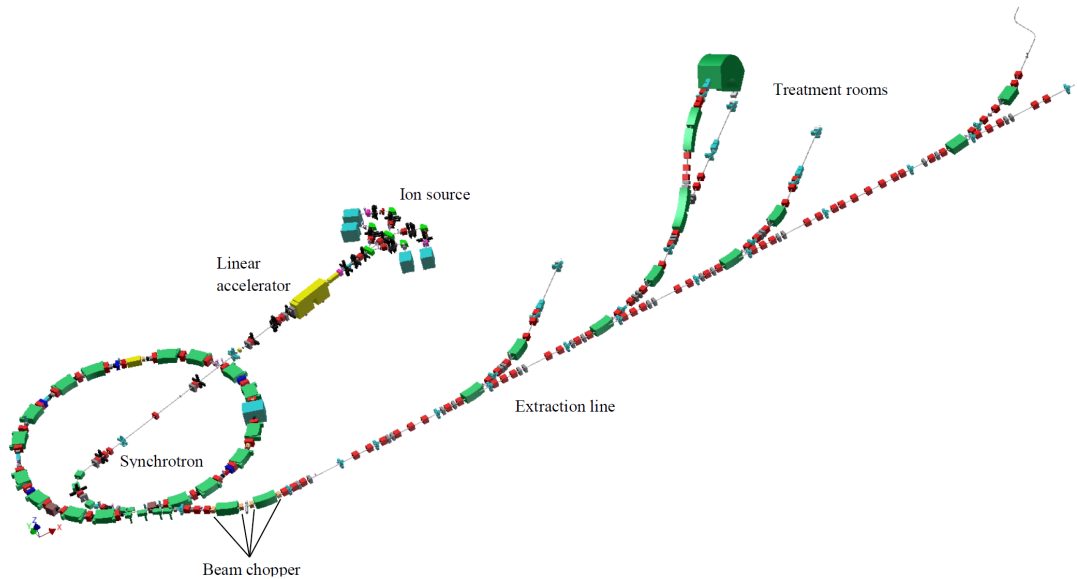A schematic of the accelerator complex is shown on Figure 1.4.

Figure 1.4. The MedAustron accelerator complex

An energy of 400 MeV/u for the carbon ions corresponds to a magnetic rigidity $B\varrho$ of 6.35 Tm, which determines the maximum strength of the required magnetic elements.

1.3   The chopper dipole

The beam chopper will allow the treatment rooms to switch the beam on and off during routine operation and in case of emergency. The concept of the system is laid down in [4]. It consists of four identical magnets connected in series that create a closed orbit bump deviating the beam around an internal dump block. Figure 1.5 shows a schematic representation of the chopper system. The system is capable of rapidly (less than 240 μs) switching the beam on and off without perturbing its position at the patient.
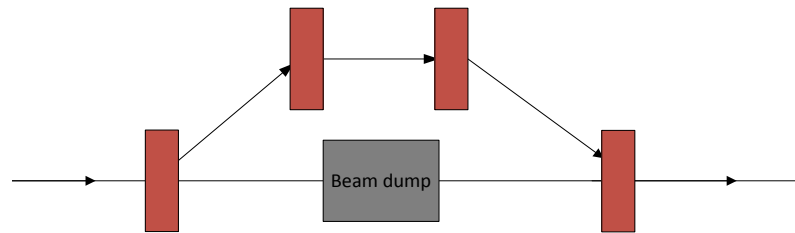

Figure 1.5. Beam chopper principle

The beam chopper is a fail-safe device since it can only allow beam downstream in its power on state. The chopper is the last barrier between the patient and a beam with incorrect and potentially dangerous parameters coming from the synchrotron.

The layout of the beam chopper system is shown on Figure 1.6. It is taken from the preliminary design study for PIMMS mainly as a guideline. The final dimensions of the chopper dipole yoke and vacuum chambers somewhat differ in the CNAO and MedAustron designs.
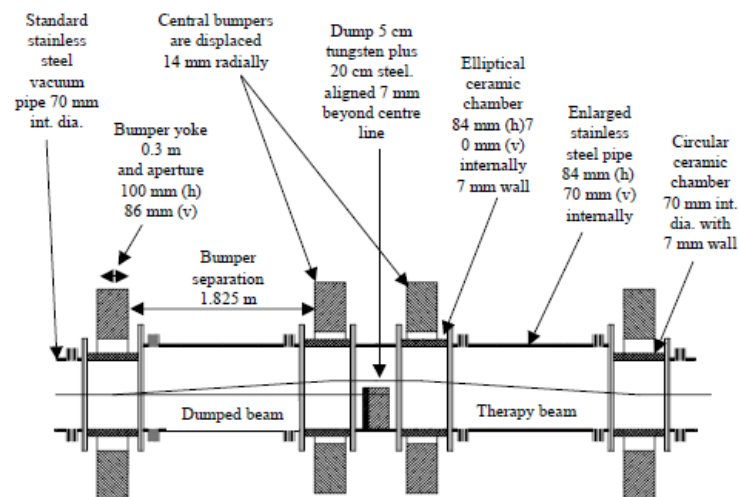

Figure 1.6. Layout of the beam chopper [4]

1.3.1   Initial magnet calculations

The preliminary calculations were done assuming the magnet separation as defined in PIMMS. The magnet design is an improved version of the one built for CNAO. It has been

optimised in order to minimise the magnet self-inductance, and to achieve a field uniformity of ± 0.2 % in the good field region [11]. The values calculated here are used for guidelines for defining a valid model.

From equations (1.8), (1.9) and (1.12) the beam rigidity $B\rho$ calculated for the heaviest particle species is 6.35 *Tm*. The deflection of 14 *mm* with longitudinal separation of 2.125 *m* as shown on Figure 1.6 corresponds to an angle of 6.6 *mrad*. Using (1.14) the total integrated field is calculated to be 0.0419 *Tm*. In the accelerator layout only about 400 *mm* are available for the integration of each magnet. Assuming a magnetic length of at least one gap height shorter than the total physical length, the effective length is chosen to be about 310 *mm*. This depends on the shape of the coil heads, the clearances between coils, yoke and endplates, and is later corrected to 318 *mm*. The magnetic induction B_0 in the magnet centre is 0.1365 *T*.

For protons at the lowest extraction energy of 60 *MeV* (corresponding to tissue penetration of 3.5 *cm*), p=0.341 *GeV/c*. The beam rigidity corresponding to this momentum is 1.137 *Tm*. Therefore the required B_0 will be 24 *mT*.

The excitation current can be calculated via (1.19). The magnet gap is 66 *mm*, which requires a total current of 7169 Ampere-turns. Using a 12 turn coil would require a nominal current of 597 *A*. For the lowest extraction the corresponding excitation current is 105 *A*. The magnet will need to preserve its linear characteristics in the entire range of excitation currents in order to allow beams of different energies to continue downstream unaffected.

The shape of the conductors as well as their location inside the magnet has a direct effect on the field quality, i.e. the homogeneity.

The preliminary mechanical model is shown on Figure 1.7. The main parameters of the magnet as defined in the technical specification are listed in Table 1.2 [12]. Some of the parameters differ from the initially calculated ones due to design and optimisation decisions taken at a later stage.
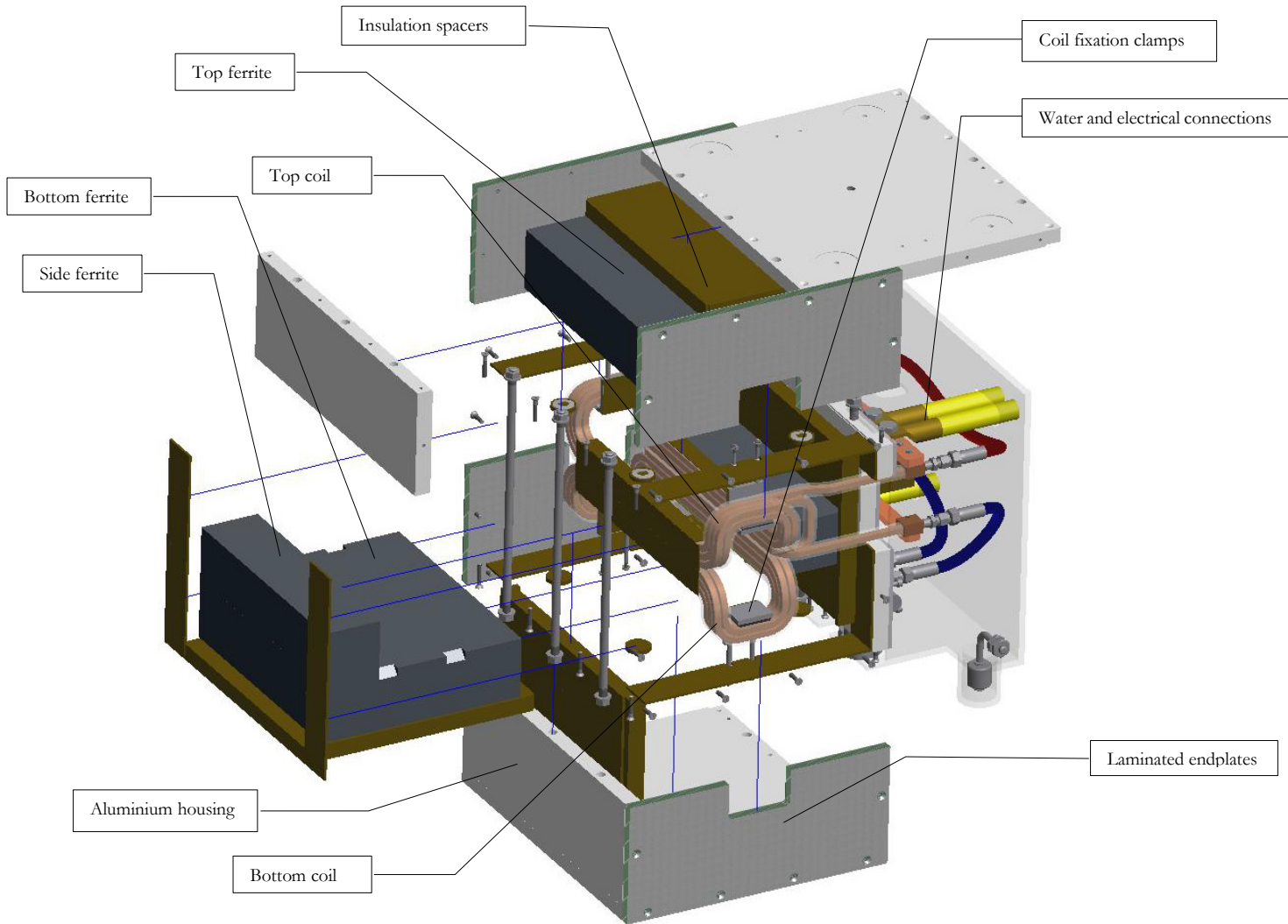
Figure 1.7. Exploded view of the chopper dipole preliminary design

Table 1.2. Chopper dipole parameters

	Chopper Dipole (4 units + 1 spare)
Name	MKC
Information	4 magnets powered in series by a programmable current controlled power converter with a resonant HV branch
Function	Device for turning beam on/off towards treatment rooms
Mounting and dismantling	Vertical
Effective magnetic length [m]	0.318 per magnet
Total physical length [m]	0.402 per magnet
Max. integrated field ∫Bdl [Tm]	0.0434 per magnet
Maximum field B_0 [T]	0.1364
Field orientation	Vertical
Maximum beam rigidity [Tm]	6.3464

Deflection angle [*mrad*]	6.6
Yoke Overall dimensions w × h × d [*mm³*]	Ferrite, window frame 258 × 216 × 290, 112 ×66 aperture
Pole gap [*mm*]	66
Clear aperture at magnet centre [*mm × mm*]	66 × 66
Vacuum chamber External dimensions h × v [*mm × mm*]	Ceramic, square, metallized 7 mm thick 64 × 64, rounded inner edges
Coil	2 half coils per magnet, electrically in series, water cooled in parallel, each coil a saddle shaped double layer pancake of 2 × 3 turns, i.e. 12 turns in total per magnet
Number of turns	12 (6 per half coil)
Conductor size [*mm × mm*]	8 × 8, with ø 4.0 *mm* water hole
Insulation space between turns [*mm*]	2
Good field region h × v [*mm × mm*]	Rectangle, 32.5 × 30
Field uniformity [*%*]	± 0.2
Current for max. field [*A*] (nominal)	600 (597 theoretical)
Voltage [*V*] (max.)	3500 (pulsed) & 50 (DC)
Current density [*A/mm²*]	11.8
Average turn length [*m*]	1.08
Cooling	Water
DC power dissipation [*W*]	2500 per magnet (1250 per half coil)
Magnet resistance [*Ω*]	0.0044 (0.0022 per half coil) (DC)
Estimated inductance [*μH*]	85 (per magnet)
Estimated stored energy [*J*]	15.2 (per magnet)
Maximum coil voltage to ground [*V*]	10000 DC
Rise time (2 % to 98 %) [*μs*]	250 (max): option of 90 (max)
Rise shape	Linear
Flat top [*μs*]	0 to DC
Peak to peak current ripple on flat top [*%*]	≤2.5 % of minimum value
Fall time (98 % to 2 %) [*μs*]	90 (max): option of 250 (max)
Fall Shape	Linear
Overshoot [*%*]	<5
Repetition rate	Baseline: DC to 20 *Hz*, continuous

Chapter 2

Modelling in Opera 3d

The full magnetic calculations have been executed in the TOSCA and ELEKTRA modules of Opera 3d by Cobham CTS Limited. The system relies on 3d finite element discretization of the domain for solving the partial differential equations that define the electromagnetic fields. The package consists of a geometric modeller, pre- and post-processor programs that provide the tools for geometry creation, and for the definition of complex conductor configurations, materials and characteristics, all displayed in a user-friendly graphical environment for interaction, visualisation and calculation of the input data and the simulation results. The Opera package contains nine specialized modules capable of solving a variety of problems, amongst which static and time-dependant electromagnetic fields and current flow, electromagnetic fields in linear and rotating machines, magnetization effects in permanent magnet materials, quenches in superconducting magnets, electrostatic fields with space charge created by charged particle beams, high-frequency electromagnetic fields, thermal and stress analyses. Furthermore these can be coupled so that several different physics phenomena can be fed back upon each other, such that the results of one simulation can be used as input data for another [13] [14] [15].

This chapter will demonstrate the capabilities of the Opera package for creating the 3d model geometry, defining the conductors, meshing and solving the problem, visualisation of results, calculations and export of data. The various design changes are detailed in Chapter 3. The TOSCA module has been used for the quasi-static magnetic calculations.

2.1   Building the geometry using the Modeller

The Opera software allows quick import/export of geometries from and to dedicated CAD systems for mechanical design such as Autodesk Inventor®, Solidworks®, and CATIA®. The built-in geometric modeller is however an equally powerful tool that allows creation of even the most complicated geometries, which is why it will be used for building the model. Once optimized, the geometry can be easily imported into a mechanical design system, and used as a base for the creation of production drawings.

2.1.1 Building the body of the magnet

The working axes of the co-ordinate system are chosen as follows (see Figure 1.3):

- The z axis is the longitudinal axis corresponding to the direction of propagation of the particle beam in the magnet gap;
- The y axis is the vertical axis, co-linear with the direction of the magnetic field between the poles of the magnet;
- The x axis is radial to the beam propagation and co-linear with the direction of the Lorentz force acting on the beam;
- The centre of the co-ordinate system is chosen to be the centre of the magnet gap.

For better visualisation the full body of the magnet is built, however at a later stage boundary conditions will be imposed. Using the symmetry only $1/8^{th}$ of the volume will be considered for meshing. This will significantly reduce the number of elements, hence the memory allocation and with this – the calculation times. It is possible to build the geometry in one octant, and using the *Copy>Reflect* command to create mirror images of the geometric entities on the desired axes.

The geometry of the magnet is relatively simple and will consist of several intersecting blocks of different material properties (Figure 2.1):

- Air – for the air gap and the insulation between the yoke and the magnet box (grey);
- Ferrite – for the magnet yoke (pale green);
- Aluminium – for the outside box (lime green);
- Iron – for the laminated endplates (blue).

The software prompts for six coordinates, a material name and a data storage level for each block. The latter will determine how intersecting blocks will hierarchically interact with each other, namely a higher storage level block will override a lower one in terms of material properties and element size and shape.
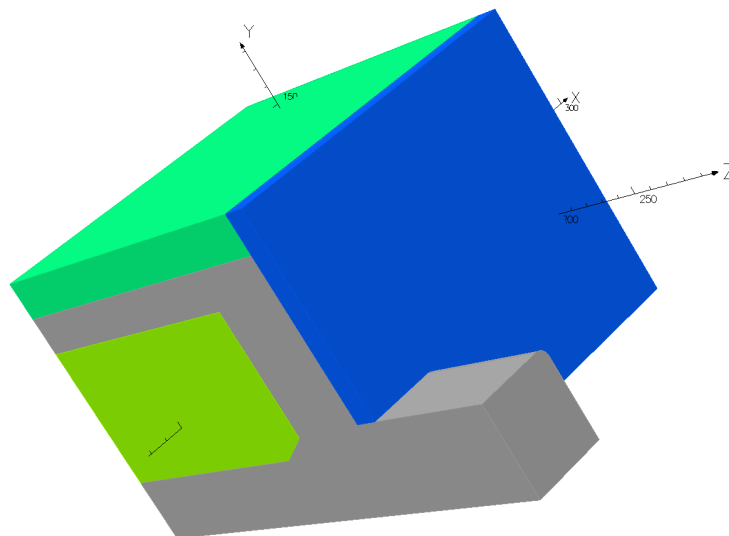

Figure 2.1. One eight of the magnet body

Geometric entities include:

- Bodies – they can be twisted, stretched, bent, and generally morphed. Overlapping bodies can be united, intersected, subtracted. Overlaps can be trimmed or cut away;
- Cells – can be formed from bodies, or the intersecting part of two bodies can be extracted as a cell, and turned into a separate body and be allocated different properties;
- Faces – can be offset or swept in any direction or along vectors, via rotation or via a defined path, thus changing the geometry of the cells and bodies they form, can be used for mesh control (for example layering to create fine meshes in regions of small skin depth), and for setting boundary conditions;
- Edges – those can be selected for blending two faces with a radius or filleting them with a chamfer. Both edges and faces can be used as centre points for working coordinate systems which are useful when creating complex geometries;
- Vertices – these are simple points which can be used for mesh control or for defining working coordinate systems.

Figure 2.1 shows the blocks defining the magnet body. The yoke is given the lowest value for the data storage level, and thus is been cut by the air gap in the bottom and the insulation on the top and sides. The size and shape of the yoke can be varied by varying the dimensions of the volumes enclosing it. Once all the bodies are created, individuals cells can be selected and set with the required mesh parameters, be given data labels for easier visualisation and analysis in the post-processor, and data storage levels can be changed if necessary. In the figure the edges of the intersecting blocks are hidden for better visualisation.

As shown earlier, the yoke is a simple rectangular ferrite block with a rectangular air gap in the middle and several chamfers for fitting the coil. The air gap is made to extend outside of the magnet body by about half the yoke length or three times the aperture height in order to be allocated a small element size which will provide more accurate results for the magnetic field.

2.1.2 Building the conductors

The modeller has a range of parameterized conductor geometries ranging from simple bars, to complete racetracks, bedsteads, and solenoids. The magnetostatic module TOSCA in 3d uses a formulation based on total and reduced scalar potentials, whilst ELEKTRA, that deals with low-frequency time-varied electromagnetic fields, uses total and reduced vector-potentials [15], [16]. There are two types of conductors used:

- Biot-Savart – they are used for predefined current sources and are not connected to external circuits. These conductors are not a part of the finite element mesh, and are defined within an area of reduced potential, which is set by default to all areas labelled "Air". Thus coil fields can be evaluated by direct integration via the Biot-Savart law, without creating a finite element mesh. They are current driven with a current density defined by its amplitude in steady state, or by scaling it with a drive function in a transient analysis. If the geometry is reduced by symmetry the coils must still be modelled as a complete set. All the Opera solvers can use this

formulation. For the chopper analysis Biot-Savart conductors are used with the current density defined via the function <*Current value / AREA*>;

- Filamentary and meshed conductors – these conductors are a part of the finite element mesh, and as such must be enclosed in volumes bearing total potential. They are connected to circuits and can be either voltage or current driven. As parts of the mesh they can exploit symmetries in the geometry. These conductor types shall not be used for the magnet simulations.

The full set of conductors is built using the bedstead command. Six bedsteads are overlapped to create the saddle shaped double layer pancake of 2×3 turns. Using the symmetry on the *z-x* plane the second coil is built using the *Reflection* command for each of the conductors (Figure 2.2).
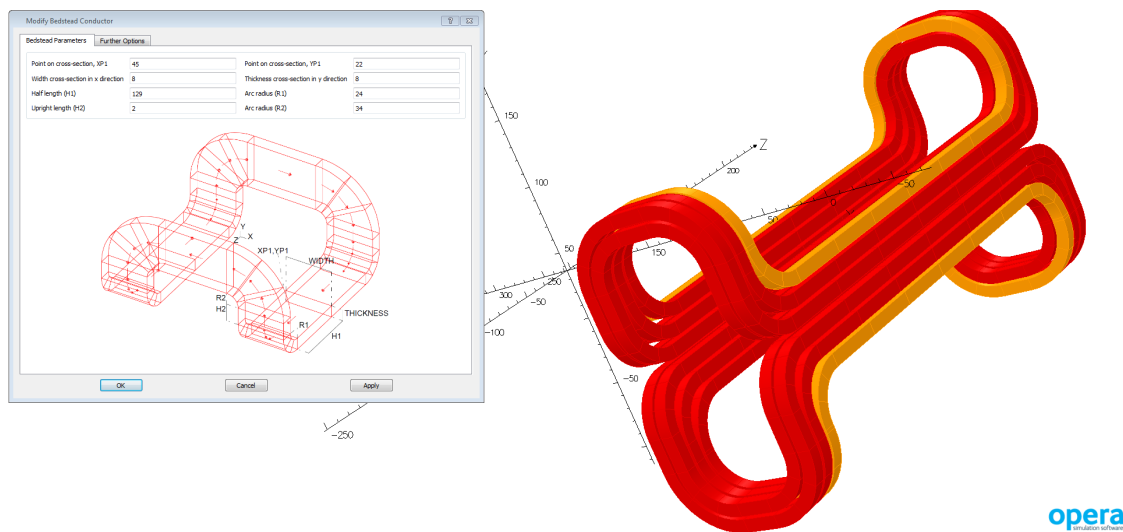
Figure 2.2. Creating the bedstead coil

The coil created in this manner doesn't take into account the inherent asymmetries introduced by the windings, nevertheless the results produced are extremely accurate as compared to the realistic model created for the final design acceptance (see 3.3). Each conductor is given the nominal current density defined with respect to the theoretical nominal current of 597 *A* via the command *597/AREA* (Biot-Savart current source), and assigned the same drive label. The conductor current density is thus 9.4 *A/mm²*. This is a simplifying assumption which does not take into account the hole for the water cooling, nor the skin effect during the rise and fall. The actual operational current density under nominal current will be 11.8 *A/mm²*. The drive label can later be used to add a scaling coefficient for the current, thus simulating different excitation levels, or be assigned a drive function in time-varying analyses.

2.1.3   Defining material properties
During the creation of the building blocks of the model material labels have been defined for the different cells. The analysis type can be chosen (TOSCA Magnetostatics), and this will permit each label to be assigned material properties:

- Ferrite – The magnets use a NiZn ferrite type CMD5005 produced by Ceramic Magnetics, Inc. The material is set as nonlinear and isotropic. The BH curve is provided by the manufacturer;
- Aluminium – Since it is non-magnetic it can be assigned with linear isotropic permeability, and relative permeability of 1. For the magnetostatic analysis executed in TOSCA it has essentially the same parameters as the default label Air;
- Steel – The 12 *mm* thick laminated endplates of the magnet use cold-rolled, final-annealed, non-grain oriented steel strips of the type isovac® 1300-100 of 1 *mm* thickness produced by Vöstalpine. The BH curve is provided by the manufacturer.

2.1.3.1 BH curves

BH curves are assigned to material labels with defined nonlinear properties. Opera has a large library of pre-defined magnetization curves, but also allows the user to input table data from manufacturers with both SI and CGS units allowed. Figure 2.3 and Figure 2.4 show the curves used for the simulations that are taken from material data sheets obtained from CMI and Vöstalpine.
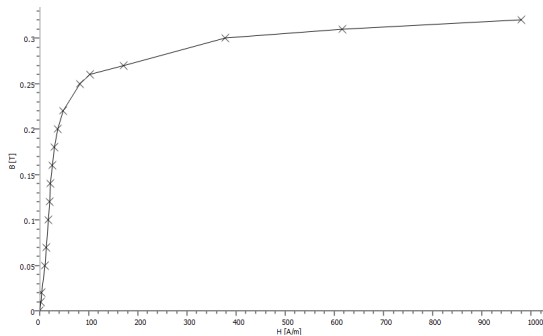
Figure 2.3. BH curve of ferrite CMD5005
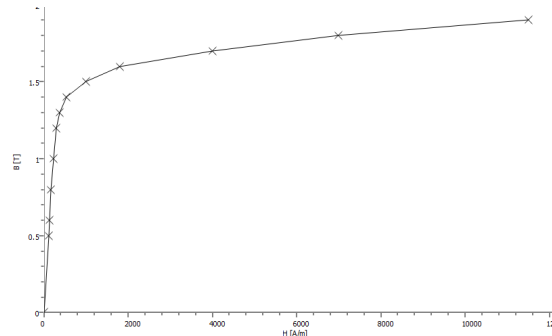
Figure 2.4. BH curve of steel isovac® 1300-100

In transient analyses Opera provides tools for modelling laminations by defining an anisotropic conductivity and a packing factor. For the steady state TOSCA simulations the endplates which consist of 12 stacked sheets of isovac® steel will be assumed as an isotropic single block.

2.2 Boundary conditions and symmetries

After the geometry has been created and the materials properties have been assigned, the area surrounding the magnet must be defined. In reality the fields extend outwards in free space to infinity, but in a finite element model the outer boundaries of the surrounding region must be defined at a finite distance from the geometry to limit the mesh size. This distance should be sufficiently far from the magnet as to not have an influence on the accuracy of the calculations. Alternatively a Kelvin transformation could be used to simulate infinity. For the TOSCA magnetostatic module the default boundary condition for the outer boundaries is the tangential magnetic. During this stage the symmetries are imposed in preparation for creating the mesh and the database for the solution.

The background region will be defined as a cylinder with scaling factors of 5 in the z axis, and 3 on the radius in the xy plane. The scaling is made with respect to the furthest vertex in the given direction. The symmetries are as follows:

- xy plane – Tangential magnetic;
- yz plane – Tangential magnetic;
- zx plane – Normal magnetic.

2.3 Finite element mesh

During the creation of the body of the magnet the different cells have been assigned mesh parameters defining element type (linear or quadratic), maximum element size and angle between elements. The element shape can be chosen between tetrahedral or hexahedral or a mix of the two.

For the analysis the magnet will be meshed with quadratic tetrahedral elements. Tetrahedral meshes can be used to mesh any geometry, and with correct application produce very accurate results. Mosaic (hexahedral or prismatic) meshes are advantageous with respect to their regularity which helps in faster volume meshing and matrix convergence, and are extremely useful in modelling eddy currents in thin sheets where the elements can be made parallel to the cell faces. Difficulties arise in the border region between hexahedra and tetrahedra, where pyramids are used to link the two mesh types. Building regular hexahedral meshes requires careful planning of the model with cell subdivision for mesh control, and is not always possible for any random geometry. Circular structures such as rotating machines are easily discretised using this method. Quadratic elements use an intermediate point between two nodes helping with definition of curved volumes.

The command *Create Model Body* creates a single body taking into account the properties of the overlapping cells, applies the symmetries and adds the background air region. Before that two additional air regions are added around the extended air gap and the magnet for smooth mesh transition between the regions of interest and the background air, and assigned the same mesh sizes as the regions they encompass. The maximum element sizes are selected as follows (Figure 2.5):

1. Endplate – 3 *mm*;
2. Aluminium box – 5 *mm*;
3. Air region between yoke and aluminium box – 5 *mm*;
4. Yoke – 5 *mm*;
5. Extended air gap – 2 *mm*;
6. Air region between yoke and endplate – 3 *mm*;
7. Additional air region surrounding gap – 2 *mm*;
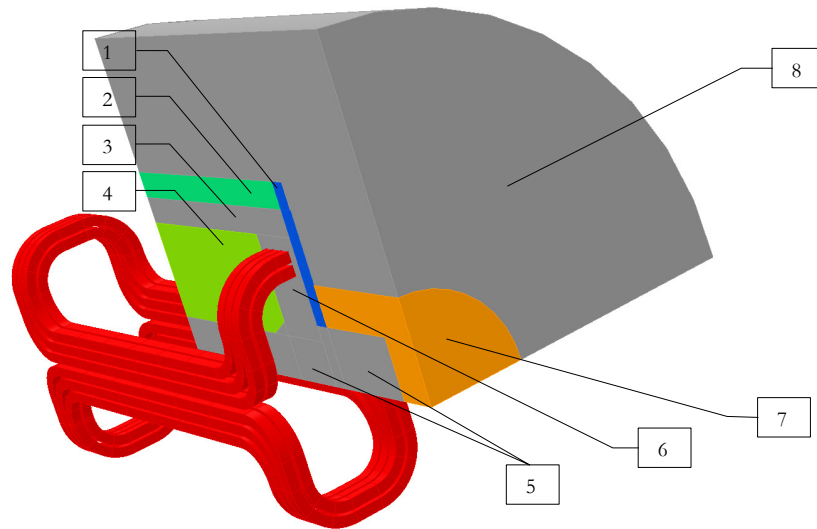8. Additional air region surrounding magnet – 5 *mm*.

Figure 2.5. Mesh size definition

The additional air regions will also allow the background air to be assigned with a coarser mesh, so that the total number of elements is kept as low as possible. The command *Generate Surface Mesh* defines the maximum element size for the background air region and any other regions without a specified element size. The maximum element size is set to 50 *mm*. The generator meshes all surfaces with triangular or quadrilateral elements. Figure 2.6 shows the meshed model body.
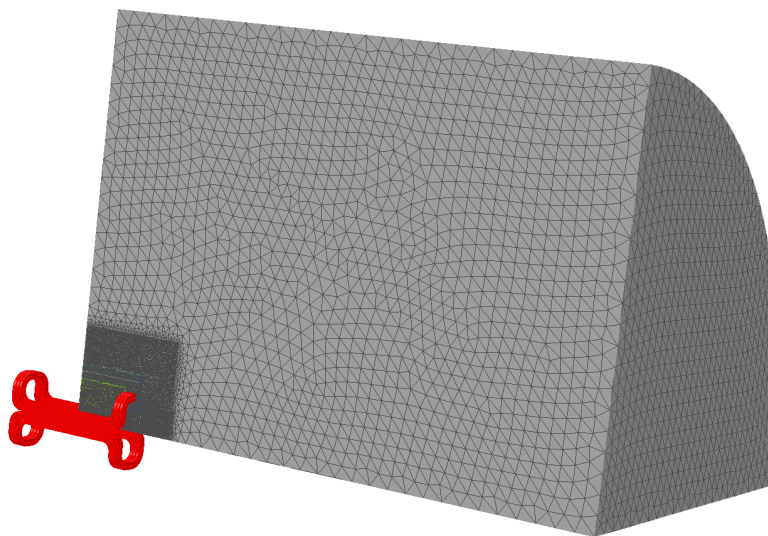
Figure 2.6. Meshed model body

A close-up of the magnet mesh is shown on Figure 2.7. An additional cell has been added in the magnet gap (shown in orange). It defines the good field region, and has been meshed with regular hexahedra of 1 *mm*. This allows for more precise post-processing and mapping of the field values, as exactly the nodal solutions can be exploited (without interpolation).
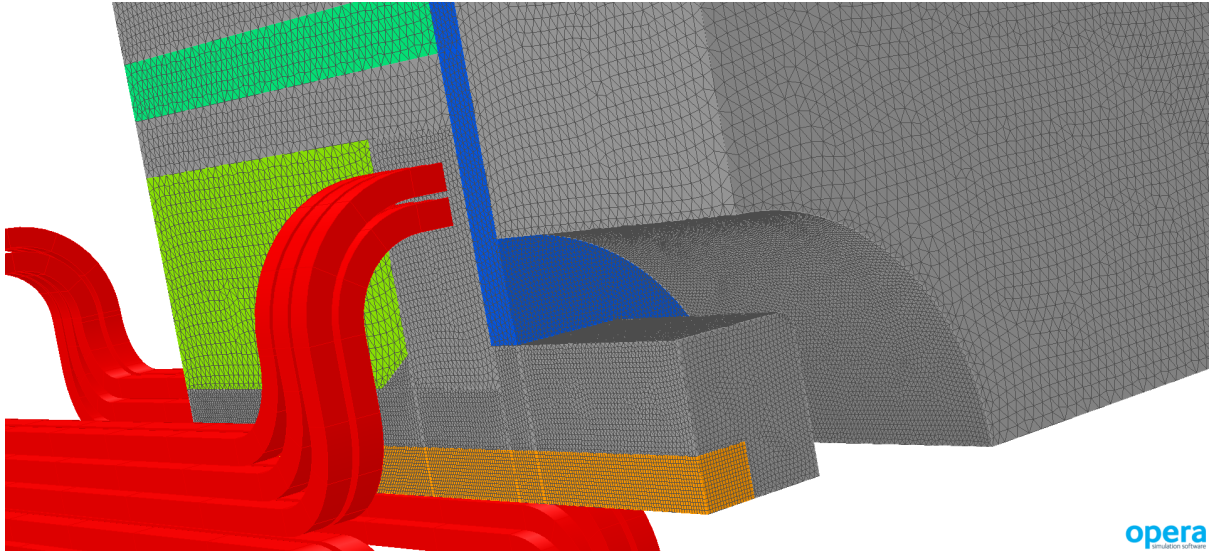
Figure 2.7. Mesh close up. Region 7 from Figure 2.5 is hidden for better visualisation.

Once the surface mesh is defined, the volume mesh can be created. For this model the volume mesh consists of a total of 1897297 nodes and 10860520 elements, out of which 10782775 quadratic tetrahedra, 68850 quadratic hexahedra, and 8895 quadratic pyramids linking tetrahedral and hexahedral meshes. The number of nodes can be reduced if the elements are set to linear.

The next step is to create the analysis database and to launch the solver. The *Magnetostatic Settings* tab can be used to force linear properties globally in the model or remain with the chosen nonlinear options. The maximum number of nonlinear iterations is set by default to 21 using the nonlinear Newton-Raphson update, but simple models as the one specified usually converge within 10 iterations [17]. The total computation time for the steady-state analysis carried out on a mid-range desktop machine (Intel *i5*, 8 GB RAM) can take between 1 and 8 hours. The RMS error for the analysis is in the region of 3.5 % and the weighted RMS error is 0.0175 %.

2.4   Post-processing

After the model has been solved the solution can be loaded in the post-processor and the results visualised. The main goal is to calculate the magnetic induction, the effective magnetic length, and to map the homogeneity in the good field region of the air gap. The results of the simulations are detailed in Chapter 3. The basic principles are briefly outlined in this section.

The post processor provides a number of instruments for field calculations, and extraction of data. Here only the most important ones used for the chopper dipole calculations are listed

The *Fields at a Point* command is used to extract the values of the magnetic induction at any given point, and is used to obtain the value of B_0 in the centre of the magnet gap.

The command *Fields on a Straight Line* is used to obtain the value of the field integral *Bdl*. It specifies a line along which a sum of the field values is taken in a discreet number of steps. For the MKC a line along the z axis starting at $\pm$ 300 *mm* is chosen. The values for the integral will be taken in 1000 points along this line. This will provide a smooth graph extending well outside the magnet gap, where the field values tend to zero. The small element size chosen guarantees a negligible error.

The integral in the centre of the gap will be taken as a reference point for the homogeneity evaluation diagram. It will be used to derive the effective magnetic length according to:

$$l_{eff} = \frac{B_0 dl}{B_0}$$ (2.1)

The values of the integrals will be calculated for an area of the gap slightly larger than the good field region in increments of 1 *mm*, and extracted to a text file via the *Table* command. This is then imported in a Microsoft Excel macro developed at the CERN Septa section in the 90's and improved over the years. The macro maps the *Bdl* values as a percentage of the nominal $B_0 dl$ according to:

$$\Delta B = \frac{B_0 dl - Bdl}{B_0 dl}\ 100\%$$ (2.2)

This displays a colour code of the field homogeneity as a percentage of the nominal integrated field. It is the main tool used for evaluation of the field homogeneity.

The post-processor allows for an integration of the stored energy in the magnetic field. This is subsequently used to derive the magnet inductance according to the well-known formula:

$$W = \frac{1}{2} L i^2$$ (2.3)

Chapter 3

Optimisations

The main goal of this work was, as previously stated, to migrate the theoretical design into a mechanical model with a full set of production drawings, and to ensure that a working magnet can be built, with parameters conforming to the technical specification with the focus being on preserving the required field homogeneity.

In this chapter, the various design improvements and modifications will be examined in detail. In the first part, a study of several possible coil insulation architectures is presented. This is followed by an investigation into the effects of the brazing joint for the ceramic vacuum chamber, which is relevant to the design of the latter, and the mechanical integration of the magnet in the accelerator. In the third part the final coil geometry is defined, and in the last – the shape of the ferrite yoke. All the derived dimensions have been incorporated into the definitive design and the production drawings.

3.1   Coil insulation schemes

Two millimetres of insulation are inserted between adjacent turns of the MKC coil [12]. The spacing between conductors is 2 *mm*. In order to incorporate more insulation, to ensure long life at the maximum specified repetition rate and to ensure that the magnet can be opened, a recalculation of the field homogeneity is required. Three alternative insulation schemes have been proposed and studied [18].

Figure 3.1 shows a drawing of the initial MKC coil design:
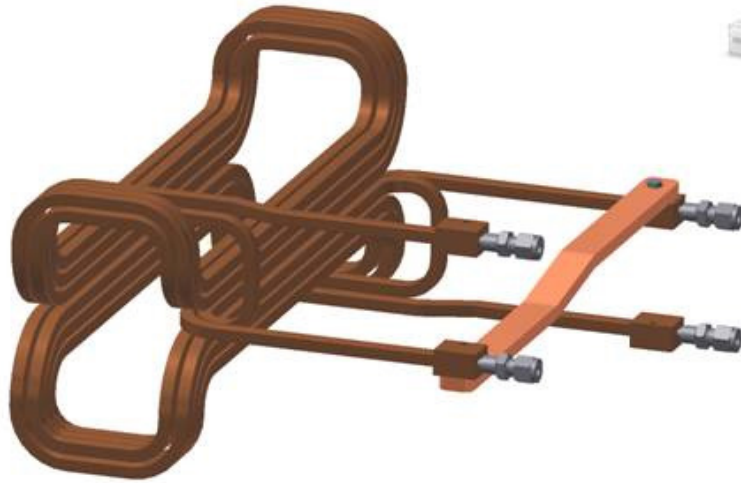
Figure 3.1. Initial MKC coil design

Figure 3.2 shows the current flow direction in the top bedstead winding, and the distance between the go and return columns:

70 mm
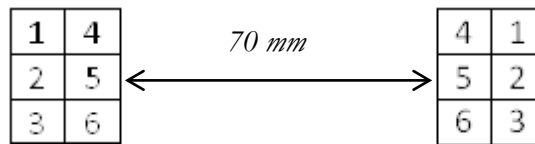
Figure 3.2. Top bedstead winding

For this:

- Adjacent windings of a bedstead coil, separated vertically, have a potential difference approximately equal to one-sixth of the bedstead coil voltage;
- Adjacent windings of a bedstead coil, separated horizontally, have a potential difference approximately equal to one half of the bedstead coil voltage.

Hence it is important to ensure adequate insulation between adjacent, horizontally separated windings.

As mentioned above, [12] specifies a total of 2 *mm* of insulation between adjacent horizontal and vertical turns of the MKC coil (Figure 3.3). Three alternative insulation schemes have been considered and simulated in an attempt to provide for increased high voltage hold off capacity between conductor columns. These alternatives are discussed in the following paragraphs.
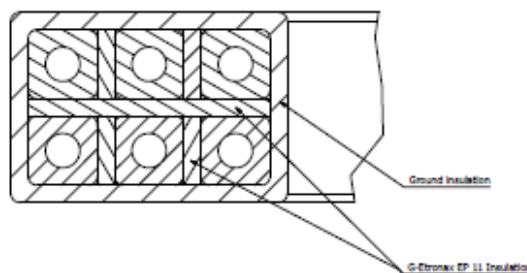
Figure 3.3. Initial configuration. Copyright MedAustron©, Danfysik©

3.1.1.1 Alternative 1

Figure 3.4 represents a schematic layout of the coil insulation for the first alternative as per [12].

- Each conductor is wrapped with 1 *mm* glass-fibre tape (shown in green in Figure 3.4);
- 0.5 *mm* thick glass fibre tape is wrapped around each 3-turn column (shown in red in Figure 3.4);
- 0.5 *mm* thick glass-fibre tape is wrapped around each 6-turn coil (shown in blue in Figure 3.4).

The insulation between horizontally displaced adjacent conductors in a coil is increased by 1 *mm* which increases separation between adjacent columns in the horizontal plane from 2 *mm* to 3 *mm*. For a given thickness of the ferrite yoke the total magnet width is thus increased by 2 *mm*, but the gap aperture height of 66 *mm*, and the 70 *mm* distance between go and return columns remain unchanged.
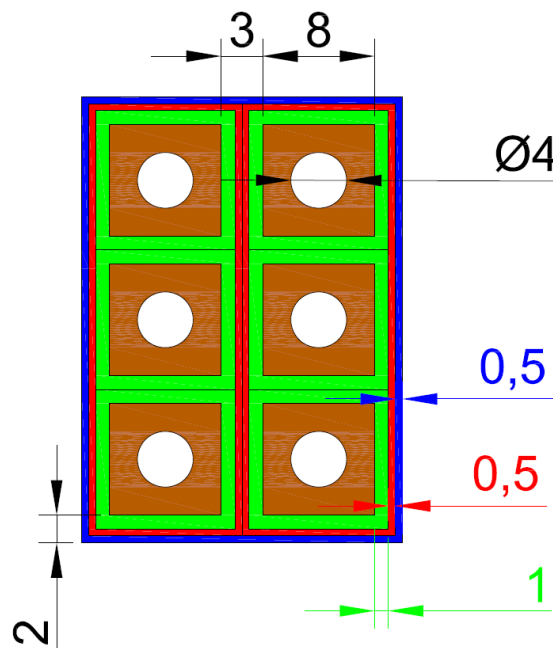
Figure 3.4. Alternative 1

3.1.1.2 Alternative 2

The second alternative is based on the CNAO configuration. Figure 3.5 shows the layout.

- Each conductor is wrapped with 1 *mm* glass-fibre tape (shown in green in Figure 3.5);
- 1 *mm* thick glass fibre tape is wrapped around each 3-turn column (shown in red in Figure 3.5);
- 1 *mm* thick glass-fibre tape is wrapped around each 6-turn coil (shown in blue in Figure 3.5).

The insulation between horizontally and vertically displaced adjacent conductors in a coil is increased from 2 *mm* to 4 *mm*. In addition the distance between the go and return columns is increased to 72 *mm*. The total magnet width needs thus to be increased by 8 *mm*, and the aperture height – by 4 *mm* to 70 *mm*.
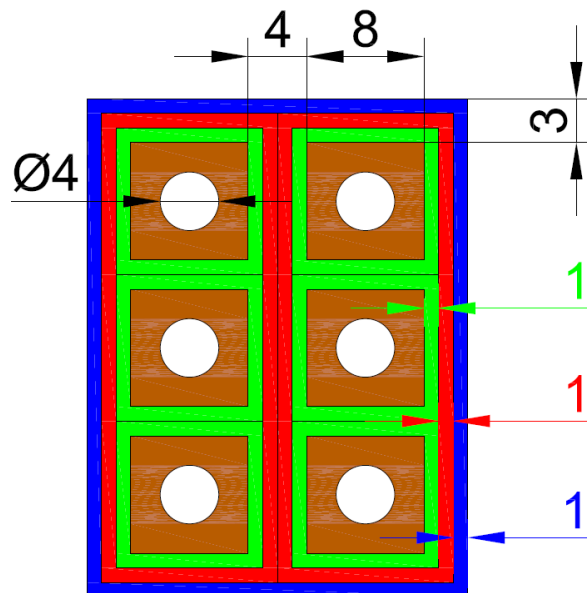
Figure 3.5. Alternative 2

3.1.1.3 Alternative 3

Figure 3.6 shows the third alternative.

- Each conductor is wrapped with 1 *mm* glass-fibre tape (shown in green in Figure 3.6);
- 0.5 *mm* thick glass fibre tape is wrapped around each 3-turn column (shown in red in Figure 3.6);
- 0.5 *mm* thick glass-fibre tape is wrapped around each 6-turn coil (shown in blue in Figure 3.6);
- 1 *mm* of glass-fibre is inserted between adjacent 3-turn columns (shown in pale blue in Figure 3.6).

Insulation between horizontally displaced adjacent conductors in a coil is increased by 2 *mm*, whilst retaining the 70 *mm* separation between go and return columns, and the 66 *mm* aperture gap height. For a given thickness of the ferrite yoke the total magnet width will have to be increased by 4 *mm*.
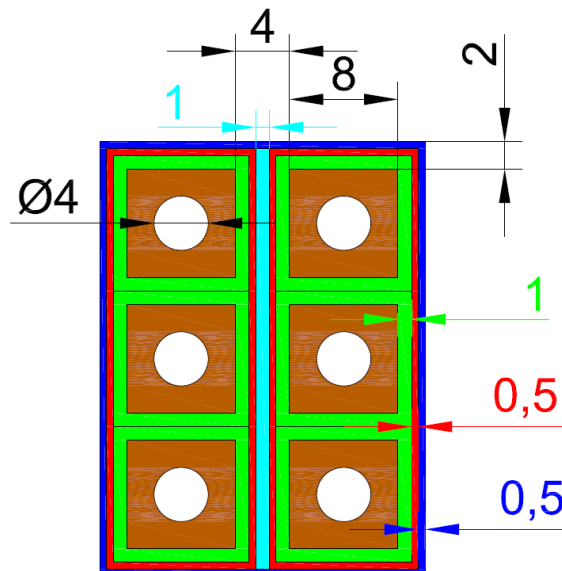
Figure 3.6. Alternative 3

3.1.2 Results from the simulations

Note: in order to interpret the predictions, and to estimate the uniformity of the deflection angle, the predicted flux density is integrated (for a given x and y coordinate) with respect to z. This neglects the deflection angle (6.6 *mrad*) which, for a beam rigidity of 6.346 *Tm* and an effective length of 0.318 *m*, would result in a deflection in the x direction of ~ 2.1 *mm* at the downstream end of the magnet.

3.1.2.1 Simulations with increased magnet overall dimensions

Table 3.1. Summary of simulation results
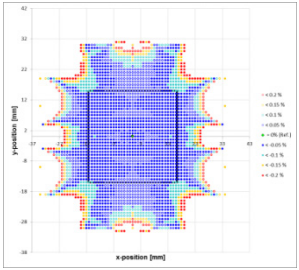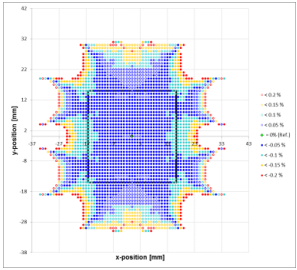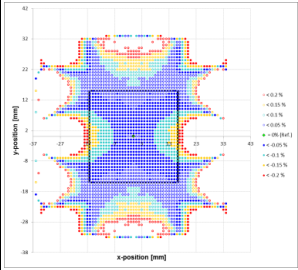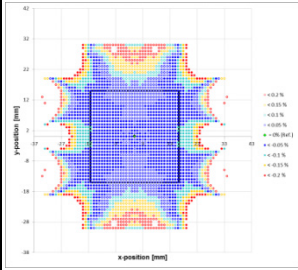
	Baseline configuration	Alternative 1		Alternative 2		Alternative 3	
		Value	Deviation	Value	Deviation	Value	Deviation
$\int Bdz$ [Tmm]	44.9186	44.9175	0.00%	42.3392	−6.09%	44.8947	−0.05%
B_0 [T]	0.1365	0.1365	0.00%	0.1287	−6.06%	0.1365	0.00%
L_{eff} [mm]	329.1315	329.1260	0.00%	329.0218	−0.03%	328.9615	−0.05%
W [J]	15.0486	15.1482	0.66%	14.8730	−1.18%	15.2339	1.22%
L [μH]	84.45	85.004	0.65%	83.46	−1.19%	85.49	1.22%

Table 3.1 summarizes the results from the simulations compared to the initial configuration. Alternative 2 shows a 6 % decrease in maximum and integrated field: hence, to obtain the same flux density, the current would need to be increased by 6 %. No change in current is required for alternatives 1 and 3, thus these are the preferred alternatives.

The integrated field, as mentioned above, is proportional to the deflection angle. The percentage deviation of the proposed alternatives from the original is given by:

$$\Delta B = \left(1 - \frac{\int Bdz_{alternative}}{\int Bdz_{initial}}\right) *100 \ \% \tag{3.1}$$

In order to visualise the difference in magnetic field between the proposed alternatives and the initial coil configuration the relative error for the integrated field values has been compared to a reference point (Bdz in the middle of the magnet for the initial configuration) according to:

$$\Delta B = \frac{\int Bdz_{alternative}}{\int Bdz_{initial}} \int Bdz_{0_{initial}} \tag{3.2}$$

The plots will then show the difference between the field values for the new configurations as compared to the B_0dl value for the initial layout. The resulting plots are shown on Figure 3.7, Figure 3.8, and Figure 3.9.
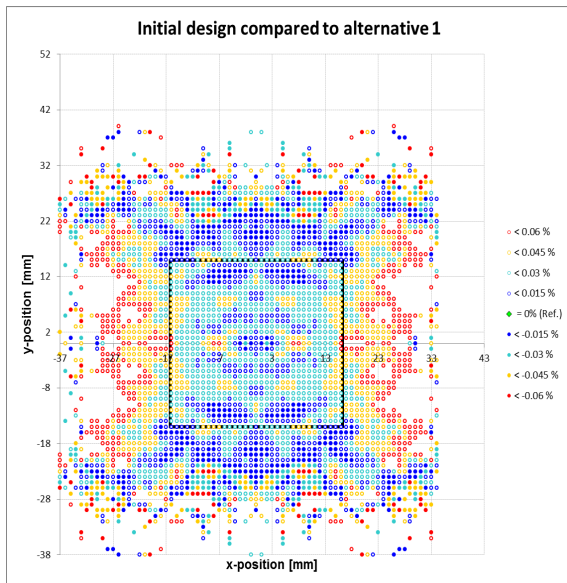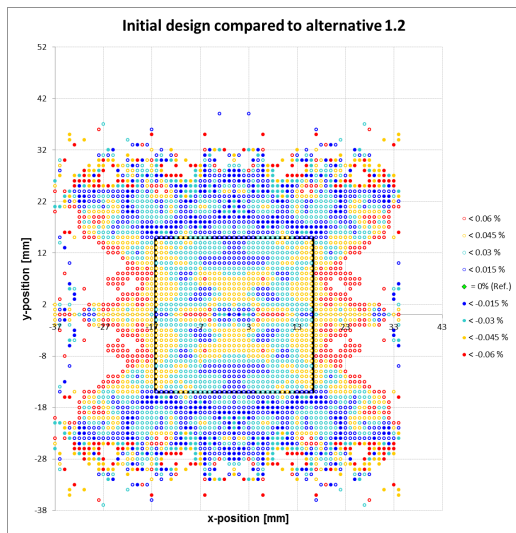

Figure 3.7. Alternative 1 deflection compared to initial layout (up to 0.06 % deviation inside good field region)
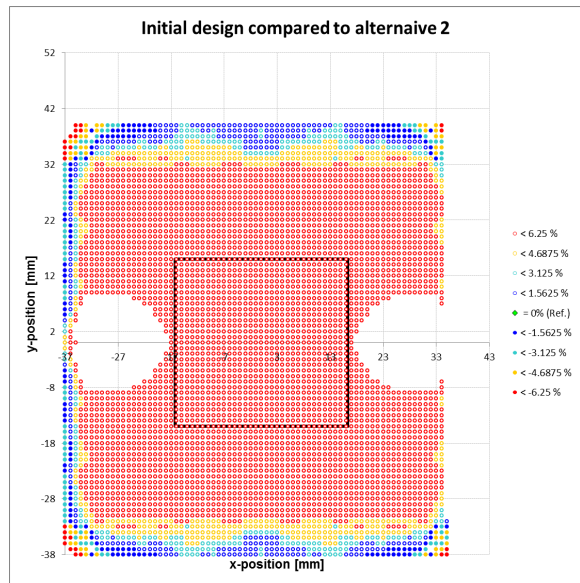
Figure 3.8. Alternative 2 deflection compared to initial layout (6.25 % deviation inside good field region)
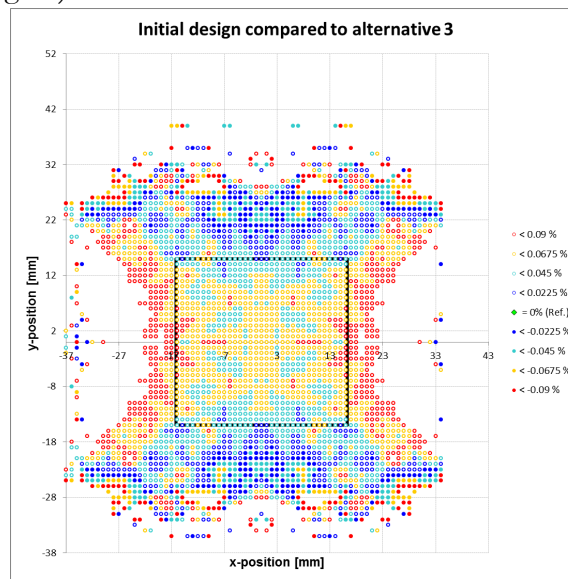
Figure 3.9. Alternative 3 deflection compared to initial layout (up to 0.09 % deviation inside good field region)

3.1.2.2   Simulation retaining the magnet overall dimensions

Table 3.2 represents alternatives 1 and 3, but in this case the magnet overall dimensions remain unchanged, while the gap width is increased by 1 *mm* and 2 *mm* respectively in order to accommodate the coil with more insulation. Alternative 2 has shown a significant deviation from the reference point and was not included in the simulations.

Table 3.2. Comparison of the initial configuration and the design with increased aperture width to maintain overall magnet dimensions

	Baseline configuration	Alternative 1.2		Alternative 3.2	
		Value	Deviation	Value	Deviation
$\int Bdz\ [Tmm]$	44.9186	44.9183	0.00%	44.9077	−0.02%
$B_0\ [T]$	0.1365	0.1365	0.01%	0.1365	0.00%
$L_{eff}\ [mm]$	329.1315	329.1083	−0.01%	329.0472	−0.03%
$W\ [J]$	15.0486	15.1441	0.63%	15.2289	1.18%
$L\ [\mu H]$	84.45	84.98	0.62%	85.46	1.18%

Figure 3.10 and Figure 3.11 show the subtracted plots.

Figure 3.10. Alternative 1.2 deflection compared to the initial layout (0.06 % max. deviation inside good field region)
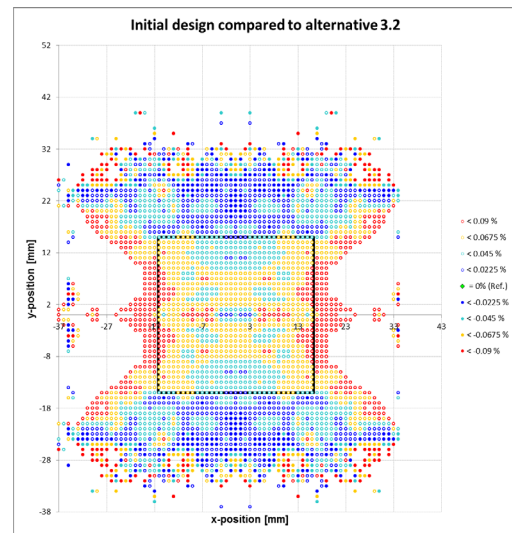
Figure 3.11. Alternative 3.2 deflection compared to the initial layout (0.09 % max. deviation inside good field region)

3.1.3   Field values along beam radial direction

Subsequently field values in the beam radial direction were taken in order to study the impact of the different coil geometries on the magnetisation levels inside the ferrite yoke. Figure 3.12 shows the area of the good field region, 32.5 *mm* x 30 *mm,* in the middle of the magnet aperture.
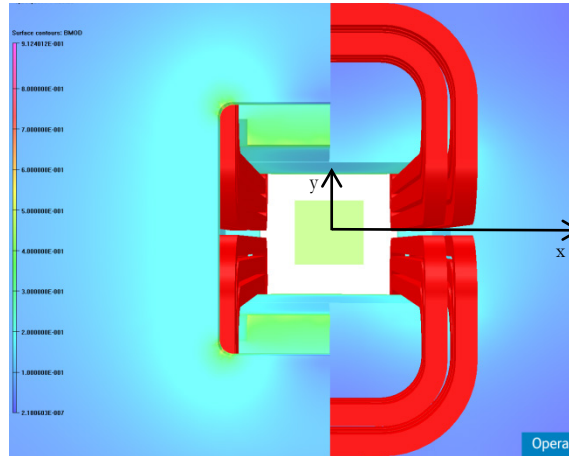
Figure 3.12. Good field region

The following figures show field value plots for *Bmod* along the horizontal (x) axis in the middle of the magnet at different offsets on the vertical (y) axis for alternatives 1.1, 1.2, 3.1, and 3.2 compared to the baseline design. The plots are taken from the centre of the magnet gap to the outer edge of the ferrite as shown in the background snapshot. The orange line represents the outer limit of the good field region in the x direction (x = 16.25 *mm*)
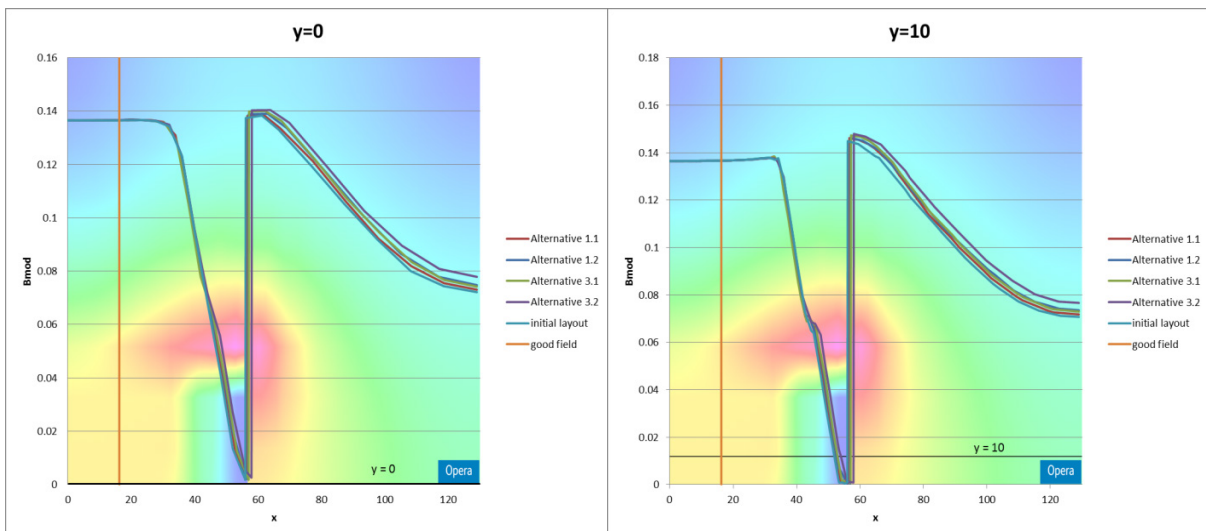
Figure 3.13. *y=0, z=0*   Figure 3.14. *y=10, z=0*
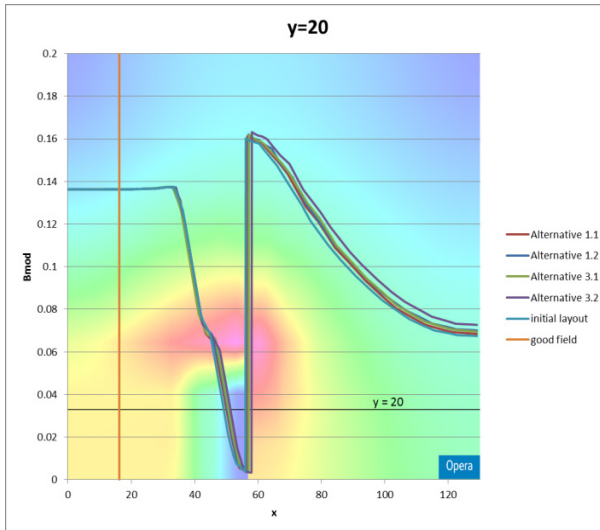
Figure 3.15. *y=20, z=0*
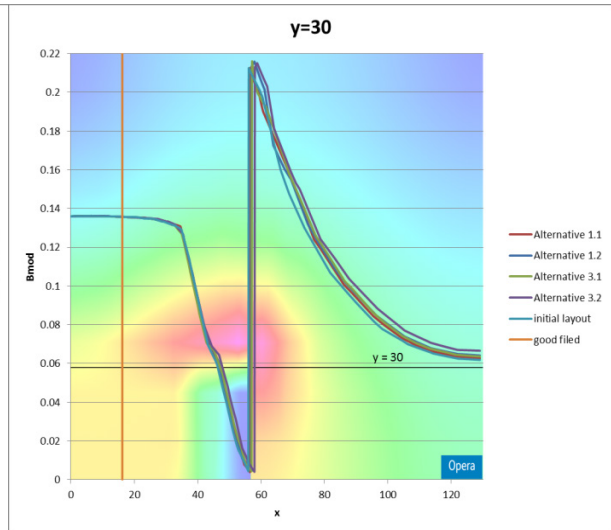
Figure 3.16. *y=30, z=0*
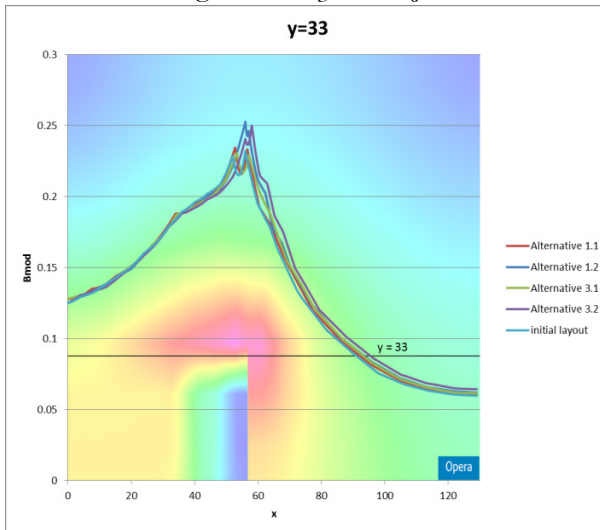
Figure 3.17. *y=33, z=0* (aperture edge)
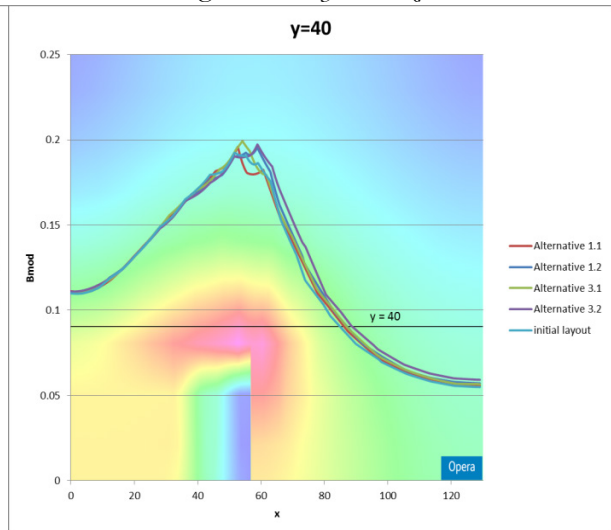
Figure 3.18. *y=40, z=0*

The graph on Figure 3.19, and the histogram on Figure 3.20 show the field values for the region examined above for alternative 1. The flux density values above 200 *mT* have been excluded from the histogram to show the level of saturation in the magnet yoke.
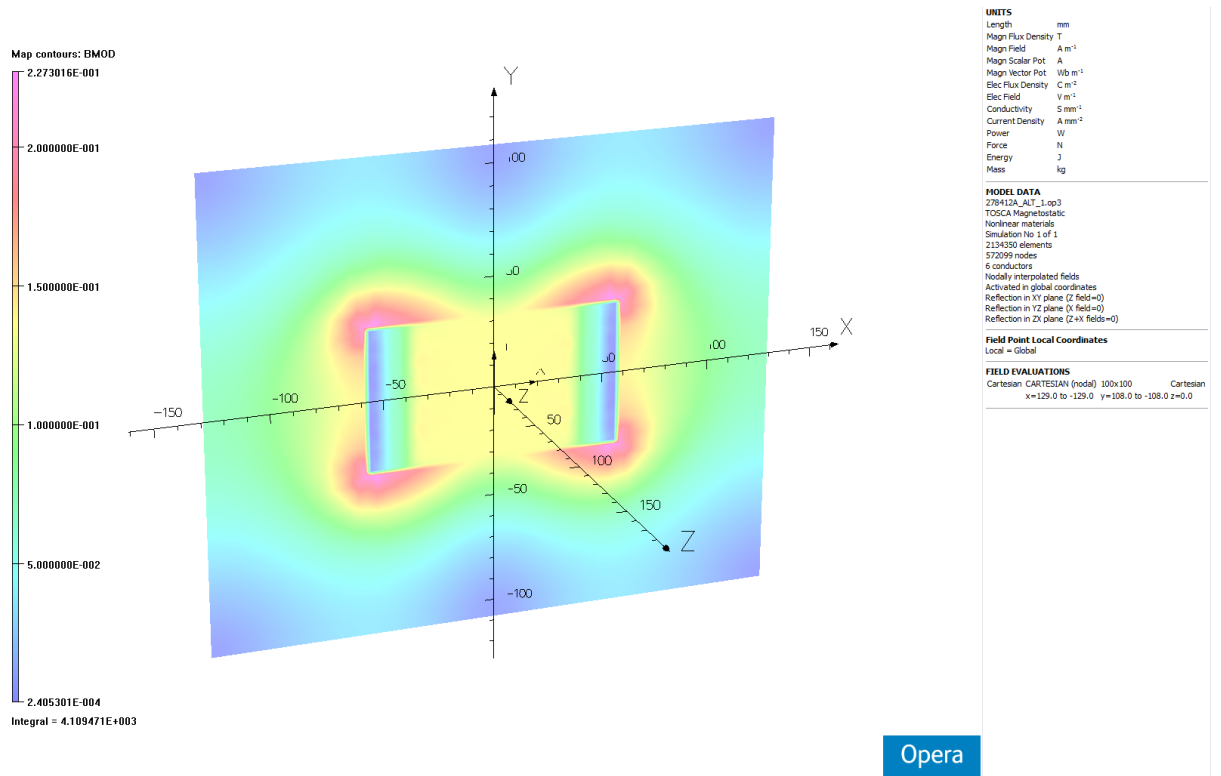
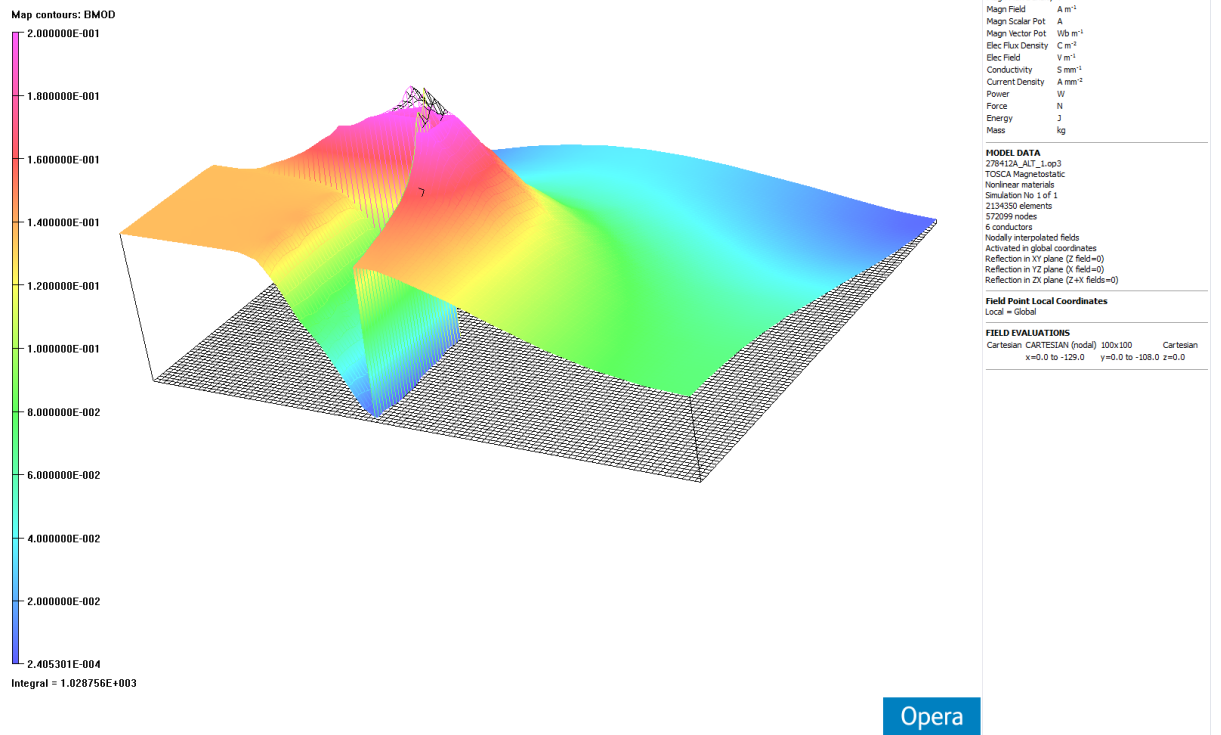Figure 3.19. Flux density in magnet centre for alternative 1

Figure 3.20. Histogram of a quarter of the examined region for alternative 1

3.1.4 **RMS field inhomogeneity**

Table 3.3 shows a comparison of max and RMS deflection inhomogeneity values in the good field region of the aperture. The RMS value has been calculated according to (3.3), and the value obtained has been compared to the point of reference (*Bdz* in the magnet centre) for each case to give the RMS error.

$$Bdz_{RMS} = \sqrt{\frac{1}{n}\sum_{i=1}^{n} Bdz_i^2} \qquad (3.3)$$

It can be seen that increasing the gap width (alternatives 1.2 and 3.2) increases the RMS deflection inhomogeneity inside the required good field region.

Table 3.3. RMS values of integrated deflection in the good field region

	Baseline configuration	Alternative 1	Alternative 1.2	Alternative 2	Alternative 3	Alternative 3.2
Integrated field [*Tmm*]	44.912	44.903	44.900	42.327	44.890	44.889
RMS deflection inhomogeneity	0.01%	0.03%	0.04%	0.03%	0.01%	0.04%
Max deflection inhomogeneity	0.08%	0.10%	0.08%	0.21%	0.10%	0.11%

3.1.5 Good field region inhomogeneity

The following figures show a zoom of the good field region for the initial coil configuration and the proposed alternatives.
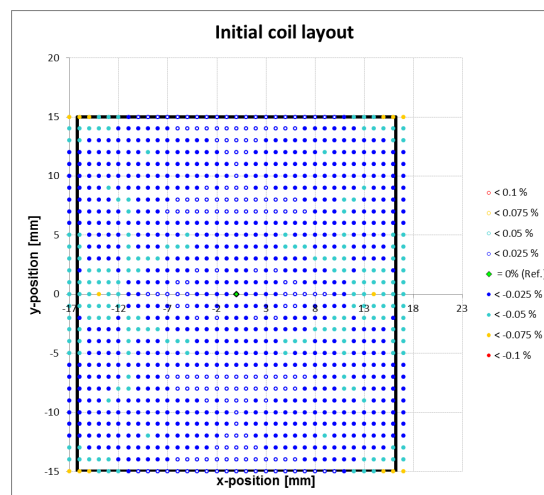
Figure 3.21. Deflection inhomogeneity for initial insulation layout
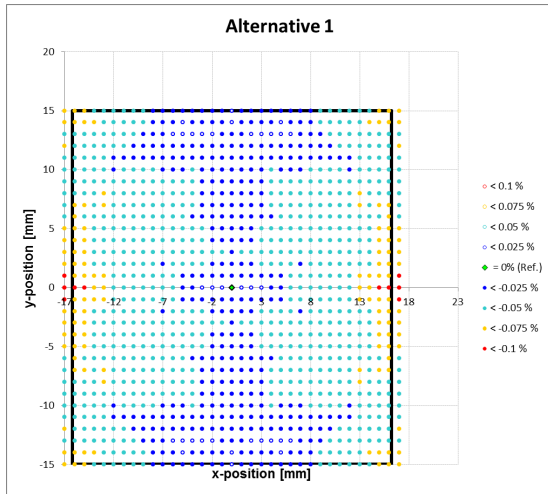
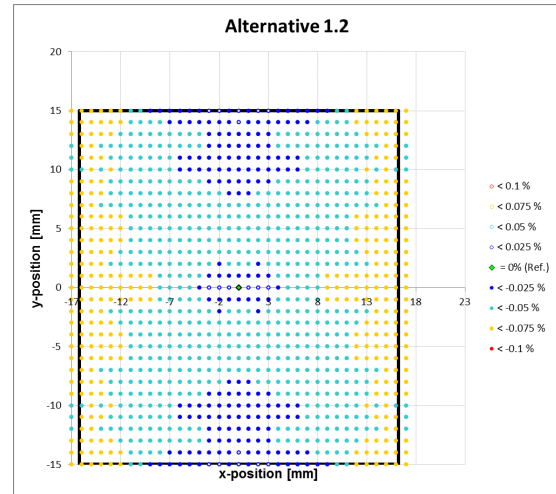Figure 3.22. Deflection inhomogeneity for alternative 1 (magnet width increased by 2 *mm*)

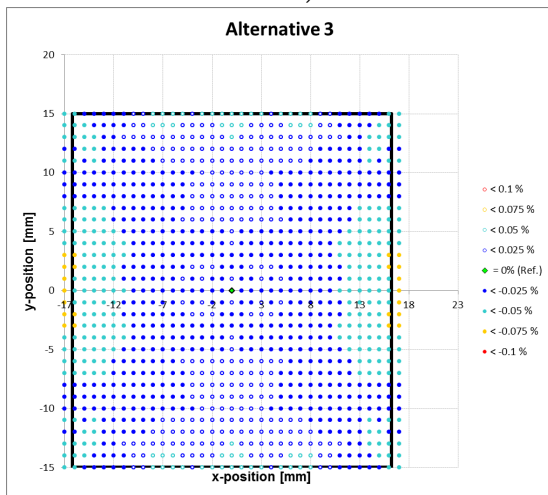Figure 3.23. Deflection inhomogeneity for alternative 1.2 (yoke shaved-off by 2 *mm*)

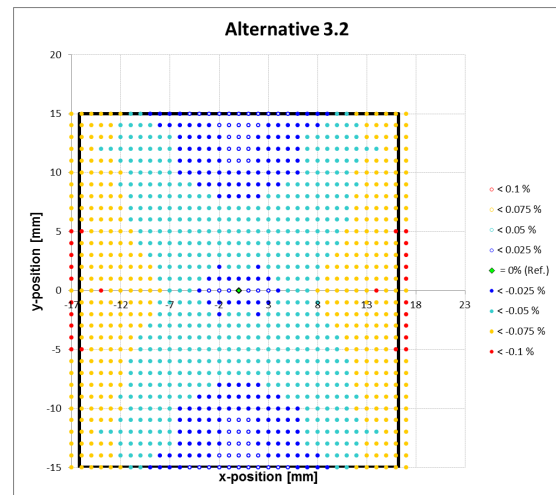Figure 3.24. Deflection inhomogeneity for alternative 3 (magnet width increased by 4 *mm*)

Figure 3.25. Deflection inhomogeneity for alternative 3.2 (yoke shaved-off by 4 *mm*)

3.1.6   Conclusions on coil insulation optimisations

The different coil insulation variants examined provide improvement in the high voltage hold off capacity of the coil insulation in case a higher pulse rate (hence a higher applied voltage) is required (option for the future). However the initial layout with the least insulation will be preserved as it produces the best field homogeneity. The magnet overall dimensions will remain unchanged. The insulation between conductors will be made by inserting 2 *mm* sheets of G-Etronax EP11 glass-fibre epoxy. For the ground insulation glass fibre tape will be wound around the coil, and the assembly will be vacuum-impregnated in epoxy resin.

3.2 Effects of brazing joint on the ceramic vacuum chamber

The particles in the accelerator are interacting with residual gas atoms and molecules via elastic and inelastic collisions. This results in beam emittance growth and beam loss, which in return leads to a decrease in beam quality and lifetime. For these reasons the beam path is kept under ultra-high vacuum by means of a continuous beam pipe. The MedAustron beam pipe is mostly made in undulated Inconel®, which is magnetically transparent for the static and quasi-static fields typically found in the main magnets of the accelerator. However, during a fast current ramp eddy currents will be induced in a beam pipe made of conductive material like stainless steel, and the fields associated with these eddy currents will prevent the external fields from penetrating the vacuum chamber. Due to the design requirements of fast-pulsed operation, the MKC uses a ceramic vacuum chamber in order to avoid field perturbations during the transient state. The chamber's inner walls are coated with a thin layer of titanium in order to provide a conductive path for the beam image current that is induced by the circulating beam, whilst allowing the external magnetic fields to penetrate without an increase in rise time. The conductive layer helps reduce the impedance seen by the beam as it travels along the chamber, but most importantly, it helps avoid the build-up of charges of ionised gases on the inner walls of the vacuum chamber.

The ceramic vacuum chamber is terminated at both ends by stainless steel flanges. These are brazed to the chamber using Kovar® for the metal-to-ceramic interface due to its specific temperature expansion coefficient that closely matches that of the Alumina ceramic, its good weldability to stainless steel, and its low outgassing rates. As a Fe-Ni alloy, Kovar® has a very high magnetic permeability, and the brazing joint, being in close vicinity to the ends of the magnet will influence the end fields with a direct impact on the effective magnetic length.

Two possible configurations of the joining between the chamber and the flanges are examined. For each of the two configurations simulations were made for several different offsets between the magnet endplates and the brazing joints, corresponding to different vacuum chamber lengths. The aim of the analysis is to specify a joining technique and to define a vacuum chamber length that does not affect the effective length of the magnet, and can still be integrated in the machine [19].

3.2.1.1 Model with metallic joint brazed to ceramic vacuum chamber – case 1.

The first possible configuration vacuum chamber – brazing is shown on Figure 3.26 and Figure 3.27. The magnet uses a rectangular chamber with rounded inner walls as shown in grey on the figure. The brazing joint is shown in purple, whereas the stainless steel flange, being non-magnetic is excluded from the magnetostatic simulations altogether.
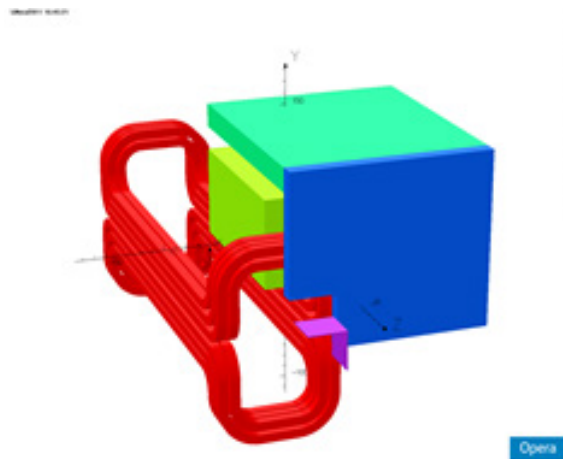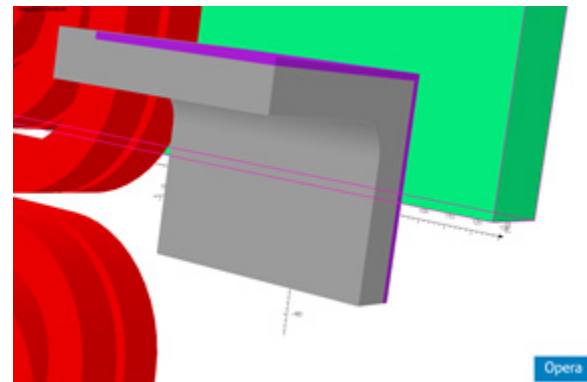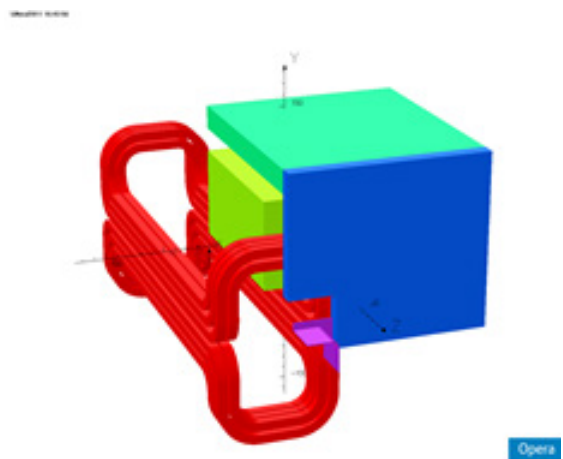

Figure 3.26. One eight of magnet and brazing
Figure 3.27. Vacuum chamber and brazing

3.2.1.2 Model with metallic joint brazed to ceramic vacuum chamber – case 2.

The configuration vacuum chamber – brazing is shown on Figure 3.28 and Figure 3.29

Figure 3.28. One eight of magnet and brazing
Figure 3.29. Vacuum chamber and brazing
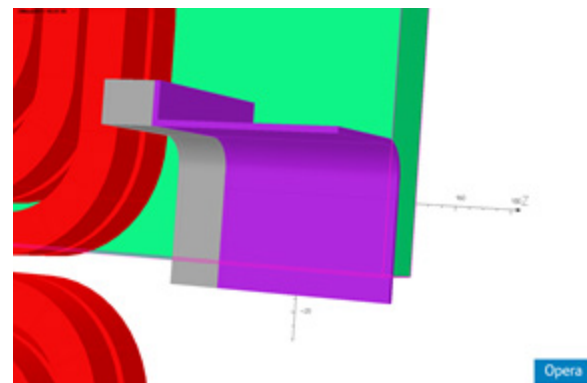
Both cases were simulated in TOSCA magnetostatic. The drive current was set to 597 A. The BH curve for the metal used in the brazing is shown on Figure 3.30 [20]. A first approximation of a transient simulation was made as well. Setting a low linear permeability of the metal joint will allow flux from the fringe fields to pass through it, which would give an adequate idealization of an eddy current induced flux in the joining piece.
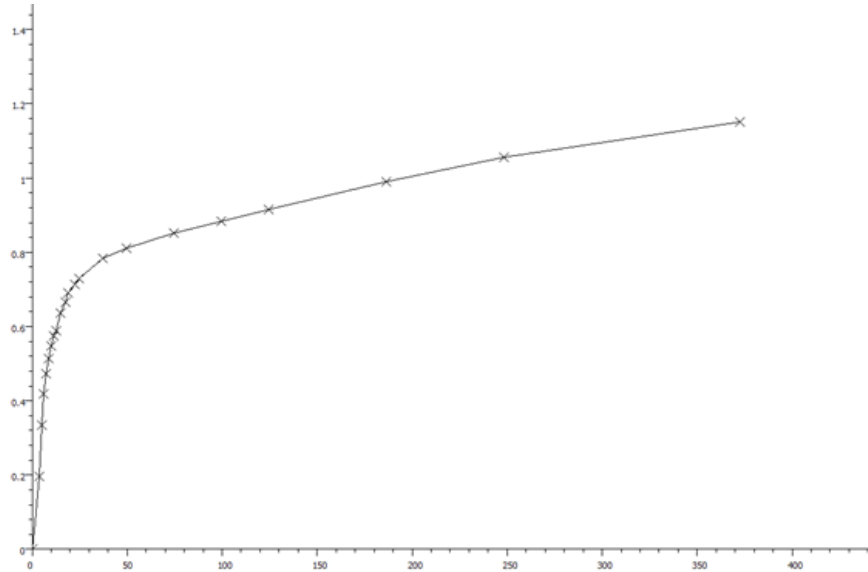
Figure 3.30. BH curve for metallic joint – 50-50 Fe-Ni

3.2.2 Results from static simulations

Table 3.4 shows the evaluated field qualities at offset distances from the laminated endplate of 1 *mm*, 3 *mm*, 5 *mm*, 7 *mm*, and 11 *mm* for the static case and the transient approximation:

- Case 1.1 – 1 *mm* thin metallic joint with nonlinear properties, BH-curve labelled Mu Metal;
- Case 1.2 – 1 *mm* thin metallic joint with linear properties *μ=0.001* (transient approximation);
- Case 2.1 – 1 *mm* thin metallic joint with nonlinear properties, BH-curve labelled Mu Metal;
- Case 2.2 – 1 *mm* thin metallic joint with linear properties *μ=0.001* (transient approximation).

Figure 3.31 gives the reference field quality plot for the magnetostatic case without brazed joint.
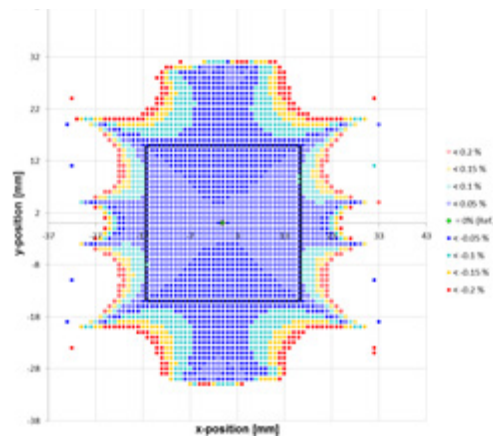
Figure 3.31. Field quality plot – no braze

47

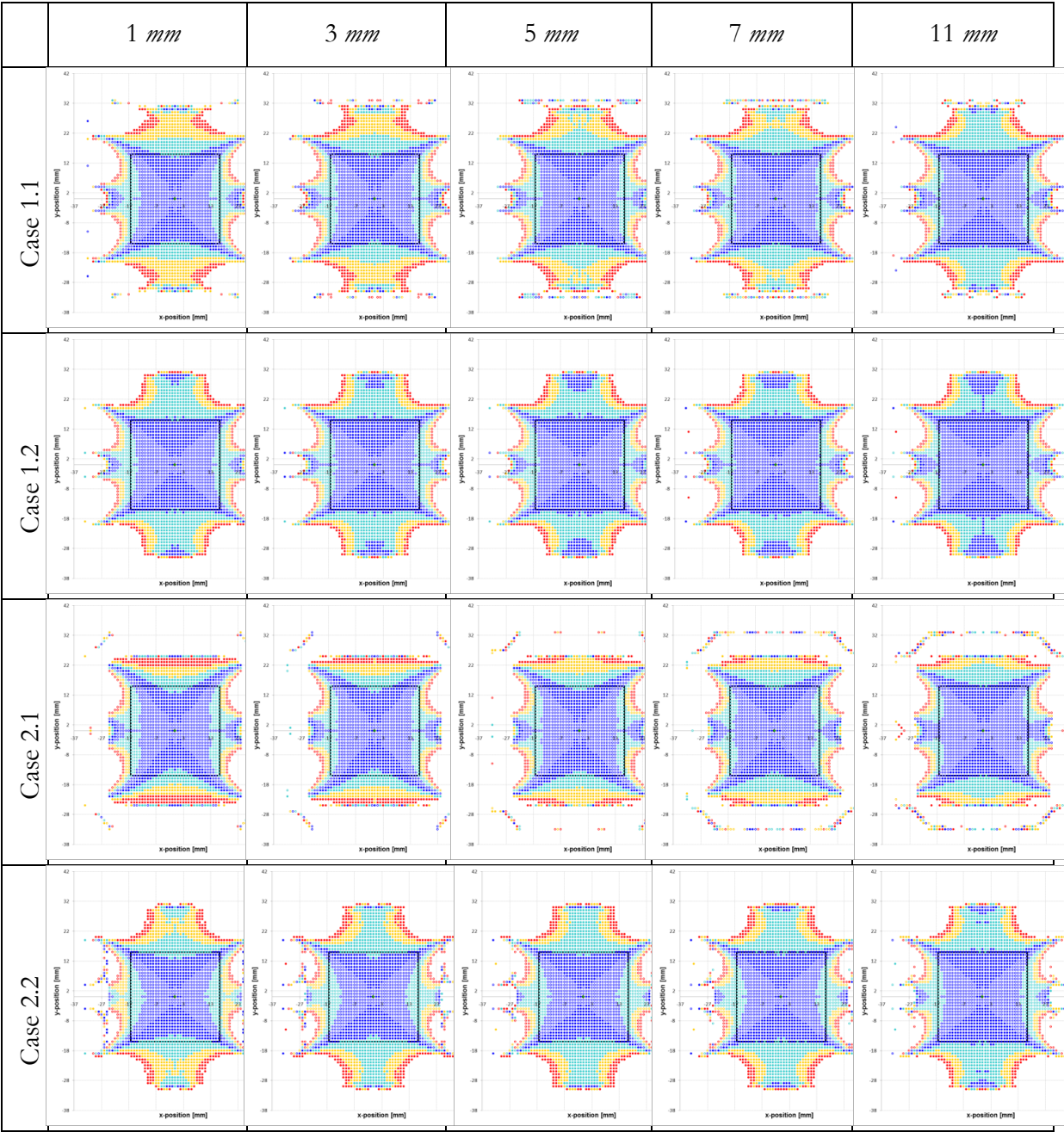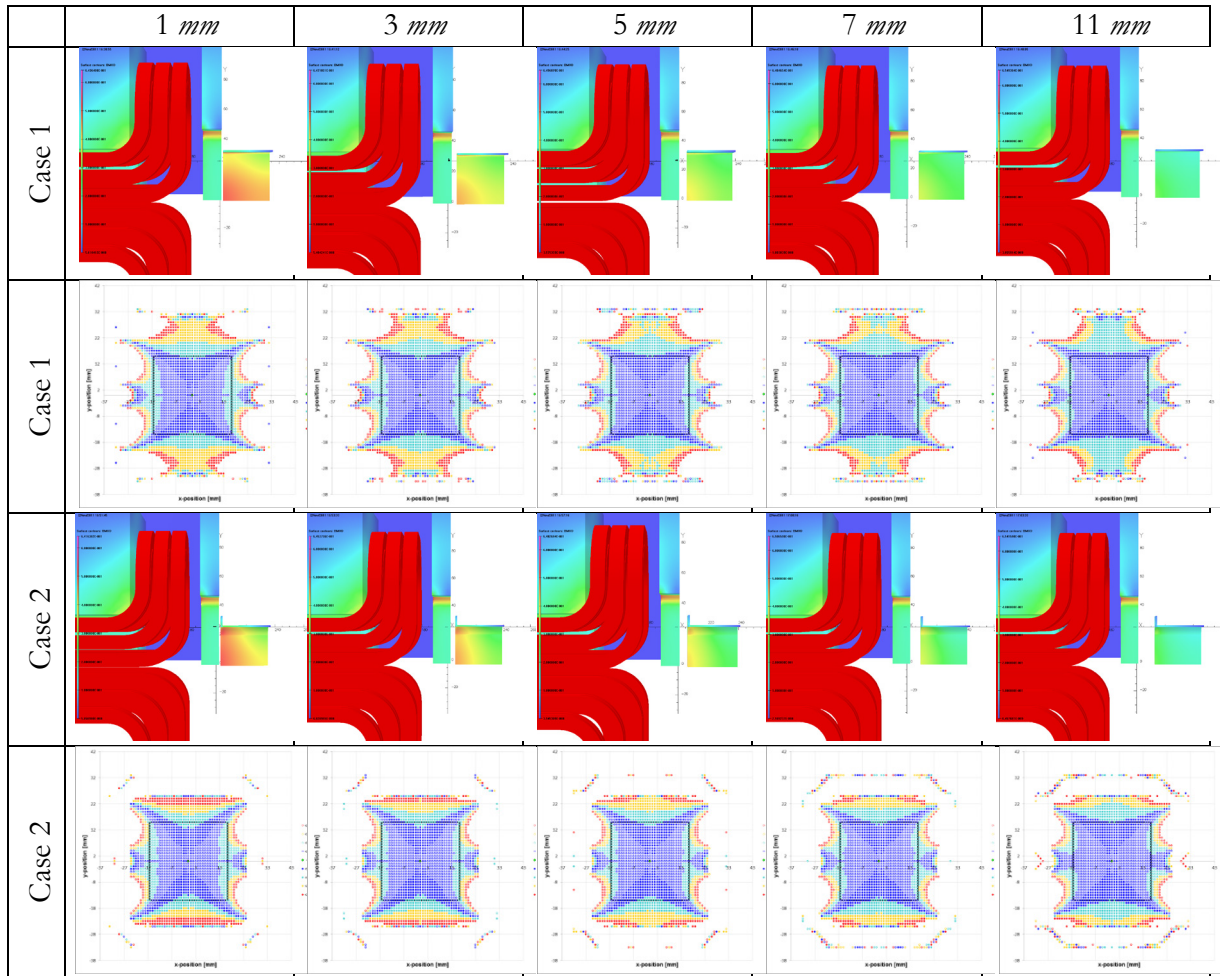Table 3.4. Field homogeneity for different offset distances of the brazing joint

	1 mm	3 mm	5 mm	7 mm	11 mm
Case 1.1					
Case 1.2					
Case 2.1					
Case 2.2					

Table 3.5. Fringe field effect on brazing. Flux density in the braze not exceeding 650 *mT*

	1 *mm*	3 *mm*	5 *mm*	7 *mm*	11 *mm*
Case 1					
Case 1					
Case 2					
Case 2					

3.2.3 Analysis of magnet characteristics for the different offset distances

The effects of the inclusion of the brazed joint into the magnetic circuit can be summarized from Table 3.6 and Table 3.7. The maximum field in the middle of the magnet gap remains unchanged. The fringe fields are not completely neutralized by the laminated steel endplates. The presence of the highly permeable brazing joint (50-50 Fe-Ni) provides a path for the fringe flux lines. The flux density does not go above the saturation point for this type of alloy which guarantees magnetic shielding. The field quality plots for the different offset distances in Table 3.4 and Table 3.5 show that the field quality remains within the specified 0.2 % tolerance, i.e. beam coherence will remain largely unaffected. Figure 3.32 and Figure 3.33 show a plot of the effective length and integrated magnetic field as a function of the brazed joint offset distance. The points in the graphs corresponding to 50 *mm* offset distance represent the values obtained in the simulation without brazed joint.

Table 3.6. Case 1

Case 1	1 *mm*	3 *mm*	5 *mm*	7 *mm*	11 *mm*	30 *mm*	50 *mm*
$\int Bdz$ [Tmm]	44.66	44.69	44.72	44.74	44.77	44.85	44.88
B_0 [T]	0.13651	0.13651	0.13651	0.13651	0.13651	0.13651	0.13647
L_{eff} [mm]	327.17	327.38	327.56	327.69	327.95	328.53	328.88
W [J]	14.34	14.34	14.34	14.34	14.34	14.34	14.33
L [μH]	80.47	80.46	80.46	80.46	80.46	80.45	80.41

Table 3.7. Case 2

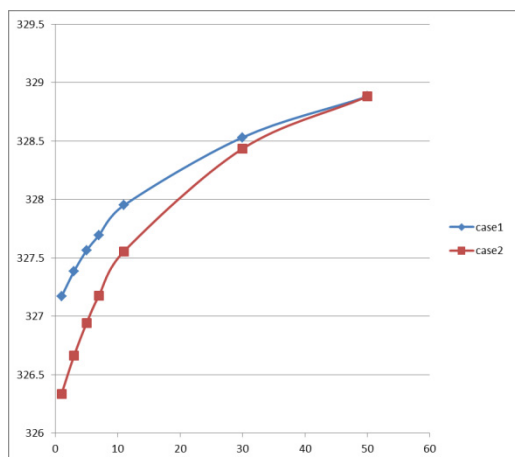| Case 2	1 *mm*	3 *mm*	5 *mm*	7 *mm*	11 *mm*	30 *mm*	50 *mm*
$\int Bdz$ [Tmm]	44.55	44.59	44.63	44.66	44.72	44.84	44.88
B_0 [T]	0.13651	0.13651	0.13651	0.13651	0.13651	0.13651	0.13647
L_{eff} [mm]	326.34	326.66	326.94	327.18	327.56	328.43	328.88
W [J]	14.34	14.34	14.34	14.34	14.34	14.34	14.33
L [μH]	80.48	80.47	80.47	80.46	80.45	80.44	80.41

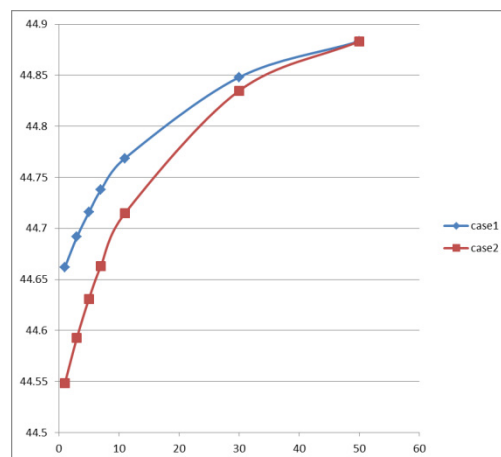Figure 3.32. Effective length vs. offset distance

Figure 3.33. Integrated field vs. offset distance

Decreasing the offset distance from the endplates causes a decrease in integrated field. It is more strongly manifested in the second case, where the deviation between the calculated *Bdl* for the 1 *mm* offset and the value calculated in the absence of a brazed joint is 0.75 %, as compared to 0.50 % in case 1. This and the constant maximum field lead to a proportional decrease in effective length – 0.52 % and 0.78 % respectively for case 1, and case 2. Decreasing the offset distance leads to an increase in inductance, however it is less than 0.1 % for the 1 *mm* offset.

A comparison of the two alternatives and their effect on the nominal integrated field $B_0 dl$ is shown on the following graphs. The graphs zoom on the end fields showing the reduction due to the inclusion of the ferromagnetic joint.
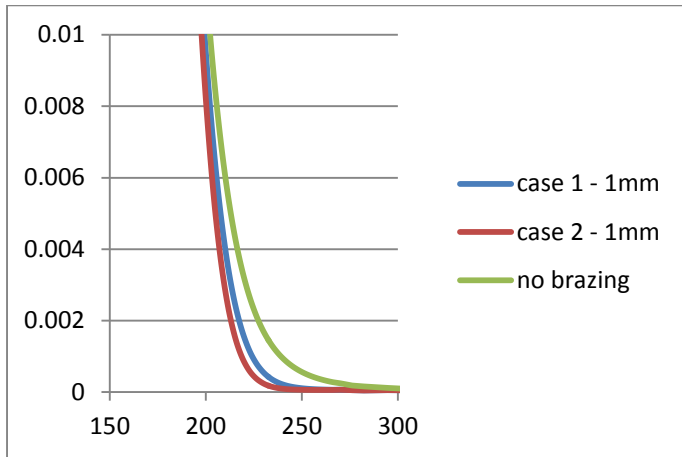
Figure 3.34. 1 *mm* offset from endplates
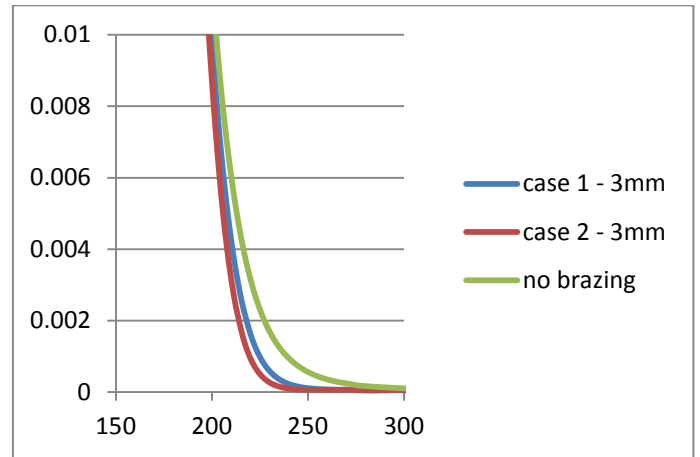
Figure 3.35. 3 *mm* offset from endplates
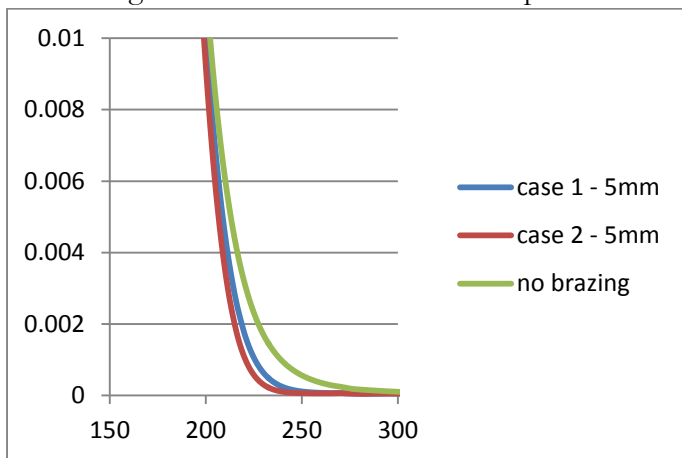
Figure 3.36. 5 *mm* offset from endplates
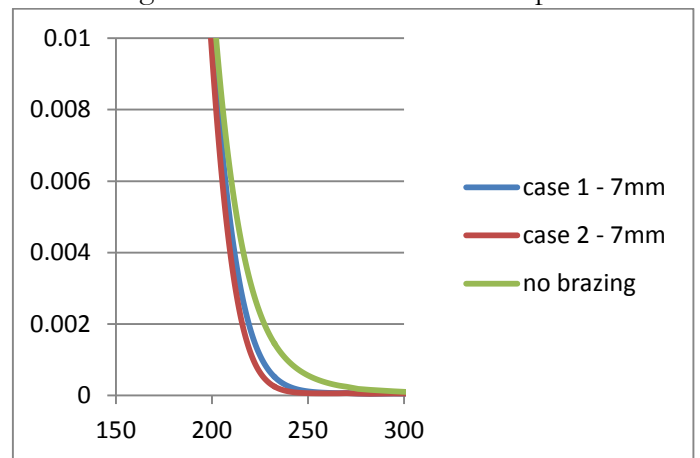
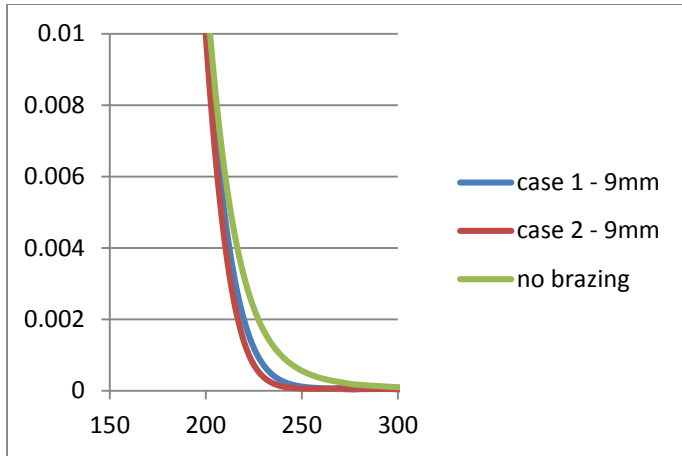Figure 3.37. 7 *mm* offset from endplates
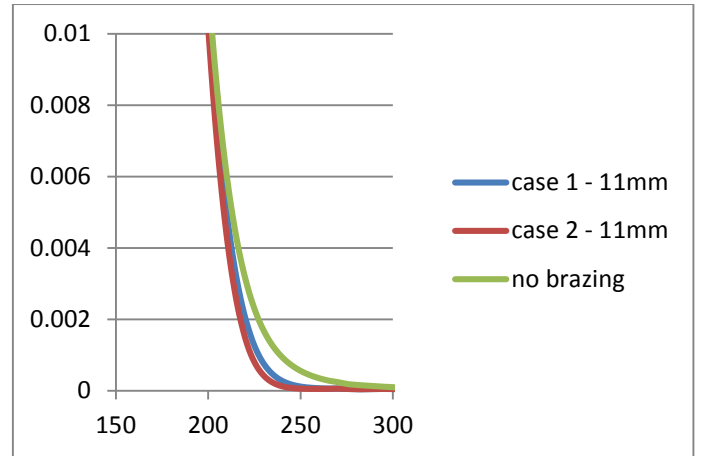
Figure 3.38. 9 *mm* offset from endplates

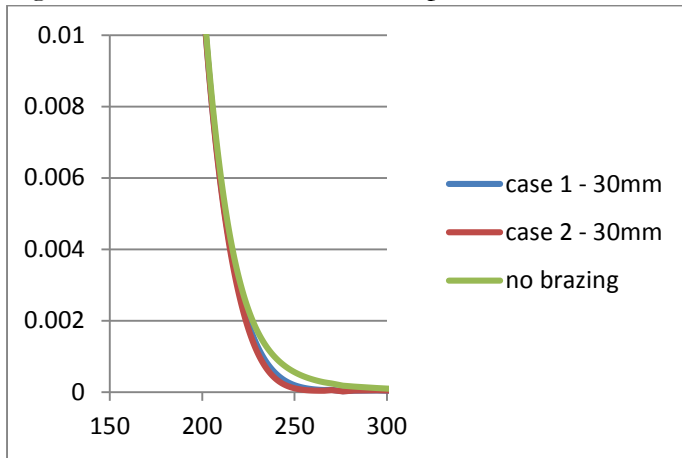Figure 3.39. 11 *mm* offset from endplates
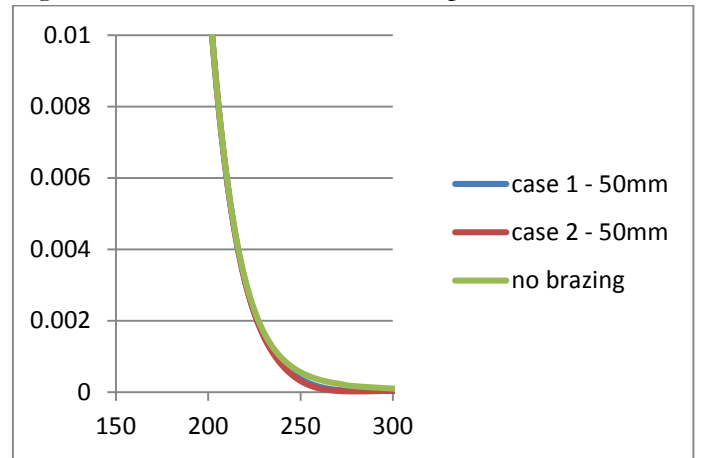

Figure 3.40. 30 *mm* offset from endplates

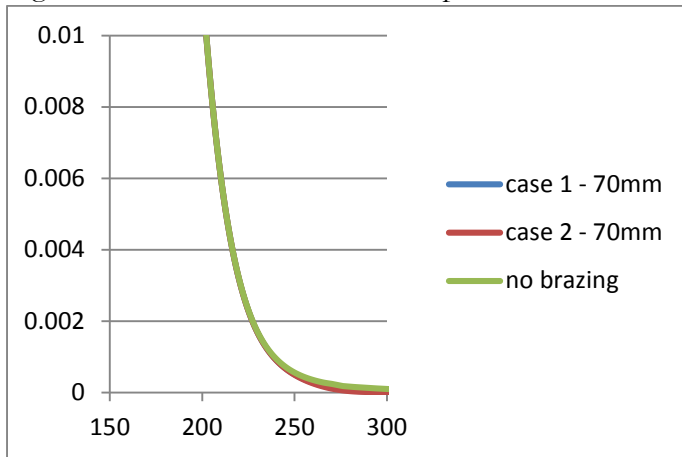Figure 3.41. 50 *mm* offset from endplates
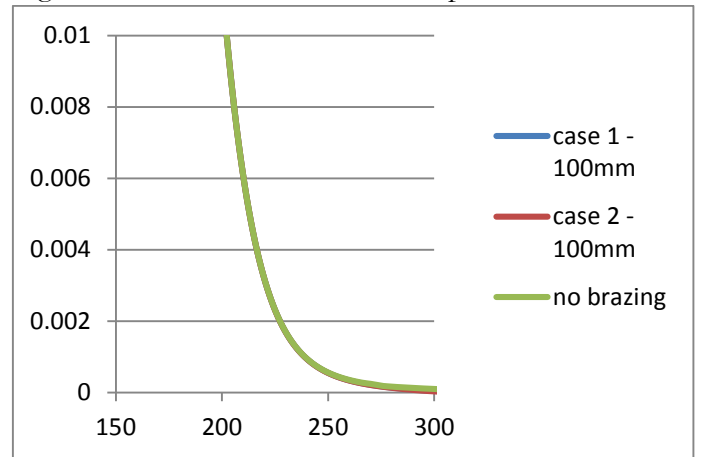

Figure 3.42. 70 *mm* offset from endplates

Figure 3.43. 100 *mm* offset from endplates

Case 2 is more attractive in the way that it requires a shorter ceramic length than case 1 for the same offset from the endplates, whilst maintaining a satisfactory field quality within the chamber. The final geometric configuration of the joint and vacuum chamber is still to be decided, but it needs to take into account the space limitation, behaviour during transients, and possibly the crosstalk between bending magnet and MKC. Depending on the offset distance it is important to include the flange connected to the brazed joint in the simulations, in order to determine how its properties are going to affect the behaviour of the system during transients.

3.2.4   Inclusion of connecting flange into the magnetic circuit

The model used in the previous section has been updated in terms of coil and yoke dimensions in order to improve field uniformity. However the results obtained give a good initial overview of the impact of the vacuum chamber brazing. It has been shown that the proposed vacuum chamber length can be significantly decreased without a major effect on the field quality. The following simulations are an attempt to bring the model one step closer to reality. Case 2 with 1 *mm* offset has been chosen as a starting point. The brazing joint geometry has been updated, and a simplified model of the connecting stainless steel flange has been included according to the preliminary design drawings.

3.2.4.1   *Braze and flange configuration – case 2.1*

An offset distance of 1 *mm* form endplates has been set. This corresponds to a total ceramic length of 404 *mm*. The configuration is shown on Figure 3.44. The brazed joint (purple) follows the profile of the vacuum chamber (grey). The flange and bellows (dark green) have been assigned with a linear isotropic relative permeability of 0.005.
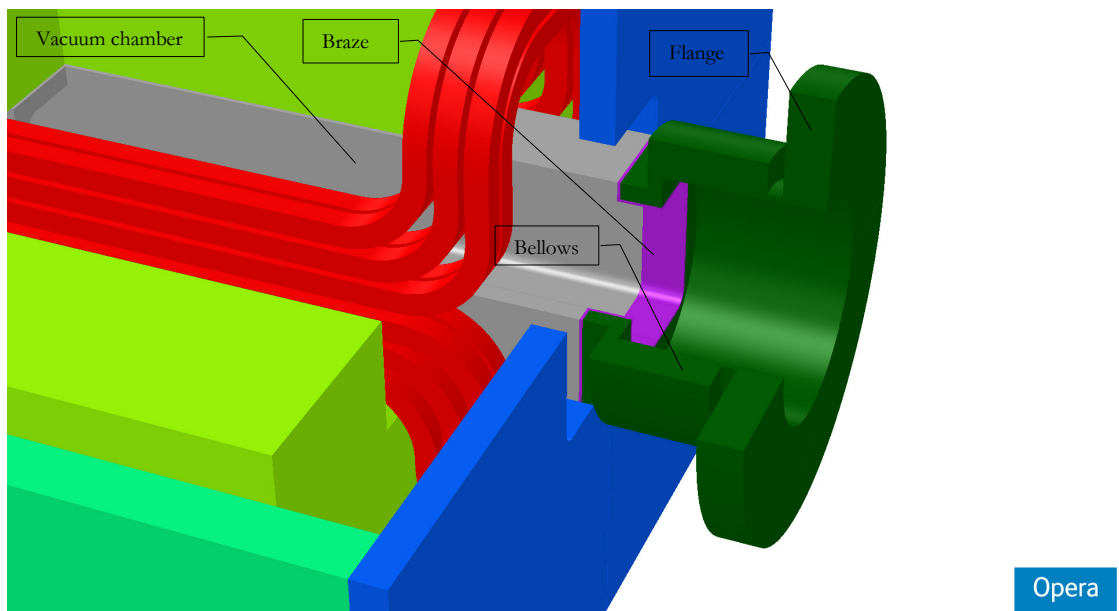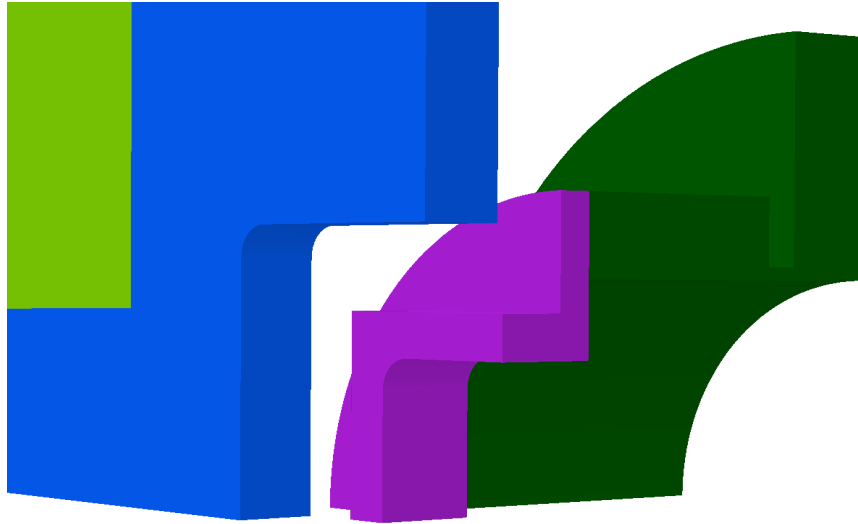

Figure 3.44. Case 2.1 detail

3.2.4.2   *Braze and flange configuration – case 2.2*

For the second simulation the bellow end adjacent to the braze has been given the same nonlinear magnetic properties. Figure 3.45 shows the configuration.

Figure 3.45. Case 2.2

A summary of the results can be seen in Table 3.8

Table 3.8. Transient approximation

	Initial configuration	Case 2.1	Case2.2
$\int Bdz\ [Tmm]$	44.918551	44.53905	44.529682
$B_0\ [T]$	0.136476	0.136486	0.136486
$L_{eff}\ [mm]$	329.131503	326.32688	326.282145
$W\ [J]$	15.048642	15.07676	15.084819
$L\ [\mu H]$	84.45	84.60	84.65

The effective magnetic length relative to the initial configuration is decreased by 0.86 % in case 2.1, and 0.87 % in case 2.2.

3.2.5 Effects of the braze on the end fields

As was seen on the graphs in 3.2.3 the effective length is reduced due to the shielding effect of the magnetic joint between flange and chamber. The following figures show a comparison of the 50-1 *mT* shell surrounding the magnet in the case with and without the inclusion of magnetic

piece. It can be seen that the extension of the fringe fields is reduced which explains the reduction in effective length.
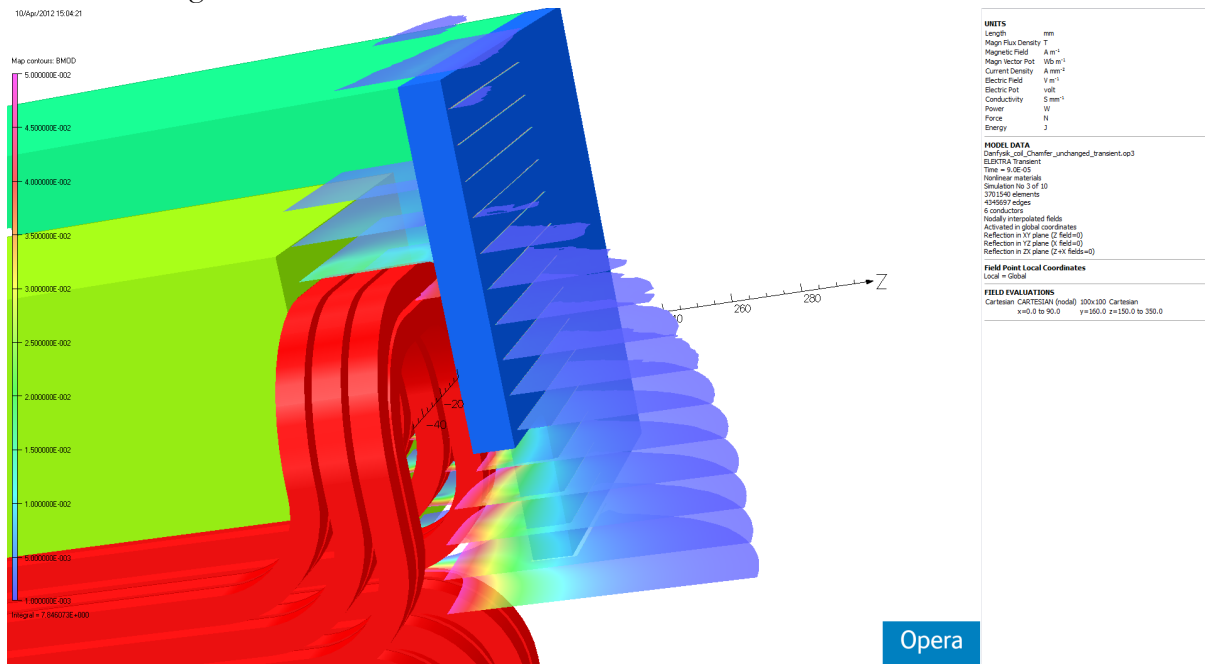

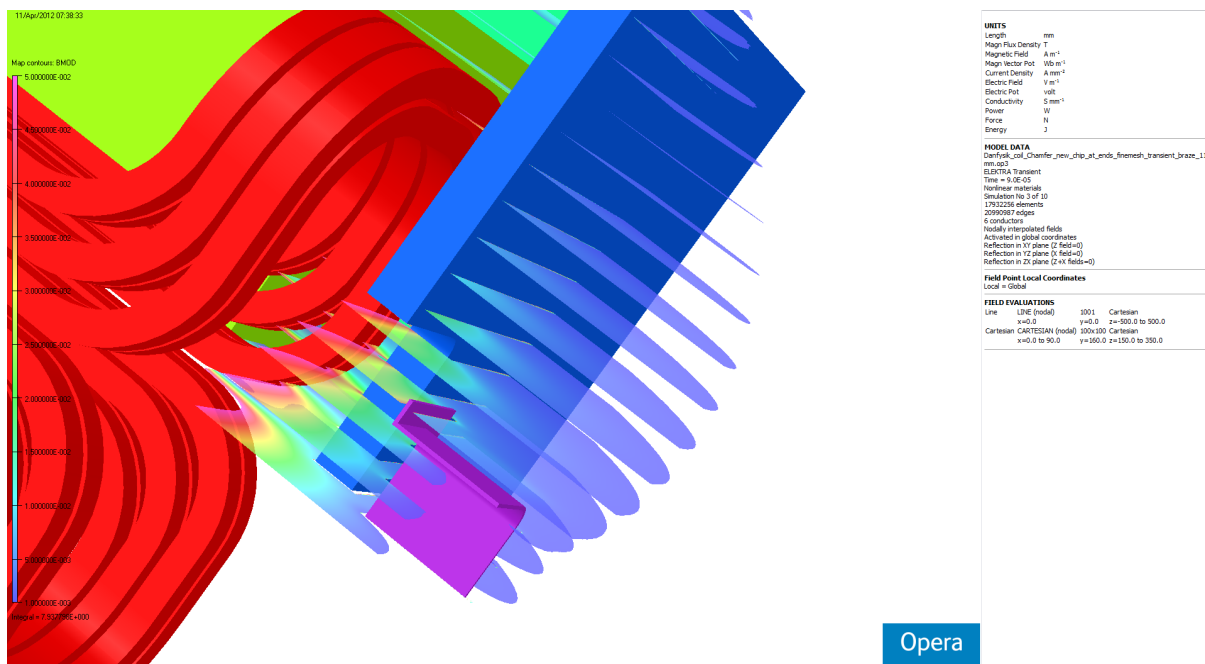Figure 3.46. Model without braze. Range of end fields 50-1 *mT*

Figure 3.47. Model with braze offset at 11 *mm*. Range of end fields 50-1 *mT*

3.2.6 Conclusions on brazing of the vacuum chamber

The magnetic braze has a non-negligible effect on the effective magnetic length. By shielding parts of the fringe fields it can reduce it by up to 0.7 % for the closest offset distances. Since this is considered to be within the margins of the system it was decided that the brazing technique as well as the braze location will not affect the system performance. Therefore the scheme of brazing

the flange will be chosen purely based on mechanical and vacuum considerations by the vacuum chamber supplier and will not be imposed by MedAustron. The results of this study have been presented in [21].

Subsequently case 2 has been chosen by the manufacturer NTG GmbH. The total chamber length flange to flange is 478 *mm*. The ceramic length is 448 *mm*, which corresponds to an offset of the braze from the endplates of 23 *mm*. It has been decided that the magnet should not be opened to insert the complete chamber, as there is the risk of damaging the ferrites. Thus the chamber will be delivered with one flange brazed at the manufacturer's premises. At MedAustron the chamber will be inserted into the magnet, and the second flange will be brazed on-site. Figure 3.48 shows the vacuum chamber being brazed at MedAustron.

Figure 3.48. Installation of vacuum chamber February 2014

3.3 Coil design

The MKC uses a water cooled coil wound from a hollow square conductor of 8×8 *mm* with a cooling water hole of 4 *mm* diameter and end parts bent into a saddle shape. The coil is a two layer (inner and outer) configuration with 3 turns per layer. During the review of the Preliminary Design Report (PDR) provided by Danfysik – the company to whom final mechanical design and manufacturing of the magnet was subcontracted, an inconsistency was discovered between the coil design requested by MedAustron (the one used for the preliminary FEM simulations), and the proposal by Danfysik. The shaping of the conductor in the region of the coil heads had not taken into account the minimum permissible bending radius accepted by Danfysik, which as a general rule cannot be less than three times the thickness of the conductor. Also the mechanical design shows a coil with progressively increasing bending radii of 16, 26 and 36 *mm*. Implementing a sharper bending radius would result in unacceptable deformations due to the keystoning effect, which would distort the geometry of the coil, and would furthermore flatten the cooling water hole, thus reducing the water flow.

A simulation of the magnet with the proposed coil layout was executed which showed a substantial deterioration of the integrated field quality. The task was then to study several possibilities for a new geometry of the coil end parts, and to define a final coil design. The main restriction was to maintain the minimum bending radius, and to achieve the desired field quality in the magnet gap [22].

3.3.1 Initial coil design

The initial Opera 3d simulations that were used to derive the required magnet performance parameters used in the technical specification [12] used a coil design based mainly on theoretical assumptions. These had not taken into account the keystoning effect, and the minimum bending radius that was required. Furthermore, an error had occurred during the migration of the Opera electromagnetic model into the Autodesk Inventor® 3d mechanical design. Figure 3.49 shows the mechanical model as drawn in Autodesk Inventor®. The innermost turn has a bending radius of 16 mm, which is only twice the conductor thickness.

Moreover it was discovered that the coil connectors require two additional chamfers in the ferrite in order to fit into the magnet frame. Due to the brittleness of the ferrite these potentially weak spots must be eliminated in the final design Figure 3.51.
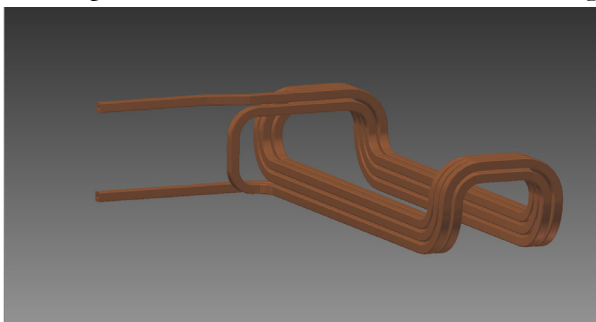

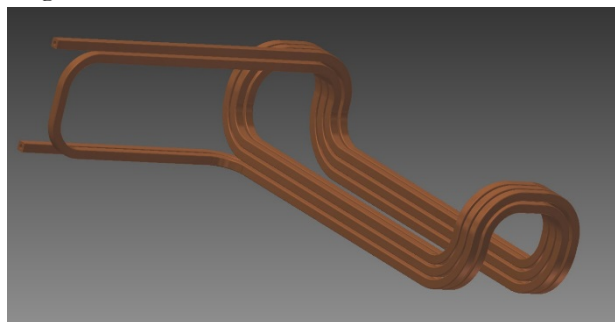Figure 3.49. MKC coil as drawn in the MedAustron preliminary design mechanical model

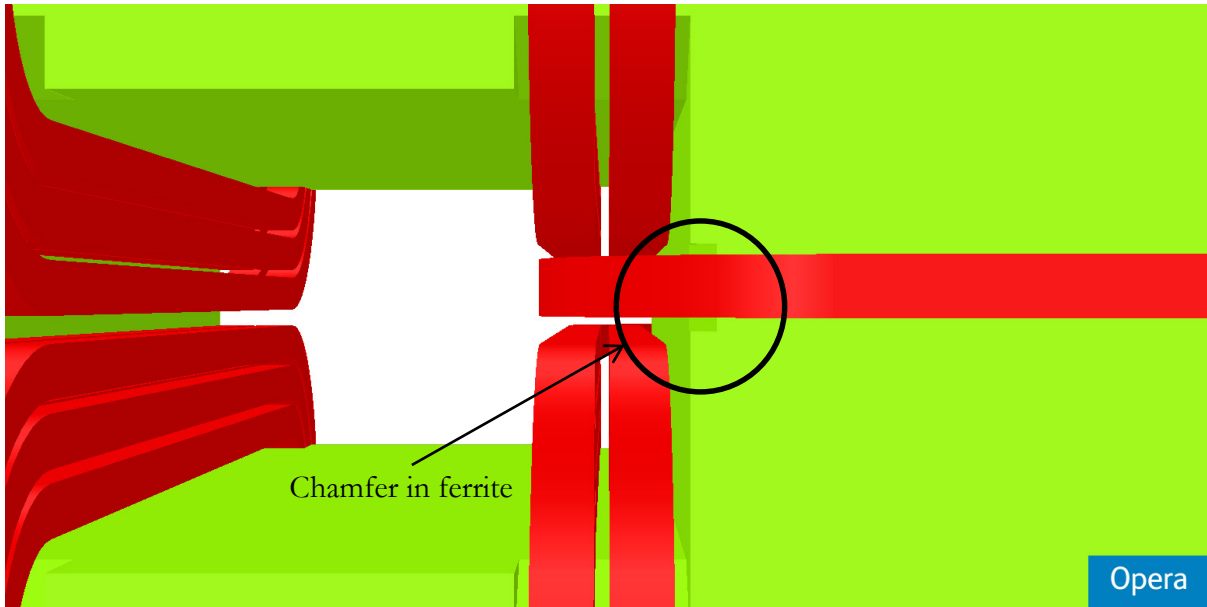Figure 3.50. Coil design as proposed by Danfysik

Figure 3.51. Chamfer in side ferrite

Figure 3.52 shows the MedAustron model in Opera. It can be seen that the coil used in the electromagnetic design has equal bending radii on all three turns in both layers of the coil heads. The Autodesk Inventor® models on Figure 3.49 and Figure 3.50 show a coil which is wound as a three turn racetrack where each successive turn going outwards is 20 *mm* longer longitudinally (10 *mm* on either side of the magnet centre). The three turns are then all bent in one operation, which results in equal height of the thus formed coil heads. In the resulting coil, the bending radius of each successive turn follows the shape of the previous one, therefore r 16 *mm* of the innermost turn, r 26 *mm* for the intermediate turn, and r 36 *mm* for the outermost turn (corresponding to a conductor thickness of 8 *mm* plus 2 *mm* of insulation between conductors). Whereas this approach is very easy to produce mechanically, it does not satisfy the field quality criteria due to the shorter straight sections of the coil [23].
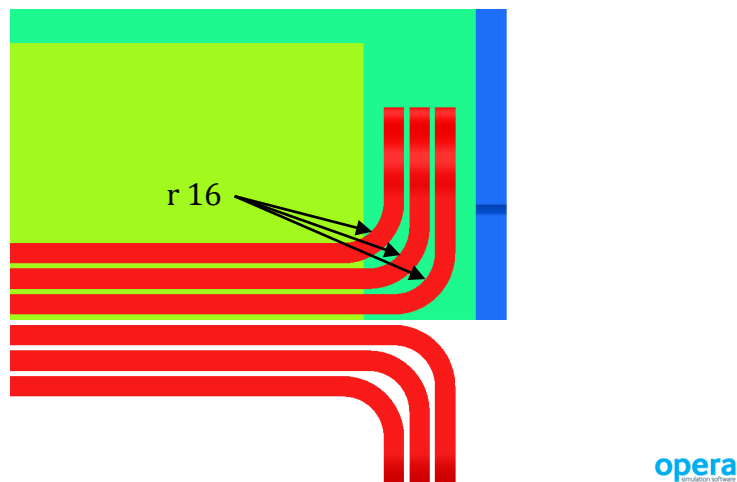

Figure 3.52. Initial model in Opera

The solution needs to respect the minimum bending radius of three times the conductor width of 24 *mm*, allow for accommodating a potentially larger coil into the magnet without increasing its overall dimensions, and would have to maintain the required homogeneity in the good field region.

3.3.2   Coil design proposed by Danfysik

Figure 3.50 shows the coil design proposed by Danfysik in the Preliminary Design Report [24]. The bending radii for the coil heads are kept at respectively 24, 34, and 44 *mm* for the consecutive turns. This design had to be verified in terms of field homogeneity before a formal approval could be sent for the coil manufacturing. Several options with the Danfysik layout will be examined in an attempt to verify the coil design with progressively increasing bending radii.

The Danfysik proposal requires the coil straight sections to be reduced, as compared to the MedAustron preliminary design, in order to fit the larger bending radius within the same overall length. The height of the coil heads is also increased by 20 *mm*. Figure 3.53 and Figure 3.54 show the model and the corresponding field homogeneity plot. It clearly does not satisfy the stringent field quality criterion of ± 0.2 %.

It will be shown that the length of the straight sections must be increased if the field quality is to be preserved. For this the overall magnet dimensions will not be changed, which will impact the clearance between the coil and laminated endplate. The results of the simulations are listed on the following pages.
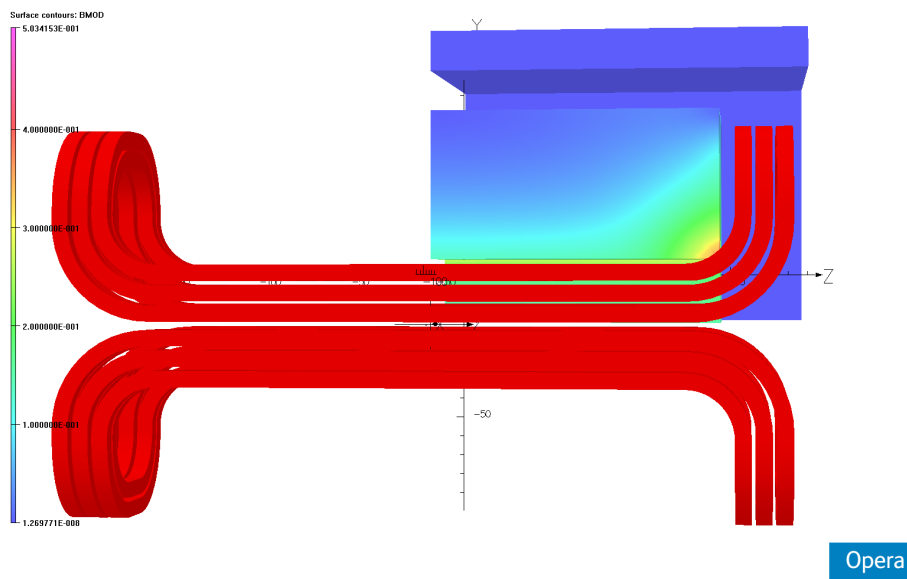

Figure 3.53. Model of the Danfysik coil. Outer bending radii follow shape of inner. r_{inner} = 24 *mm*, r_{mid} = 34 *mm*, r_{outer} = 44 *mm*
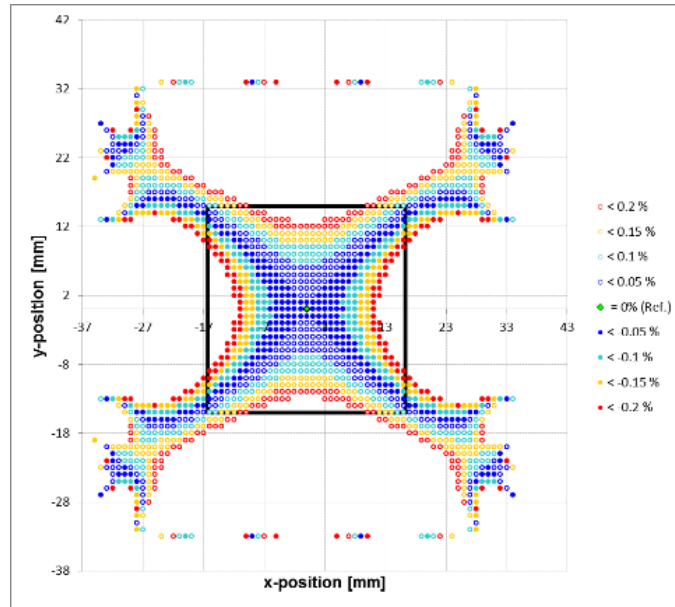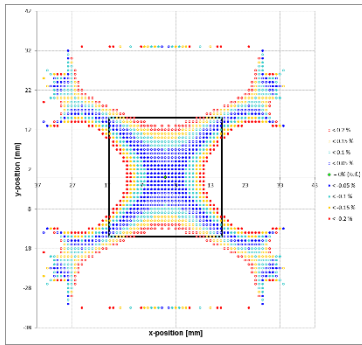
Figure 3.54. Danfysik proposal homogeneity plot.

Figure 3.55. r_{inner} = 24 mm, r_{mid} = 34 mm, r_{outer} = 44 mm

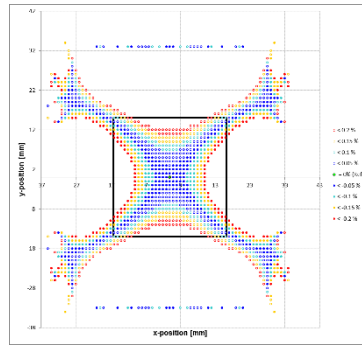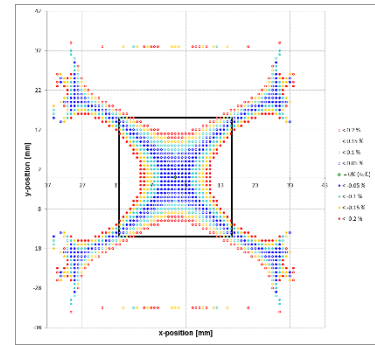Figure 3.56. r_{inner} = 26 mm, r_{mid} = 36 mm, r_{outer} = 46 mm

Figure 3.57. r_{inner} = 28 mm, r_{mid} = 38 mm, r_{outer} = 48 mm

3.3.3 Coil design proposed by MedAustron

The proposal for the coil design was rejected since it does not provide the desired field quality. The coil was redesigned with the specified minimum bending radius for all turns and layers. The redesigned coil and corresponding field homogeneity plot are shown on Figure 3.58.
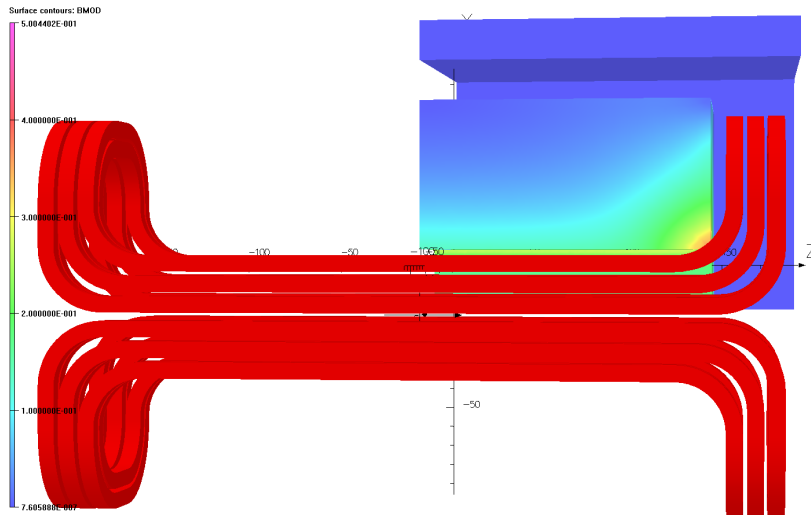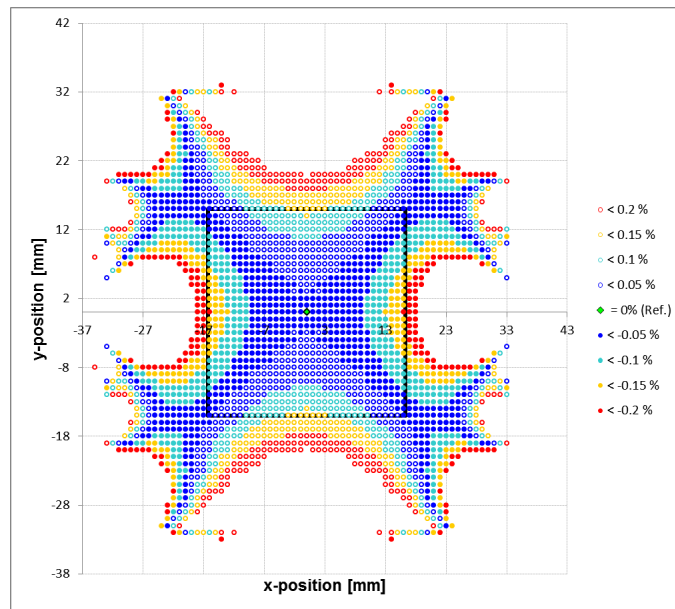
Figure 3.58. Proposal for coil design with corresponding homogeneity plot. Outer bending radii are kept the same as inner. r_{inner} = 24 *mm*, r_{mid} = 24 *mm*, r_{outer} = 24 *mm*

This configuration of the conductors satisfies the homogeneity condition as well as the manufacturing criteria imposed by the supplier and therefore this modification was accepted by both parties.

3.3.4   Coil design retained for the definitive design. Conclusions

At this stage the coil geometry needs to be modelled in Opera in a realistic manner. It includes the turns as they should be wound, as well as the end connectors. The coil is built turn by turn with simple arcs and bricks following the template on Figure 3.58. The following renderings show the newly designed coil with the modified coil heads highlighted in orange.
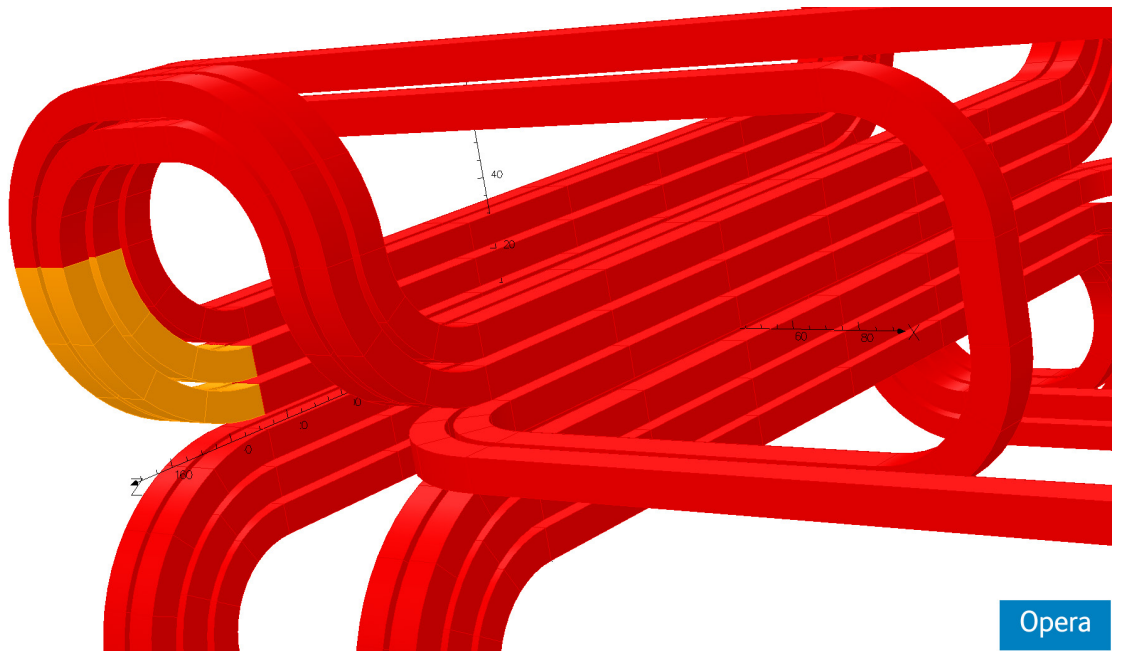
Figure 3.59. Coil as per Danfysik drawing
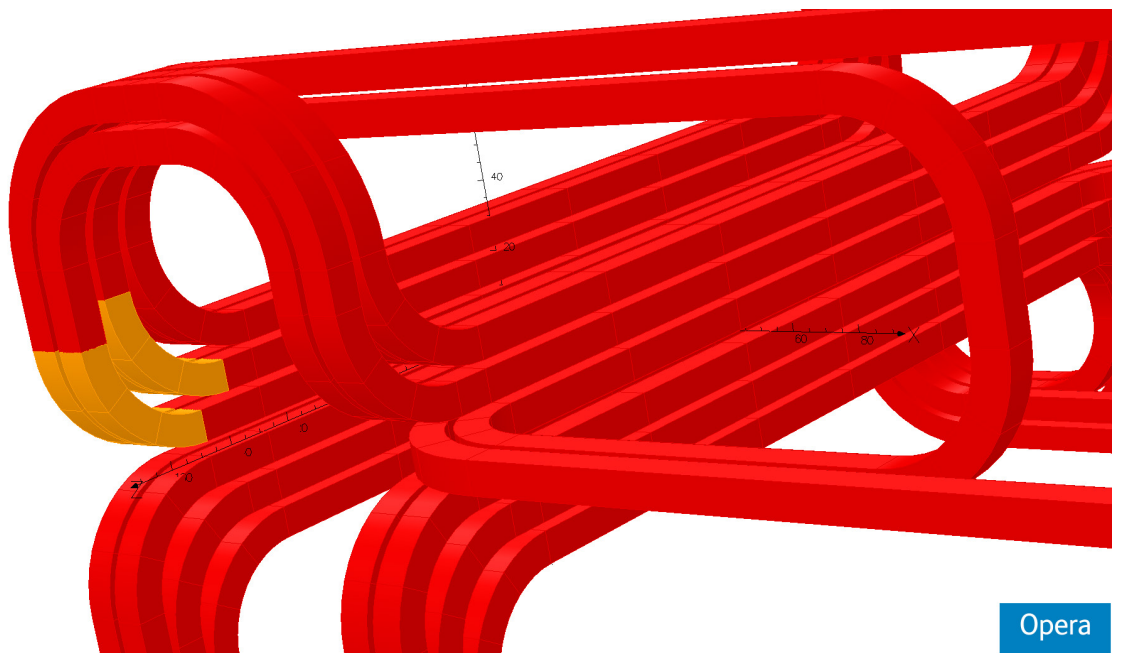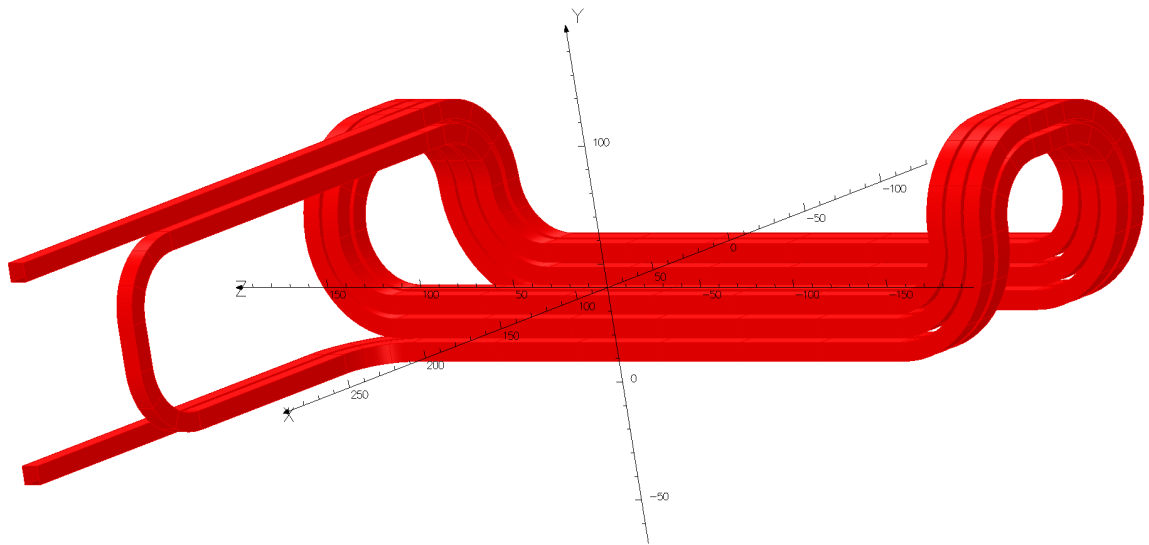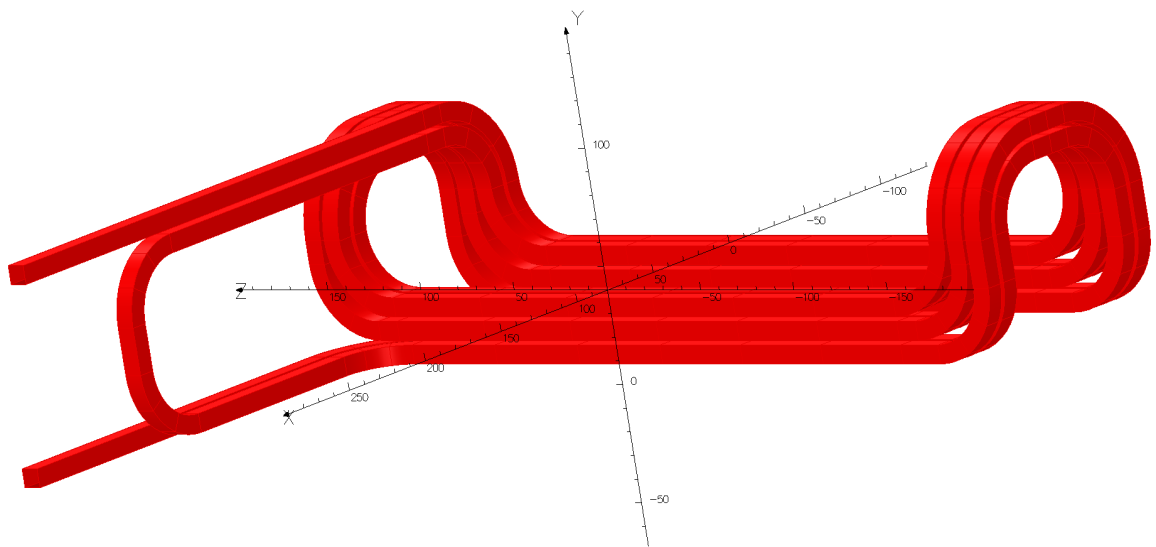

Figure 3.60. Newly designed coil with modified end parts

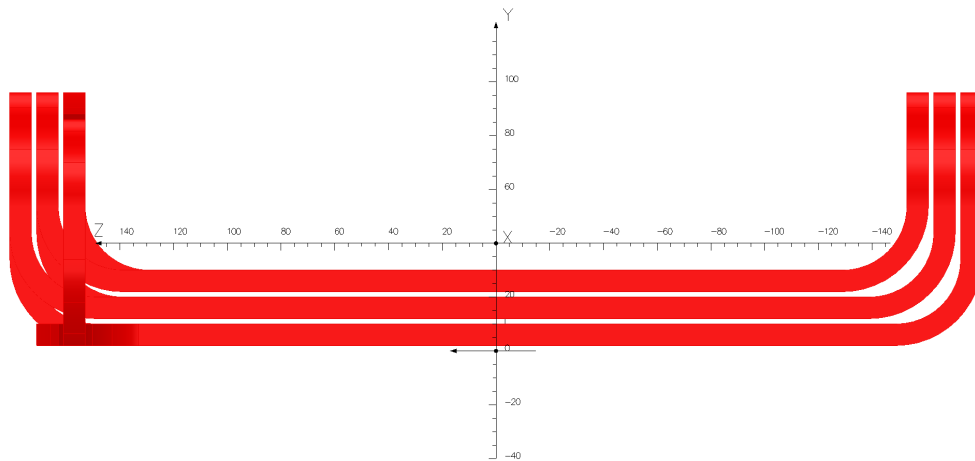Figure 3.61. Overall view of the coil proposed by Danfysik

Figure 3.62. Overall view of the new coil design

The coil overall dimensions have been preserved with respect to the original design so that it fits inside the magnet frame with the required clearances. Comparison views are shown on Figure 3.63 and Figure 3.64.
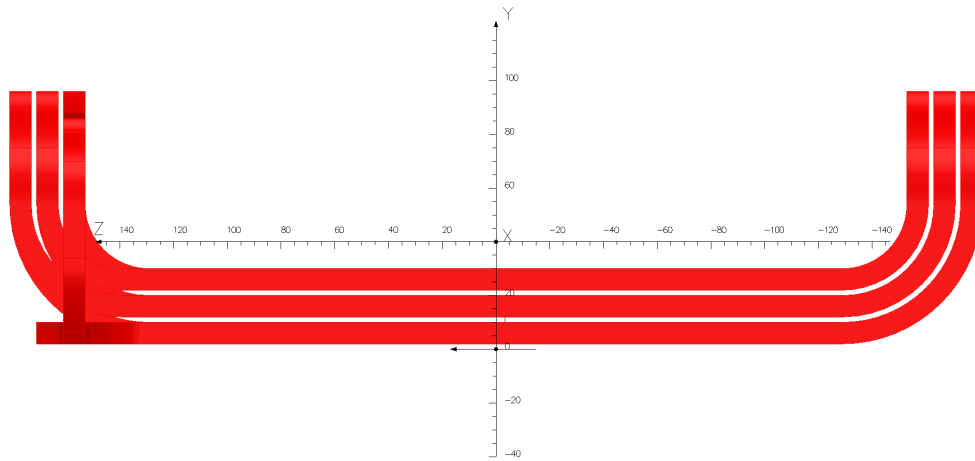
Figure 3.63. Danfysik coil side view

Figure 3.64. MedAustron coil side view

The coil design from Opera has been extracted into an Autodesk Inventor ® 3d model. Subsequently this was used to create the drawings that were approved for the definitive design. The proposed coil geometry as extracted from the 3d FEM simulation is shown on Figure 3.65. Here the link between the inner and outer layer is made with a copper plate brazed to the conductors. This allows the inner and outer layers to be cooled in parallel, rather than in series as designed.

Figure 3.66 and Figure 3.67 show the finished coils before and after impregnation. The inter-turn insulation and the gaps between bends are filled with machined G-Etronax EP11 glass-fibre epoxy to avoid resin rich areas (prone to cracking). The coil is wrapped in glass fibre tape, and impregnated in a precision mould under vacuum using CTD-101K epoxy resin.
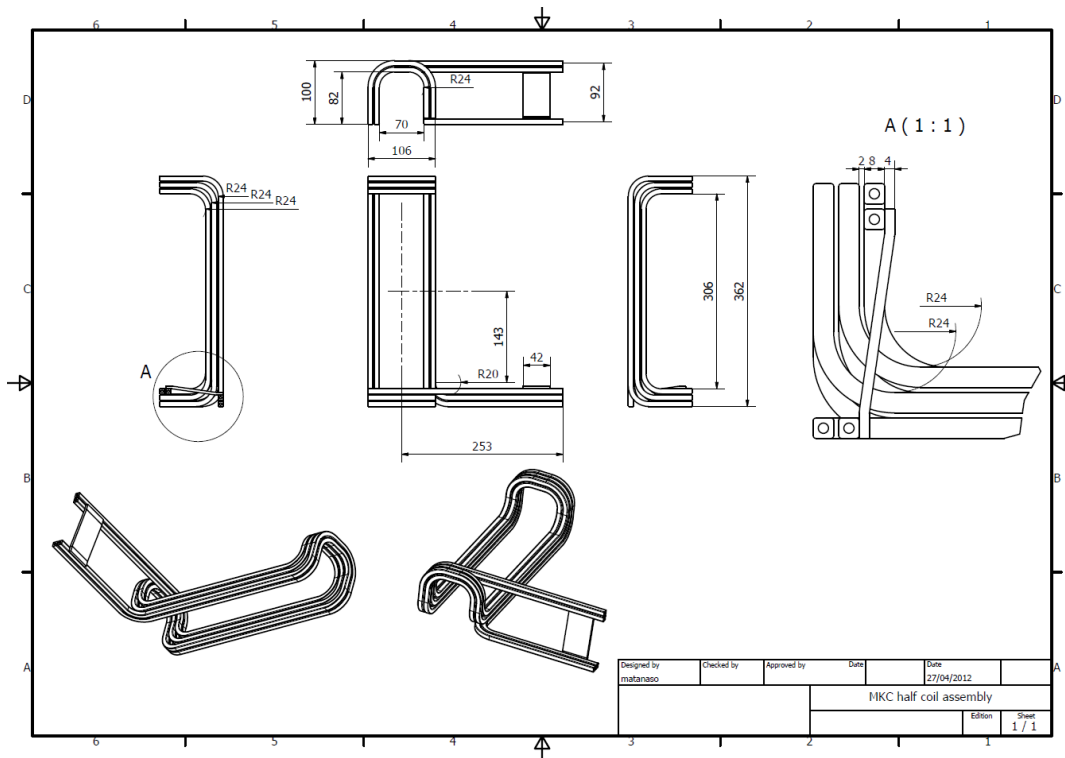
Figure 3.65. MKC half coil assembly

Figure 3.66. MKC coil before impregnation

Figure 3.67. MKC coils after impregnation

65

3.4 Shape of the ferrite yoke

As mentioned earlier the MKC uses a window frame ferrite yoke with dimensions 258 × 216 × 290 *mm* and an aperture of 66 × 66 *mm*. Due to the brittleness and low machinability of the ferrite the yoke is assembled out of several blocks including: top and bottom parts each consisting of three individually glued blocks, and two side blocks sandwiched between the top and bottom sections (Figure 1.7). The top and bottom ferrites are glued from three parts since the manufacturer cannot press a single volume with these dimensions. The layer of glue is tangential to the magnetic flux lines. The yoke is held in place between the aluminium housing and the coil by layers of insulation spacers. The side ferrites are not glued to the top and bottom ones since the glue layer will be normal to the flux lines. The top part of the magnet including the coil and top ferrite can be lifted in order to fit the ceramic vacuum chamber in the gap in case both flanges have been brazed to it. Although the magnet does not have to be opened for the installation of the vacuum chamber, it must nevertheless be easy to dismantle for maintenance.

In this section the effects of ferrite surface imperfections will be studied, and final shape of the ferrite yoke will be defined [25].

3.4.1 Definition of surface chips

Ceramic Magnetics, Inc. work instruction 41-860-01 specifies the size and number of imperfections for ferrite surfaces. The chips are divided into 3 classes depending on their size (surface area and penetration into surface) relative to the surface area of the ferrite blocks. Unlike for CERN applications, where Class A ferrites are used, MedAustron found itself contractually bound to accept class B ferrites. The chip size for the MKC ferrites will fall into class B which is divided into two sub-classes.

- Class *B1* defines critical or mating surface chip size. For a surface area bigger than 161 cm^2, the maximum permissible penetration in surface is 3.048 *mm*, with maximum chip surface area of 0.4 cm^2 – not more than 0.25 % of the total surface area.
- Class *B2* defines the chip size for non-critical surfaces. For a surface area bigger than 161 cm^2, the maximum permissible penetration in surface is 6.096 *mm*, with maximum chip surface area of 1.61 cm^2 – not more than 1 % of the total surface area.

3.4.2 Worst case simulations

Several simulations have been carried out removing bits of ferrite in critical in terms of field quality spots. Figure 3.68 shows the model with the newly defined coil used for reference.

Figure 3.69 presents a worst case simulation with a 6 × 3 *mm* channel cut out of the middle of the pole face. The pole face is assembled from three ferrite blocks, with the biggest having a surface area of 258 cm^2. Thus the 6 *mm* wide channel takes up 2.3 % of the total surface area of the block. The field quality is just inside the 0.2 % margin.

In Figure 3.70 the chamfer used to sit the coil is essentially extended across the width of the pole gap. As can be seen from comparing Figure 3.68 and Figure 3.70, the missing part is strongly saturated in the original model. The maximum flux density in the ferrite is reduced by 43 %. The field quality plot shows a ± 0.05 % maximum inhomogeneity inside the entire good field region. This is a major improvement and was chosen as the final shape of the pole edge.

Figure 3.71 shows a 3 × 6 *mm* channel in the side ferrite. This area is the least affected, and as can be seen from the plot, the impact on field quality is insignificant.
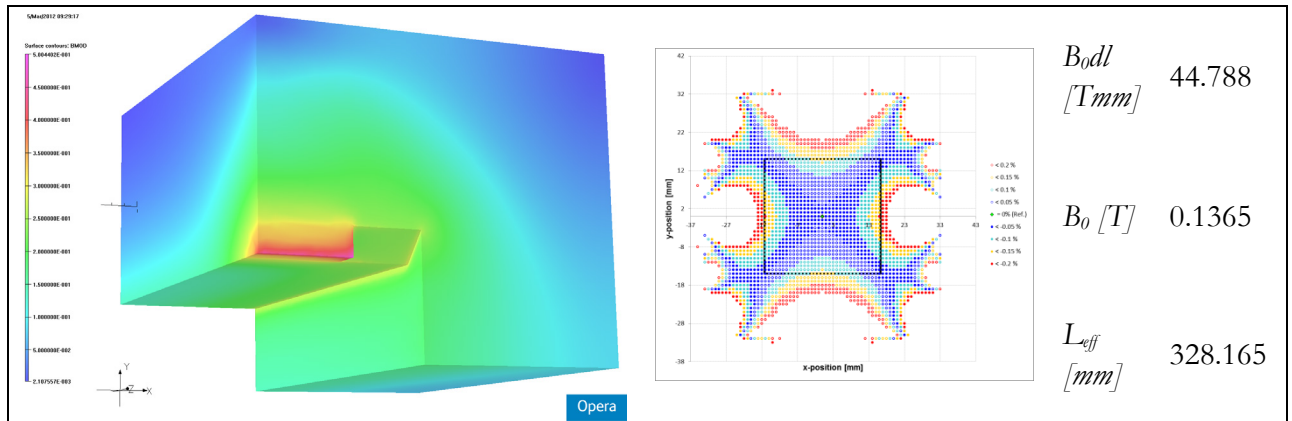
Figure 3.68. No chips in surface, B_{max} = 500 *mT*

B_0dl [*Tmm*]	44.788
B_0 [*T*]	0.1365
L_{eff} [*mm*]	328.165
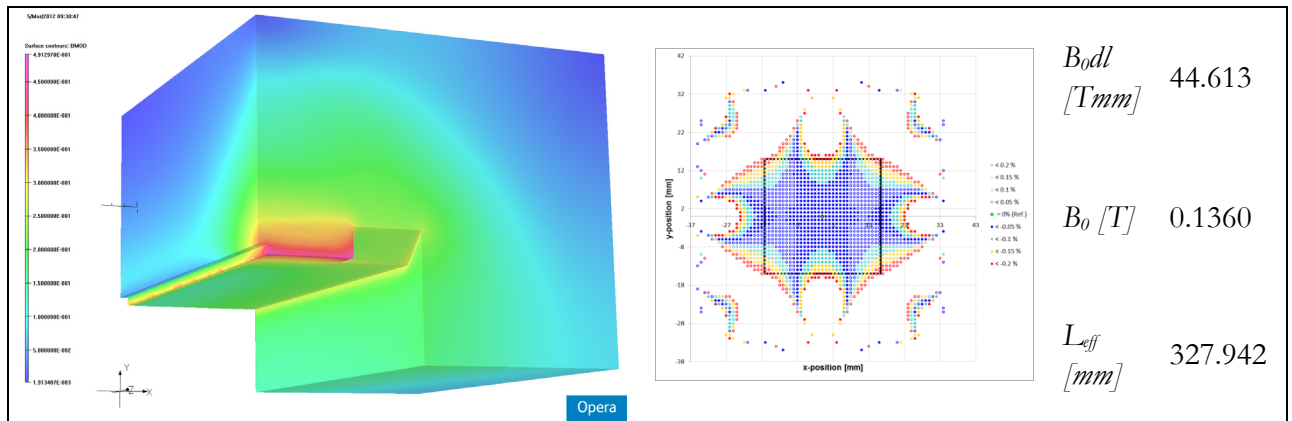
Figure 3.69. Worst case – 6 × 3 *mm* chip along the length of the top ferrite, B_{max} = 491 *mT*

B_0dl [*Tmm*]	44.613
B_0 [*T*]	0.1360
L_{eff} [*mm*]	327.942
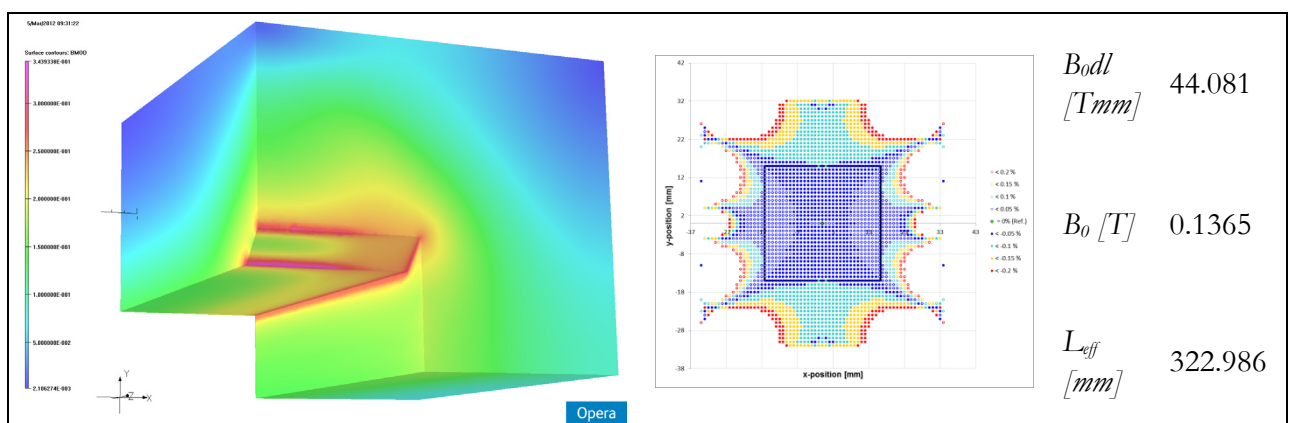
Figure 3.70. Chamfer along the edge of the pole, B_{max} = 344 *mT*

B_0dl [*Tmm*]	44.081
B_0 [*T*]	0.1365
L_{eff} [*mm*]	322.986
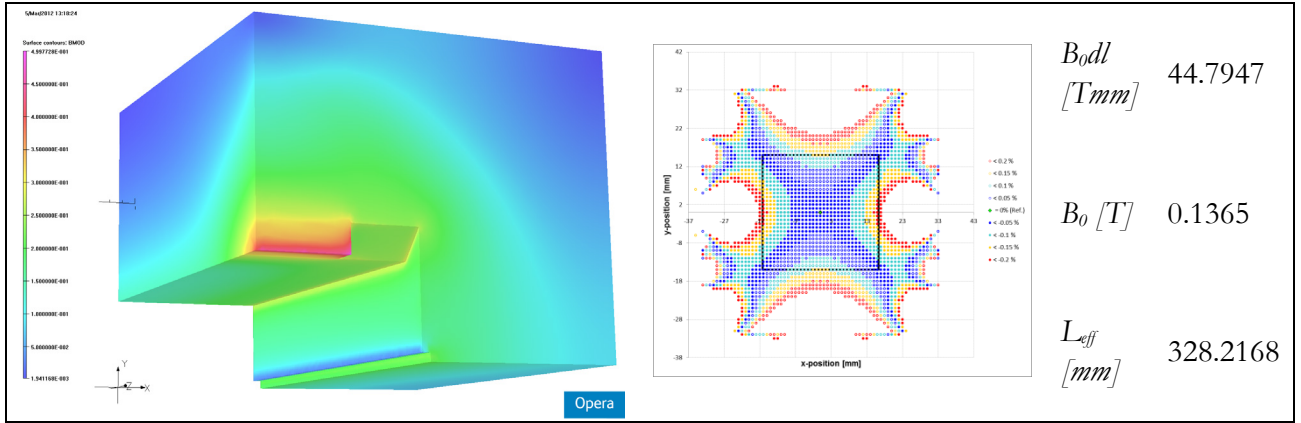
Figure 3.71. 3 × 6 *mm* chip along the length of side ferrite, B_{max} = 500 *mT*

A comparison between the two options is shown on Figure 3.72 and Figure 3.73. The small reduction in effective length brings this design closer to the specified in Table 1.2. The homogeneity in the good field region is vastly improved. A scaling factor has been applied to the current drive to ramp the excitation current to 700 *A*. The plot is shown on Figure 3.74

Figure 3.72. Preliminary design, *I*=597 *A*, B_{max} = 500 *mT*

Figure 3.73. Chamfered pole edge, *I*=597 *A*, B_{max}=344 *mT*

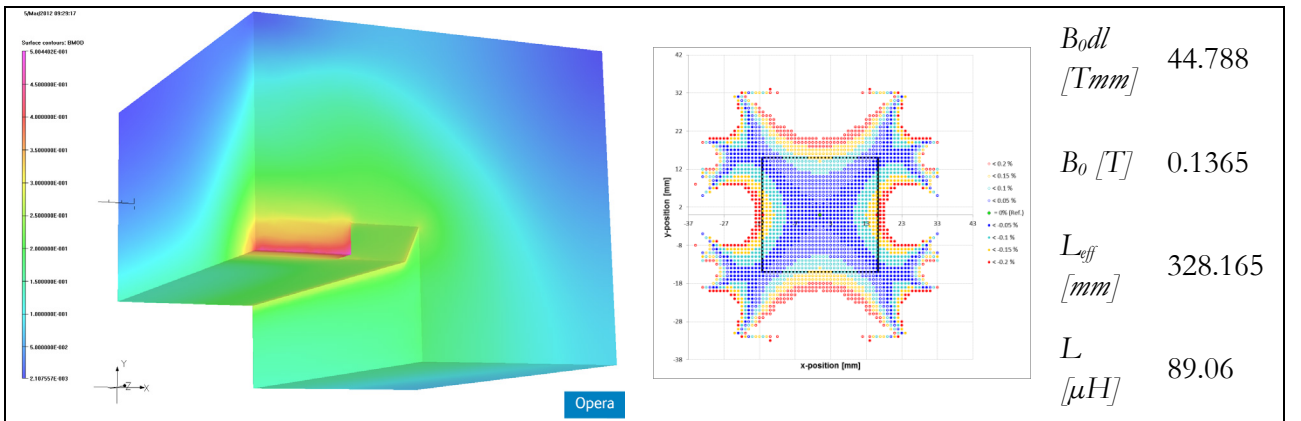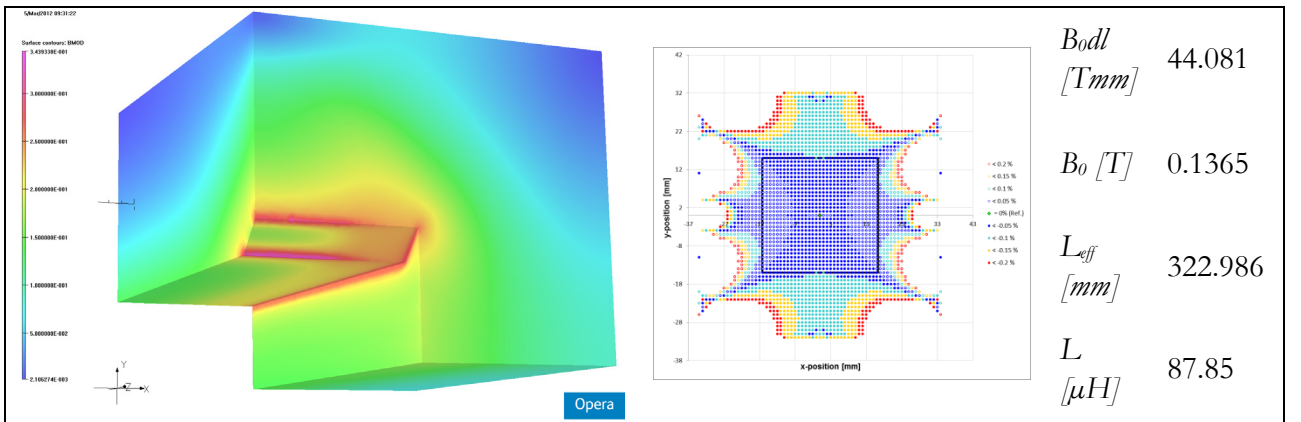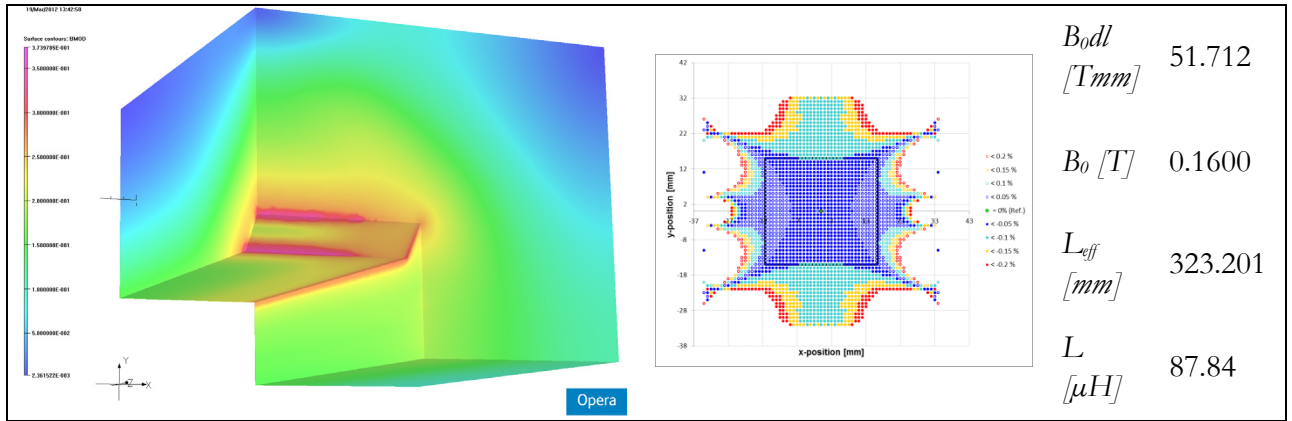|	
$B_0 dl$ [Tmm]	51.712
B_0 [T]	0.1600
L_{eff} [mm]	323.201
L [μH]	87.84

Figure 3.74. Chamfered pole edge, I=700 A, B_{max}=374 mT

The simulations with increased current are needed to prove the feasibility of operating the MKC at increased excitation for future upgrades of the MedAustron machine.

Figure 3.75 shows flux density plots for the two excitation currents of 600 and 700 A. For both simulations planar field maps on surfaces bisecting the yoke have been extracted, and the values above 100 and 200 mT have been removed from the display.

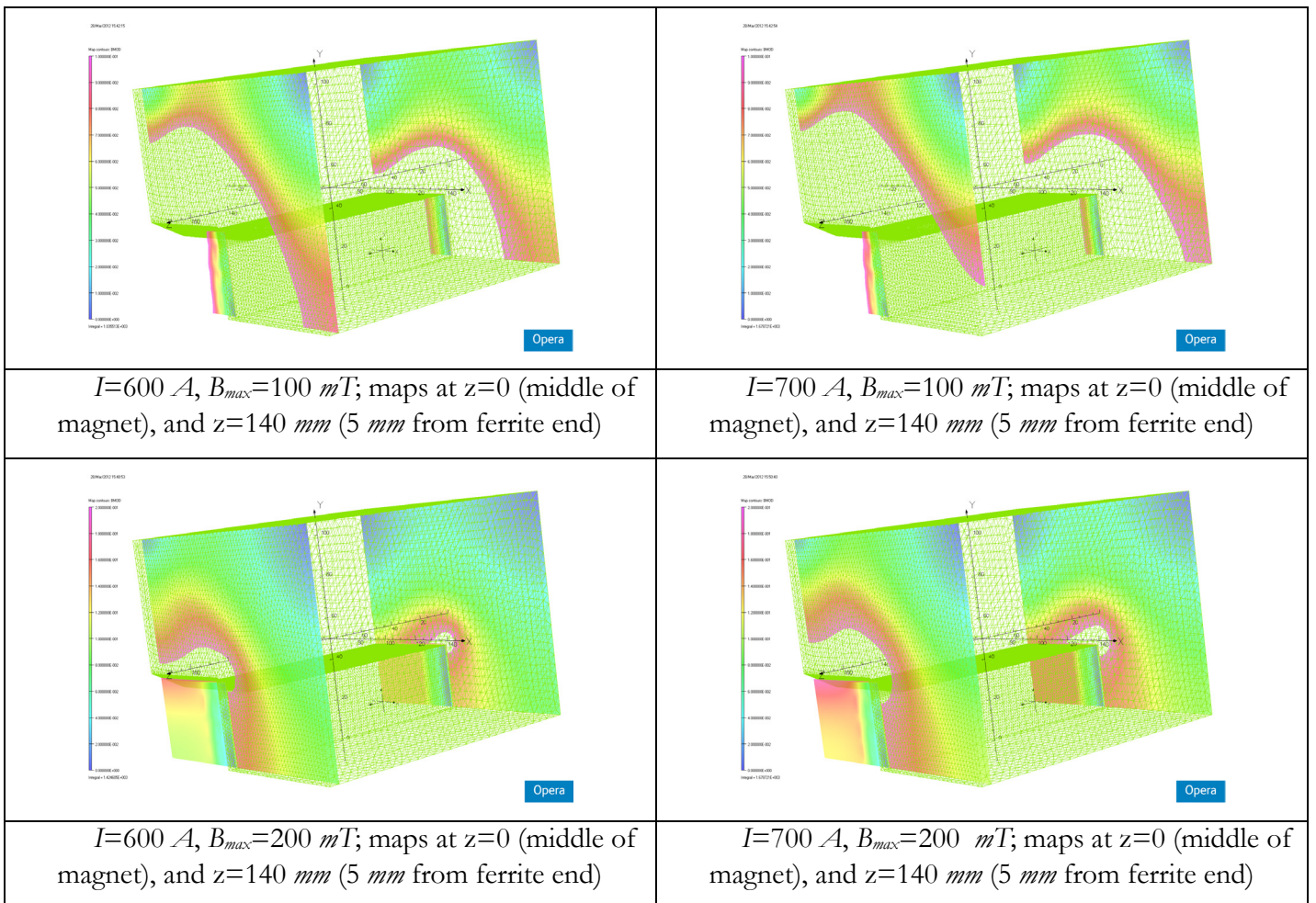|	
I=600 A, B_{max}=100 mT; maps at z=0 (middle of magnet), and z=140 mm (5 mm from ferrite end)	I=700 A, B_{max}=100 mT; maps at z=0 (middle of magnet), and z=140 mm (5 mm from ferrite end)
I=600 A, B_{max}=200 mT; maps at z=0 (middle of magnet), and z=140 mm (5 mm from ferrite end)	I=700 A, B_{max}=200 mT; maps at z=0 (middle of magnet), and z=140 mm (5 mm from ferrite end)

Figure 3.75. Maximum flux densities

The second row shows the saturated regions (transparent) above 200 *mT*. Although the 700 *A* excitation current causes saturation of larger parts of the ferrite yoke, the field homogeneity plot on Figure 3.74 proves that this option is feasible as the field quality and the effective magnetic length are preserved.

3.4.3   Conclusions on shape of ferrite yoke

During the examination for defects it has been discovered that chamfering the edges of the pole face will improve the field quality and reduce the total saturation levels in the yoke. It was agreed that although it will require a more lengthy and costly machining operation, this option should be implemented in the final design.

The drawing of the top/bottom ferrite is shown on Figure 3.76. A picture of a glued block as received from CMI is shown on Figure 3.77. A small chip within the specification is visible on the outside corner.
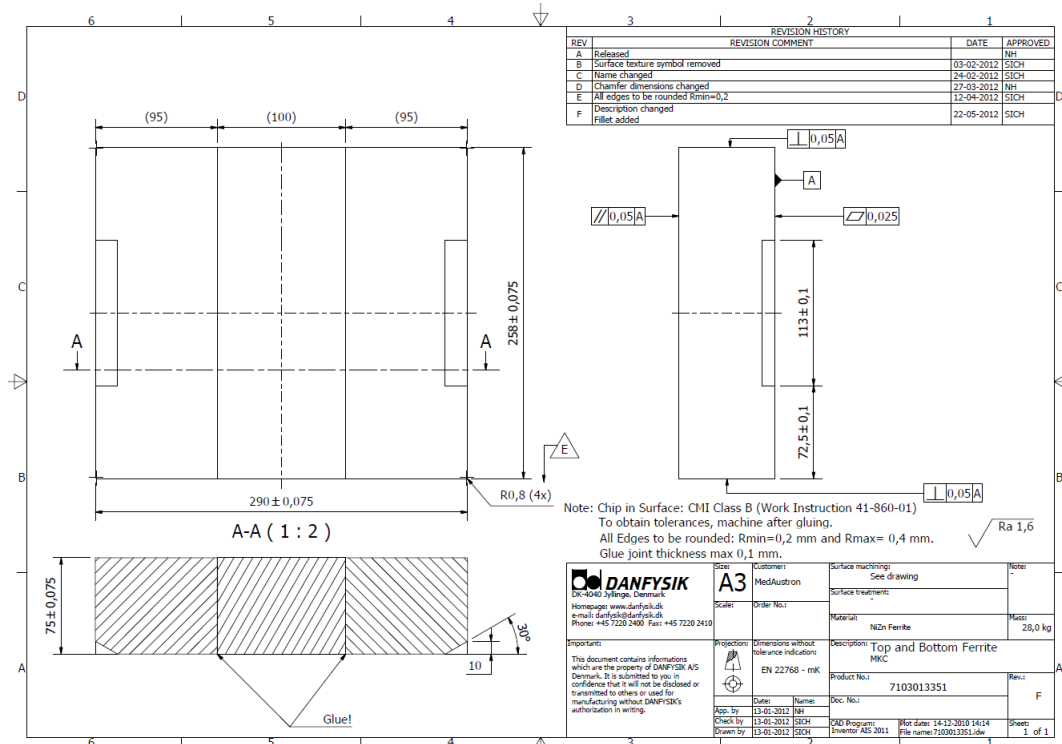

Figure 3.76. Top/bottom ferrite production drawing. Copyright MedAustron©, Danfysik©

Figure 3.77. Top/bottom class B ferrite block

Chapter 4

Magnetic measurements

In this chapter the results of the magnetic measurements and factory acceptance tests will be examined and compared with the simulations.

The magnets were produced and tested in the premises of Danfysik near Copenhagen in Denmark in the autumn of 2013. The testing and measurements have been carried out as prescribed in [26] and [27]. The good field regions of all magnets are mapped, and the values are compared with the Opera simulations.

4.1 Magnetic measurements.

For the DC magnetic measurements (there was no appropriate pulsed power supply available and it was not required in the specification) a field mapping table is used to measure the field values on a rectangular 3d grid [27]. The table has a range of 1300 *mm* in the transverse plane, and a 360 *mm* in the vertical direction. The positioning accuracy is better than 0.1 *mm*.
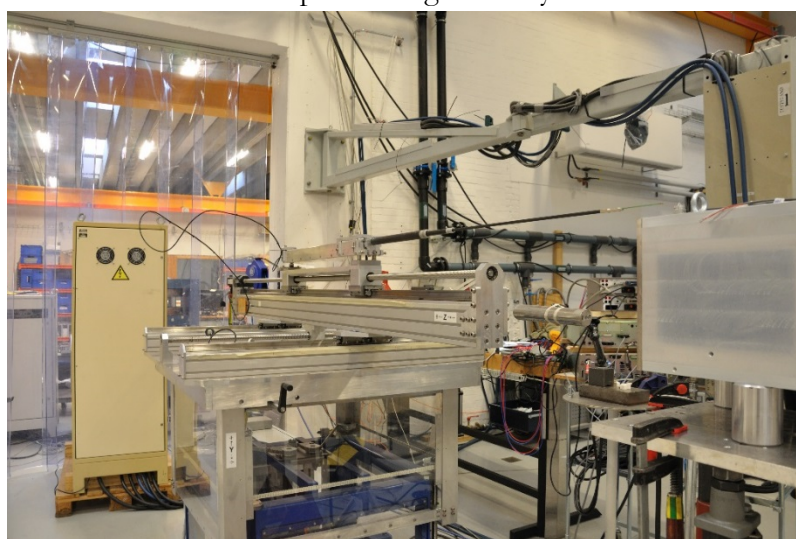

Figure 4.1. Measurement table. MKC magnet is on the right.

Figure 4.1 shows the field mapping table. It is equipped with an analogue Hall probe from Group3 with a short-term drift of $\pm$ 0.005 *mT* for fields up to 0.1 *T*, and $\pm$ 0.02 *mT* for fields above 0.1 *T*. The negative z direction is towards the magnet as shown on the picture.

The magnet is aligned with respect to the table using the reference target on top (Figure 4.2).
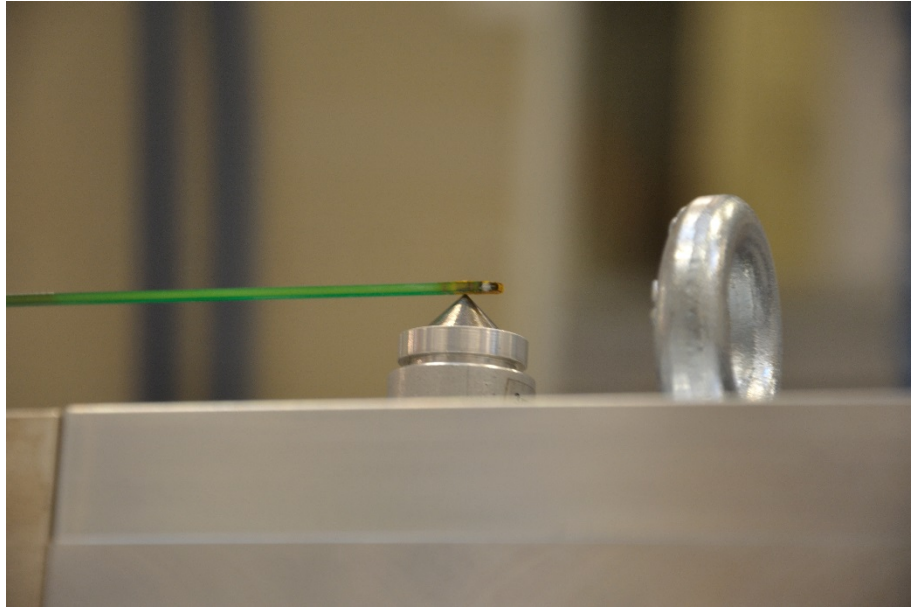

Figure 4.2. Probe being aligned with the reference target

The probe is then placed in the magnet centre (0, 0, 0), and is moved outside of the magnet at a distance $z = -$ 300 *mm* (see 2.1.1 and 2.4). The probe is moved backwards from $-$ 300 *mm* to + 300 *mm*, and is set to take values for the magnetic induction on the fly at every 2 *mm*. Thus the integral sum of 300 values is extracted which gives the B_0dl curve. To cover the entire good field region the probe maps an area of $\pm$ 18 *mm* in increments of 3 *mm* in the x direction, and $\pm$ 15 *mm* in increments of 5 *mm* in the y direction as shown on Figure 4.3.
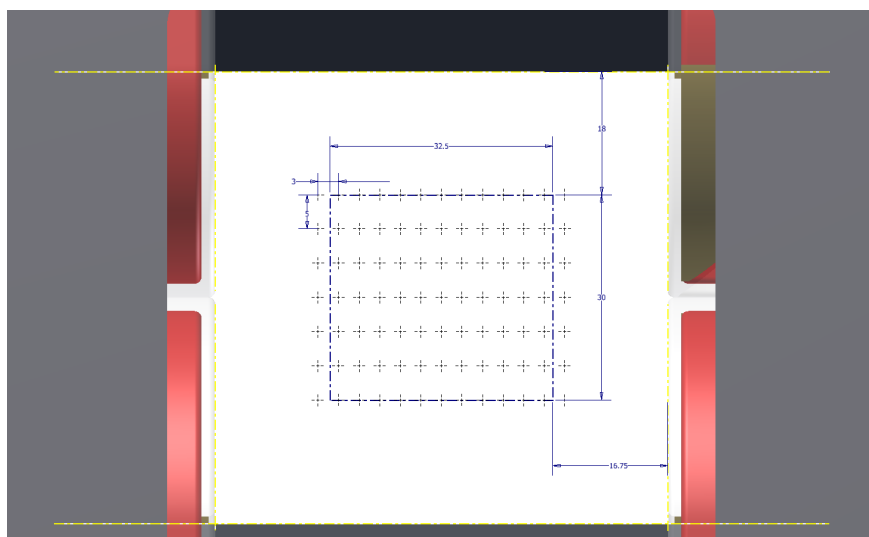

Figure 4.3. Good field region mapping

To remove systematic errors, the *Bdl* curves taken at all points on Figure 4.3 are mapped in the return stroke of the probe. During the tests the magnet is powered with the nominal current 600 A DC.
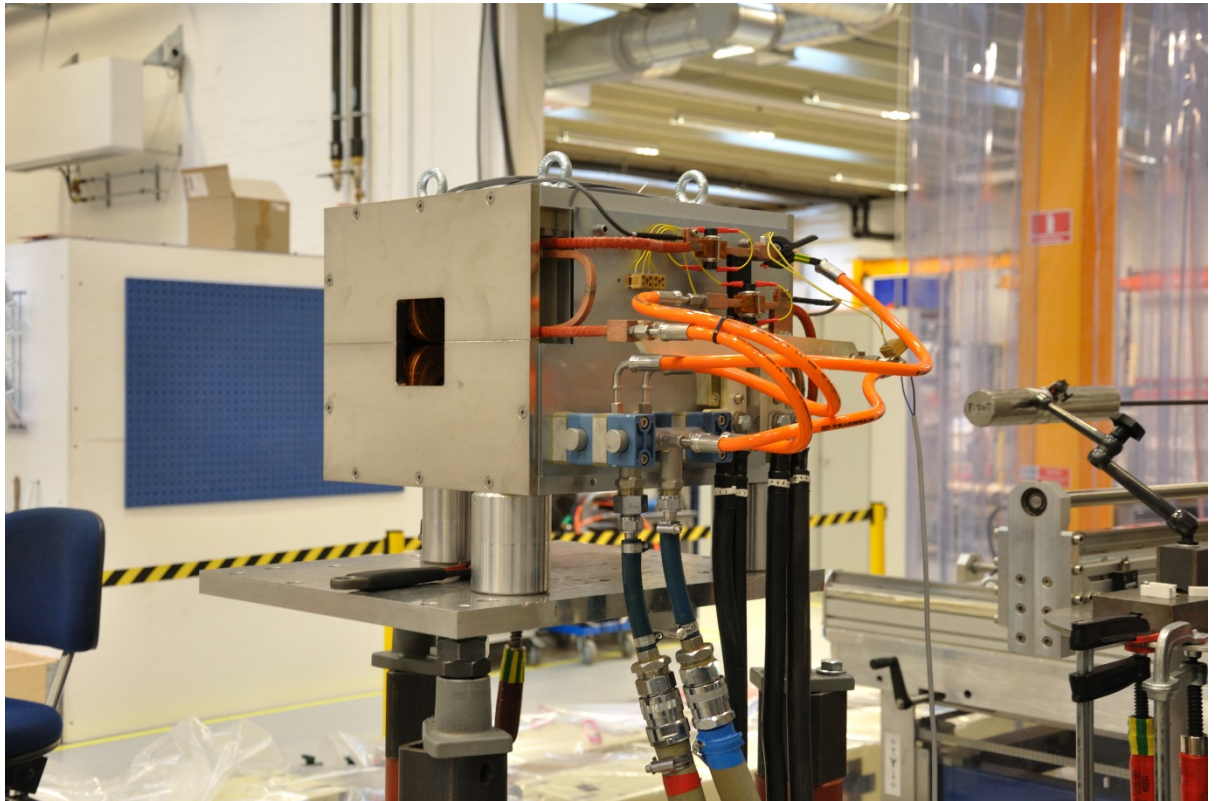

Figure 4.4. MKC magnet on the test bench

4.2   Results of measurements and comparison with the predictions

The results of the magnetic measurements for the five magnets are summarised in Table 4.1. The Opera model has been run with the nominal current of 600 A, rather than the theoretical 597 A.

Table 4.1. Measurements results for each magnet (referred to by their production number)

Magnet №		**12057**	**12058**	**12059**	**12060**	**12061**	**Theoretical**
$\int B_0 dl$ [Tmm]		43.887	43.913	43.904	43.894	43.92	43.864
B_0 [T]		0.13703	0.13707	0.13709	0.13705	0.13715	0.13716
L_{eff} [mm]		320.27	320.37	320.26	320.28	320.24	319.9
ΔBdl_{max} [%]		0.12	0.28	0.28	0.2	0.18	0.13
ΔBdl_{min} [%]		-0.1	-0.2	-0.2	-0.2	-0.2	-0.08
L [µH]	1kHz	81.117	81.555	81.654	81.401	81.337	
	3kHz	77.974	78.377	78.465	78.282	78.215	86.956
	5kHz	76.895	77.308	77.366	77.222	77.169	
R [mΩ]		5.0	5.1	5.1	5.03	4.99	4.4

The graphs for B_0dl are plotted for all five magnets and compared to the Opera model. Figure 4.5 shows the overlapping plots.

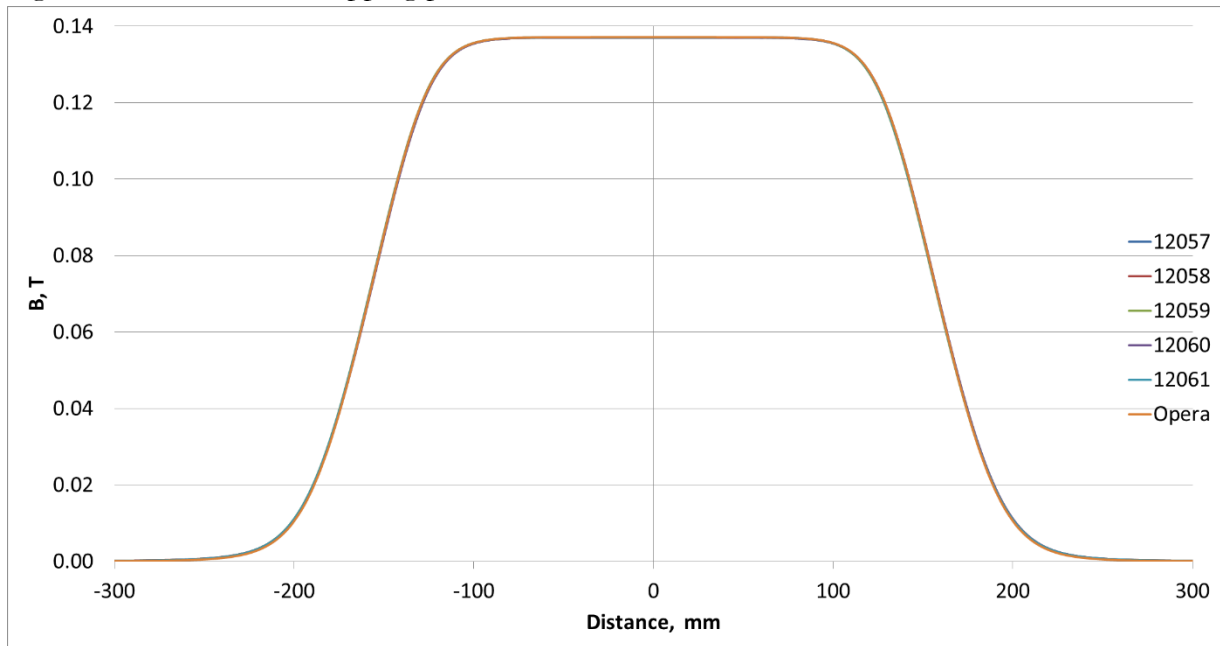Figure 4.5. Integrated field values for the 5 magnets as compared to the Opera model

A zoom in on the central area of the graph is presented on Figure 4.6. It shows that the values for B_0 coincide to about 0.09 % as shown in Table 4.1.
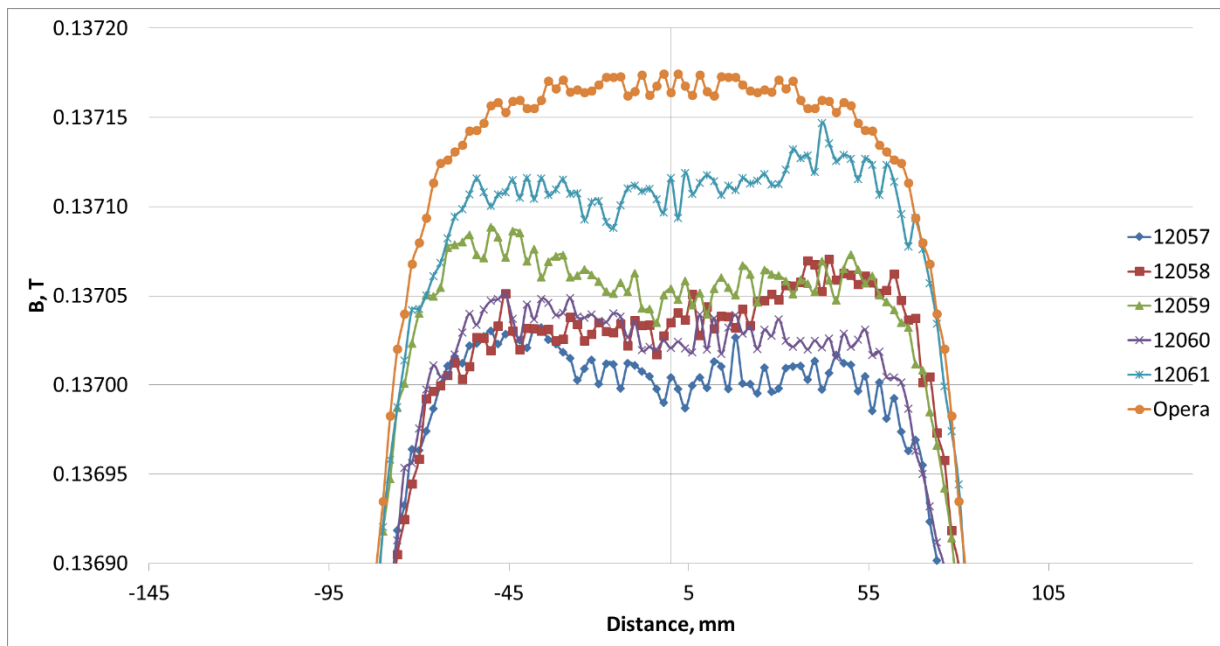

Figure 4.6. Integrated filed values zoom in

Figure 4.7 shows the field values under the length of the poles of the magnet whereas Figure 4.8 shows the fringe fields.
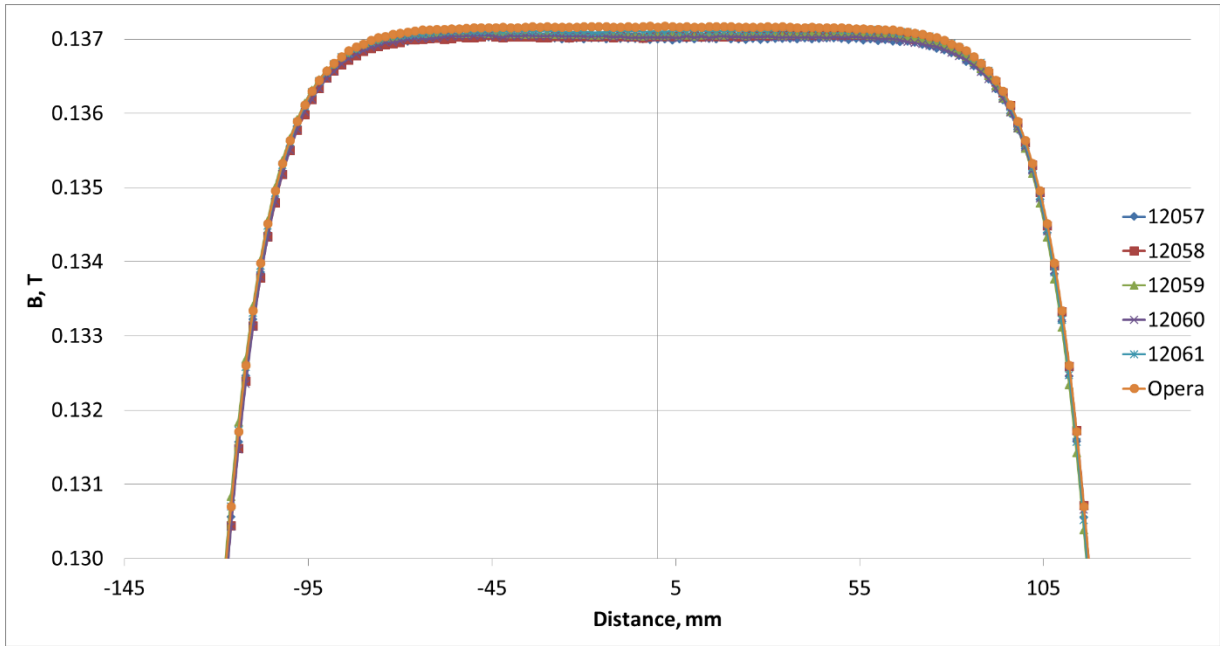
75

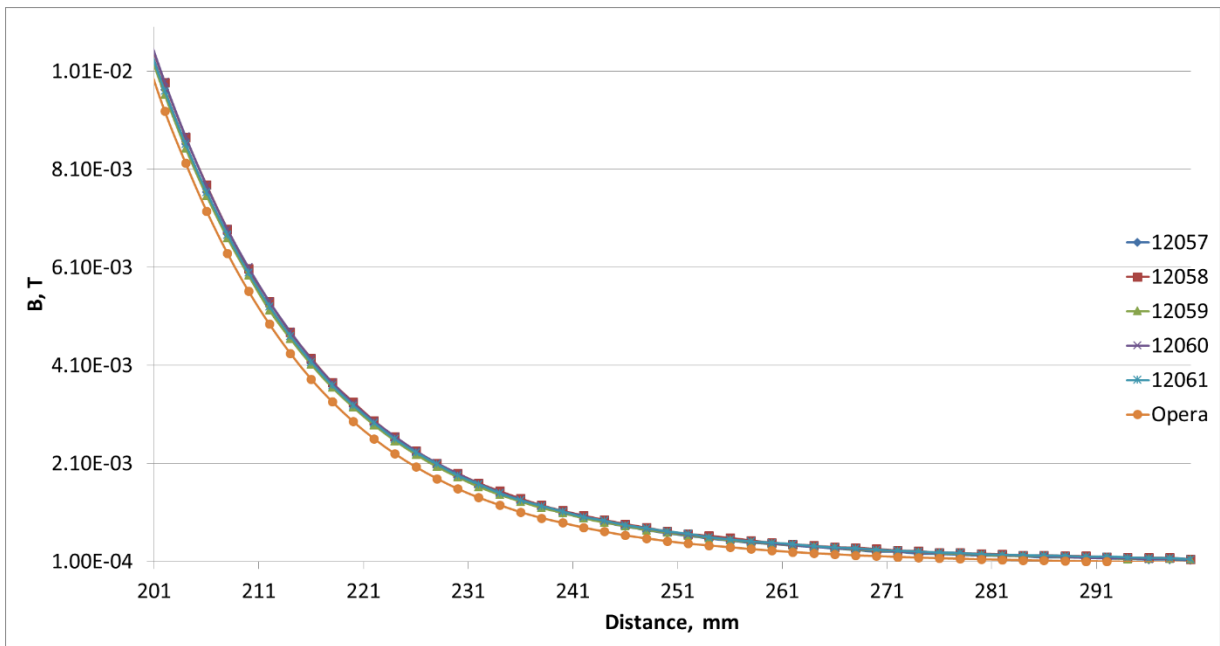Figure 4.7 Field values under the poles

Figure 4.8 End fields

A comparison of the homogeneity plots is shown on Figure 4.9.
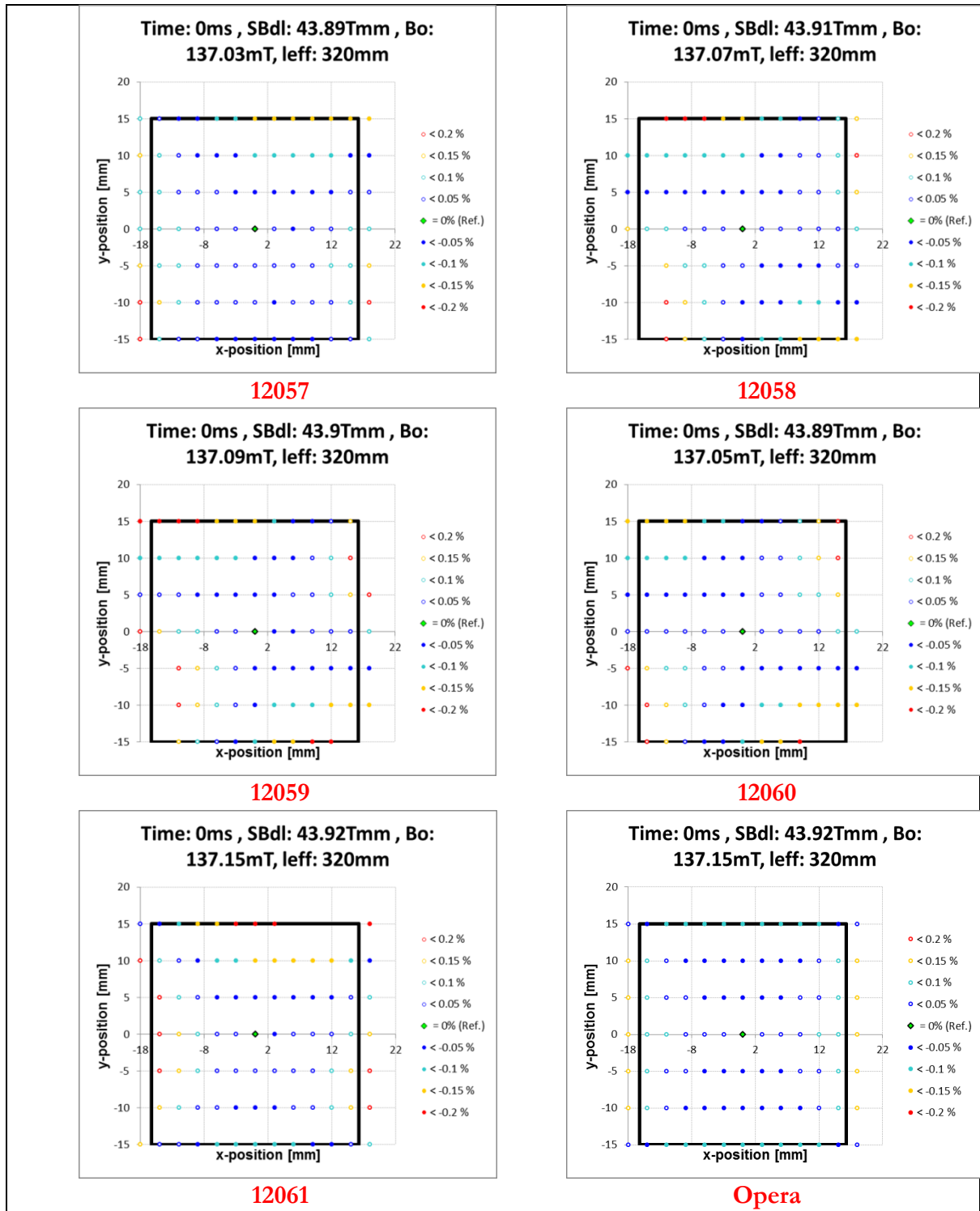
Figure 4.9. Homogeneity plots

4.2.1 Excitation linearity

For this measurement the probe is placed in the magnet centre and the power supply is ramped from zero to nominal current and back to zero in increments of 50 A (Figure 4.9). The corresponding graph for magnet 12059 is shown in Figure 4.10.
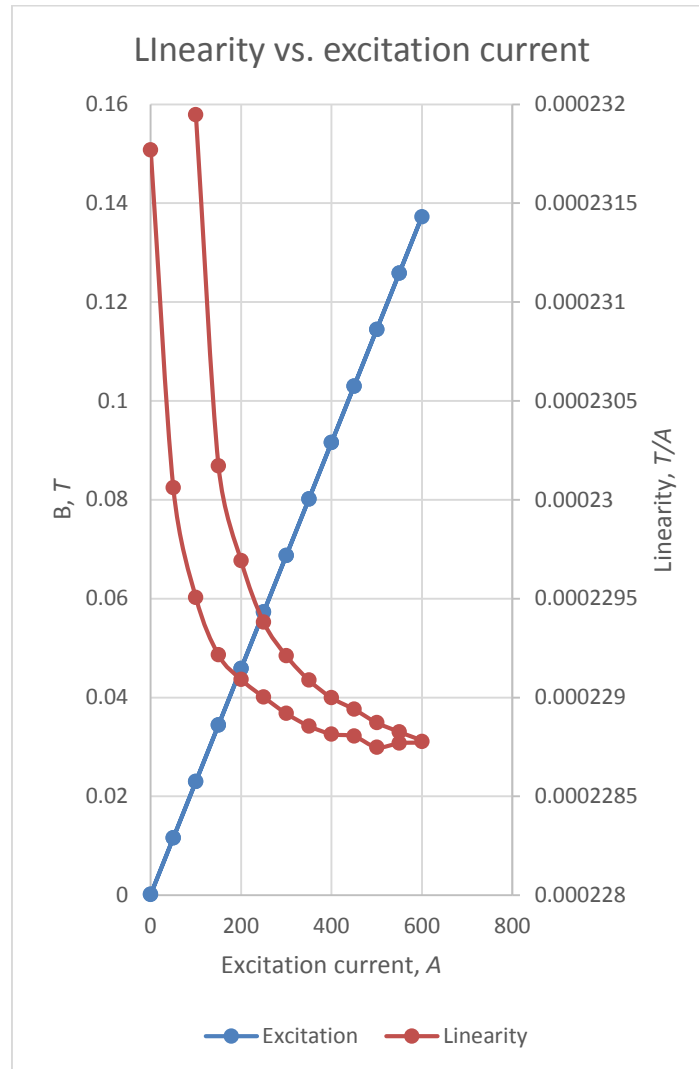
Figure 4.10. Excitation linearity for magnet 12059

It can be seen from the graph that the excitation current drives a linear increase of magnetic field. The linearity as shown in the graph is the ratio between the magnetic field and the current. It shows a good reproducibility in the full operational range of 100-600 A. The maximum error of 0.05 % is found at lowest excitation current region. The linearity increases with the increase of current.
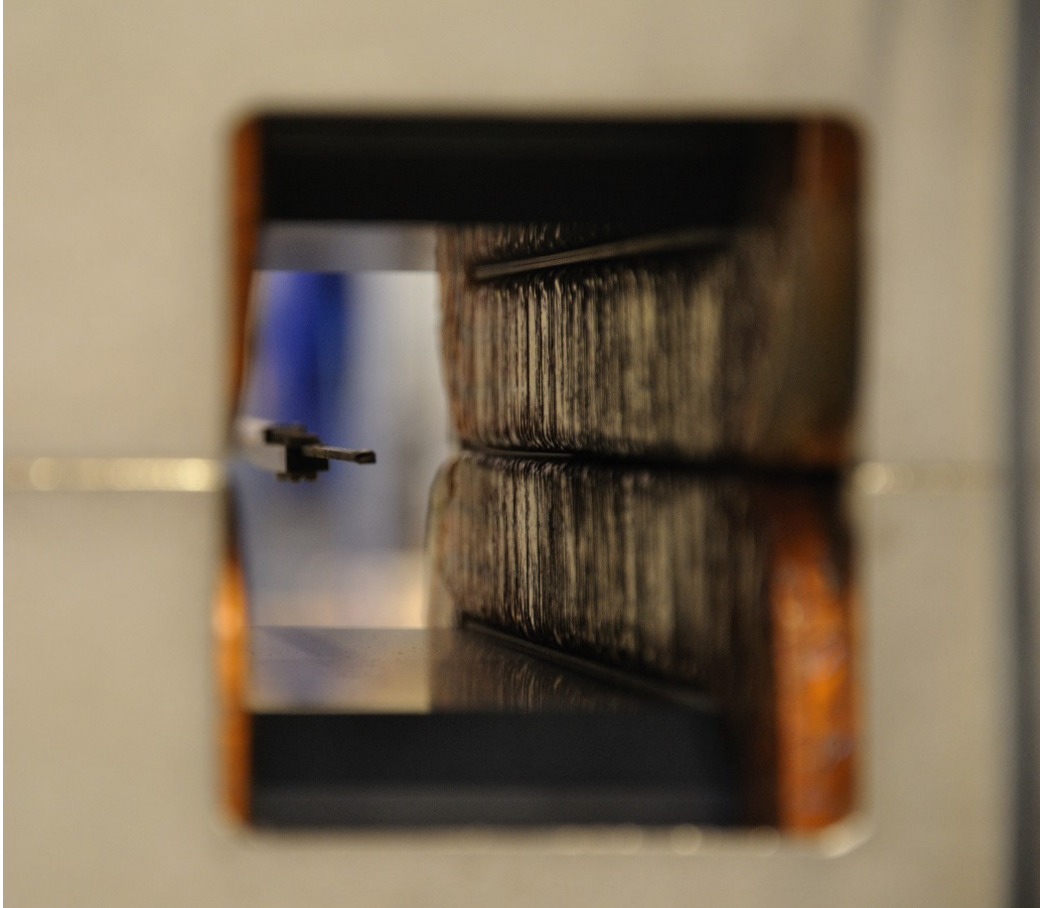
Figure 4.11. Probe in the magnet centre for B_0 measurement

4.2.2 Summary of the measurements

The magnetic performance of all five magnets was considered satisfactory, and the magnets were accepted by MedAustron. The field homogeneity, integrated length, linearity, and the electrical and mechanical parameters conform to the technical specification and

The magnets were delivered in Wiener Neustadt in the spring of 2014, and were subsequently installed in the accelerator in June 2014.

Figure 4.12 shows the magnets installed in the machine.

Figure 4.12. MKC magnets installed in the accelerator

Chapter 5

Conclusions

5.1 Optimisations

The simulations of the coil insulation design have shown that there was room for improvement for future designs where an increased voltage hold off could be required (for example in case a burst mode operation were to be implemented). The insulation levels can be doubled between the vertical layers of the coil which are subject to half the nominal applied voltage. The modified coil would retain the field homogeneity and would not require a change in the magnet's overall dimensions.
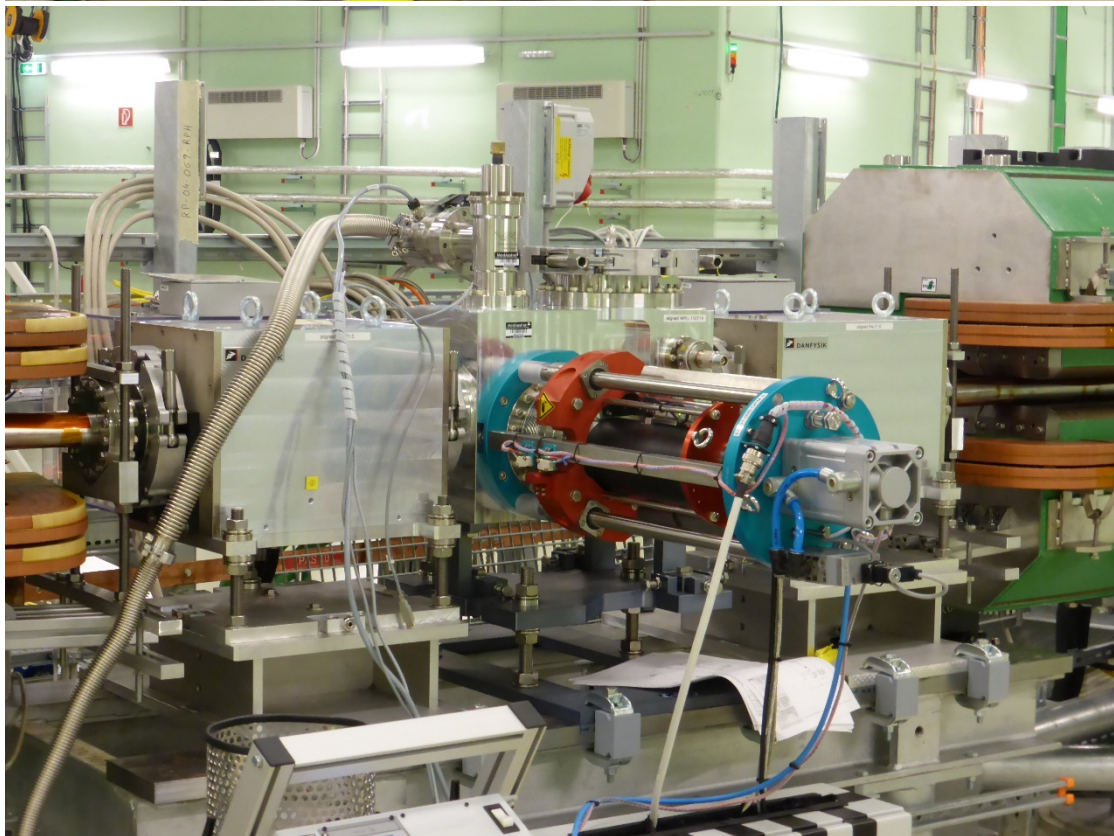
The study of the brazing of the flanges to the vacuum chamber showed that the magnetic material used for the collar acts like a shield for the fringe fields that are present in this region. The reduction of the fringe fields which are a part of the total integrated field leads to a reduction in effective length, thus care must be taken when choosing the length of the vacuum chamber. This should be as far away from the endplates as the integration allows, as to not have an effect on the integrated field. An offset of 20-30 *mm* is shown to be sufficient (23 *mm* was chosen for the definitive design). The required field homogeneity has been retained for all configurations examined.

The optimisation of the coil heads has shown that the geometry of the current carrying conductors plays a crucial part in establishing highly homogenous fields even in normal conducting magnets like the MKC. The results of the study confirm that a compromise between mechanical and electromagnetic considerations can be made, and a coil could be produced that satisfies both design aspects. The modifications of the coil heads have been incorporated into the final design. The coil configuration has also served as a base for the new BSW magnets currently under development at CERN for the 2 *GeV* H⁻ injection into the Proton Synchrotron Booster.

The shape of the ferrite pole edges has been redesigned, since the initial geometry showed unacceptable saturation levels in these volumes, hence reduced field homogeneity. Additionally it is also a more robust and reliable solution from the mechanical point of view, as the pole ends are prone to chipping during the insertion of the coil. Although the new ferrite shape requires lengthier and hence costlier machining operations, these considerations were deemed sufficiently important to justify the additional expenditure.

5.2 Magnetic measurements

The optimisations imposed several changes to the preliminary design, which were confirmed by the final measured results.

All magnets have passed the acceptance tests, which also proved the validity of the Opera models. All the values measured were in agreement with the finite element calculations.

The most important aspect of the performance of the magnets is the good field region homogeneity. The particle beam is on its way towards the patient downstream of the chopper bump and its shape should not be changed as it exits the last magnet. Therefore the homogeneity of the bending field will guarantee that the beam will be delivered at the correct spot on the tumour.

The downstream trajectory is unaffected since all the magnets have the same characteristics, and are connected in series, thus receiving the same excitation currents, hence providing the same deflections. For this reason the stability and overshoot of the power supply are less critical issues.

The measurements were done in DC, since the power converter for the magnets was still being built at the time of writing.

The linearity of the excitation current with respect to the field obtained guarantees correct deflection angles within the entire dynamic range of particle energies.

5.3 Applications

In terms of applicability this work can be used as a guideline for magnet designers in the aspects of evaluating coil configurations and shaping the magnetic circuits.

The instructions for building the model in Opera 3d can be used to introduce new users to the program and help understand the finer aspects of modelling with finite elements.

The newly adopted technique of meshing the good field region with regular hexahedra can prove useful in extracting nodal values of the fields and incorporating them into matrices for the study and evaluation of magnetic field components with high accuracy.

Bibliography

[1]   U. Amaldi, "Particle accelerators take up the fight against cancer," *CERN Courier,* Dec 6, 2006.

[2]   S. Braccini, "Progress in hadrontherapy," in *Nuclear Physics B Proceedings Supplements*, Geneva, 2007.

[3]   U. Linz, Ion Beam Therapy, Jülich: Springer, 2011.

[4]   P. J. Bryant et al., "Proton-Ion Medical Machine Study (PIMMS)," CERN - PS Division, Geneva, 1999.

[5]   CNAO press release, "Tumor "bombarded" with carbon ions for the first time in Italy," Centro Nazionale Adroterapia Oncologica, Pavia, 2012.

[6]   H. Wiedemann, Particle Accelerator Physics, Springer, 2007.

[7]   E. Wilson, An Introduction to Particle Accelerators, Geneva: Oxford University Press, 2001.

[8]   M. Reiser, Theory and Design of Charged Particle Beams, Wiley-VCH, 2008.

[9]   L. Badano, M. Benedikt, P.Bryant, M. Crescenti, P. Holy, P. Knaus, A. Maier, M. Pullia, S. Rossi, "Synchrotrons for Hadron Therapy," CERN - PS Division, Geneva, 1999.

[10]   M. Benedikt, A. Fabich, "MedAustron - Austrian Hadron Therapy Centre," in *IEEE Nuclear Science Symposium Conference Record*, 2008.

[11]   J. Borburgh et al, "Design and Development of Kickers and Septa for MedAustron," in *IPAC*, 2010.

[12]   M. Barnes et al., "Engineering Specification for the MedAustron Injection Bumper, Dump Bumper, Tune Kicker and Chopper Dipole Magnets," ES-100701-a-MBA, Geneva, 2011.

[13]   Opera-3d User Guide, Version 16R1, Cobham Technical Services, 2013.

[14]   Opera Additional Support Knowledgebase, Version 16R1, Cobham Technical Services, 2013.

[15]   Opera-3d Reference Manual, Version 16R1, Cobham Technical Services, 2013.

[16]   C. W. Trowbridge, An Introduction to Computer Aided Electromagnetic Analysis, Vector Fields Ltd., 1990.

[17]   В. Спасов, Числени методи и моделиране на полета, Записки, Пловдив: Издателско полиграфично звено на ТУ София, филиал Пловдив, 2003.

[18]   M. Atanasov, M. Barnes, "MKC Insulation: Field Evaluation for Different Coil Insulation Configurations," EN-111118-b-MAT, Geneva, 2011.

[19]   M. Atanasov, "MKC Vacuum Chamber: Effects of Metal Joint Brazing on Field Quality," EN-111118-a-MAT, Geneva, 2011.

[20]   J. Borburgh, Private communication.

[21]   M.J. Barnes, T.Fowler, M. Atanasov, T. Kramer, T. Stadlbauer, "Effect of a Metallized Chamber Upon the Field Response of a Kicker Magnet: Simulation Results and Analytical Calculations," in *IPAC'12*, New Orleans, 2012, THPPD074.

[22]   M. Atanasov, "MKC Coil: Field Evaluation for Proposed Changes of Coil Dimensions," EN-120131-a-MAT, Geneva, 2012.

[23]   H. E. Knoepfel, Magnetic Fields: A Comprehensive Theoretical Treatise for Practical Use, New York: Wiley-Interscience, 2000.

[24]   T. Sørensen et al., "Preliminary Design Report Chopper Magnet, MKC," AUS501383-PDR-005, 2012.

[25]   M. Atanasov, "MKC Ferrite: Field Evaluation for Expected Chips in Ferrite," EN-120305-a-MAT, Geneva, 2012.

[26]   M. Barnes et al., "Specification for Dump Bumper, Injection Bumper, Chopper Dipole and Tune Kicker Magnet Measurements," ES-100701-f-MBA, Geneva, 2011.

[27]   N. Hauge et al., "Magnet Measurement Report: Detailed Design," AUS501383-DDR-006 Measurements, 2012.

[28]   J. Tanabe, Iron Dominated Electromagnets. Design, Fabrication, Assembly and Measurements, Stanford, 2005.

[29]   T. Sørensen et al., "Detailed Design Report and Cover Letter for DDR," AUS501383-DDR-003 rev 1 - MKC, 2012.

[30]   S. Russenschuk, Field Computation for Accelerator Magnets, Wiley-VCH, 2010.